2017

Fuzzy Logic Based Energy Storage Management System for MVDC Power System of All Electric Ship

Mohammed Masum Siraj Khan

FLORIDA STATE UNIVERSITY

COLLEGE OF ENGINEERING

FUZZY LOGIC BASED ENERGY STORAGE MANAGEMENT SYSTEM FOR MVDC POWER SYSTEM OF ALL ELECTRIC SHIP

By

MOHAMMED MASUM SIRAJ KHAN

A Thesis submitted to the
Department of Electrical and Computer Engineering
in partial fulfillment of the
requirements for the degree of
Master of Science

2017

Mohammed Masum Siraj Khan defended this thesis on April 6, 2017.
The members of the supervisory committee were:

Md Omar Faruque
Professor Directing Thesis

Simon Y. Foo
Committee Member

Pedro Moss
Committee Member

The Graduate School has verified and approved the above-named committee members, and certifies that the thesis has been approved in accordance with university requirements.

To my parents- Mr. Mohammed Iqbal Khan and Mrs. Lutfur Nessa Khanam

ACKNOWLEDGMENTS

I am really grateful to many people, especially my supervisor Dr. Md Omar Faruque for his guidance and support. Also, I want to thank Dr. Yi Guo, Ali Hariri and Alvi Newaz for their kind supports. I am also grateful to my committee members and the employees of CAPS who helped me a lot. I want to express my gratitude to electric ship research and development consortium (ESRDC) for financing my research.

TABLE OF CONTENTS

Appendices

LIST OF TABLES

LIST OF FIGURES

LIST OF ABBREVIATIONS

AES- All Electric Ship
ATG- Auxiliary Turbine Generator
AVM- Average Value Model
CHIL- Controller Hardware-In-The-Loop
DAB- Dual Active Bridge
DC- Direct Current
DICC- Decoupled Inner Current Control
DOD- Depth of Discharge
EMALS- Electromagnetic Aircraft Launch System
EMRG- Electromagnetic Rail Gun
ESM- Energy Storage Management
FC- Flying Capacitor
FES- Flywheel Energy Storage
FESS- Flywheel Energy Storage System
FL- Fuzzy Logic
FPGA- Field-Programmable Gate Array
HESM- Hybrid Energy Storage Module
HESS- Hybrid Energy Storage System
HFAC- High Frequency Alternating Current
I/O- Input/Output
IPS- Integrated Power System
LIB- Lithium-Ion Battery
LPF- Low Pass Filter
MMC- Modular Multilevel Converter
MTG- Main Turbine Generator
MVAC- Medium Voltage Alternating Current
MVDC- Medium Voltage Direct Current
NGIPS- Next Generation Integrated Power System
NPC- Neutral Point Clamped
ONR- Office of Naval Research
PCM- Power Conversion Module
PCS- Power Conditioning System
PI- Proportional-Integral
PV-Photovoltaics
QOS- Quality Of Service
SFP- Small Form-Factor Pluggable
SMES- Superconducting Magnetic Energy Storage
SOC- State of Charge
SOD- State of Discharge
VHDL- VHSIC Hardware Description Language
XSG- Xilinx System Generator

ABSTRACT

The power management strategy in a medium voltage direct current (MVDC) based power system of an all electric ship (AES) with Hybrid Energy Storage System (HESS) can greatly affect the energy efficiency of the system. In order to maintain the bus voltage of a MVDC shipboard power system within the allowable margin with the operation of different types of loads, the energy storage has become indispensable part of the AES. With the aim of supporting the MVDC shipboard power system, an energy storage management (ESM) system based on Fuzzy Logic (FL) has been proposed and its performance with a Proportional-Integral (PI) control algorithms is compared. In order to support the peak demand and pulsed load, a HESS incorporating high energy density storage (battery), and high power density storage (supercapacitor) are proposed. Based on the analysis of power flow, the load characteristics, the power management objectives, constraints and the ease of implementation in MVDC power system, the battery and supercapacitor are considered as the potential storage devices. For energy transfer among the energy storages and the MVDC system, bi-directional DC-DC converters with dual active bridge (DAB) configuration are used. With the changes of the bus voltage and load power demand, the ESM systems provide instantaneous reference powers for charging or discharging of the battery and supercapacitor. The reference powers for the battery and supercapacitor are sent to the respective controllers of the DAB converters. Two power sharing strategies are designed to share power among multiple energy storages. The MVDC shipboard power system with the generators, loads, battery and supercapacitor with DAB converters are modeled in SimPowerSystems. Simulation results are used to make a comparison of performances of the FL and PI controller based ESM systems. Finally, controller hardware-in-the-loop (CHIL) based experimental results are added to demonstrate the effectiveness of the controller.

CHAPTER 1

INTRODUCTION

1.1 Electric Ship Technology

1.1.1 Background

In 1878, the USS Trenton was built containing two propulsion systems. The ship had another new feature, an electric lighting system, which was the first U.S. Navy ship service power system. The size of the electric power system of the ship is dependent on the electric load demand [1]. For instance, in sailing ships, the propulsion system provides power only for propulsion and not for the ship's service loads. Prior to and during World War II, in turboelectric ships, propulsion and ship service electric power were provided by separate prime movers. The first U.S. naval ship powered by electric motors in 1912 had two electrical systems: one for propulsion and the other for service loads [2]. When the ship service load and propulsion load are provided power from the common generators, the power system is called an Integrated Power System (IPS), otherwise it is called a segregated power system. The segregated systems utilize separate generators for the ship service load and propulsion load. Figure 1.1 shows the comparison between a segregated power system and an integrated power system. From Figure 1.1, four geared turbines are used for propulsion system but three less powerful turbines are assigned for ship service loads [3]. The problem with the segregated power system is that most of the produced power (around 80-100MW) is available only for propulsion system. If higher power is required for the loads (example: pulsed load and radar load) except for propulsion load, it cannot be extracted from the propulsion turbines even if the propulsion system is not operating [4]. To solve the problem with segregated power system, an IPS has been developed. Figure 1.1 shows that the IPS system uses fewer prime movers than the segregated power system and supply power to both propulsion load and service load. The IPS structure has been used on the DDG-1000 Zumwalt-class destroyer, the T-AKE-1 Lewis-and-Clark-class cargo ship, the currently suspended CG(X) next generation cruiser, the LHA-6 Makin-Island-class amphibious assault ship, the Flight III Virginia-class attack submarine, and the CVN-21 Gerald-Ford-class aircraft carrier [3,4]. The U.S. Navy invested significantly in developing

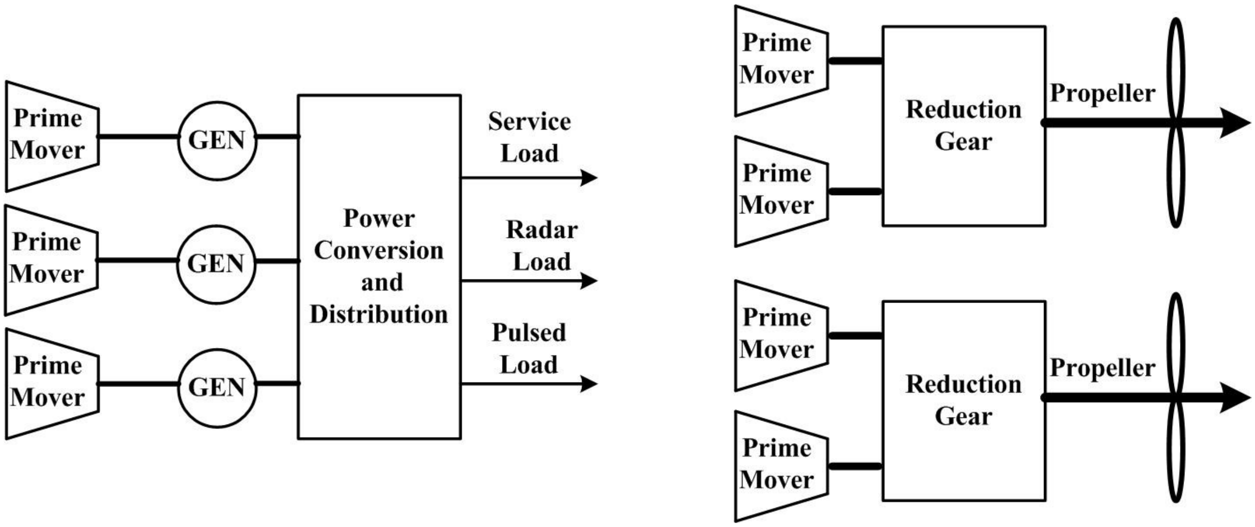

(a) A segregated power system.

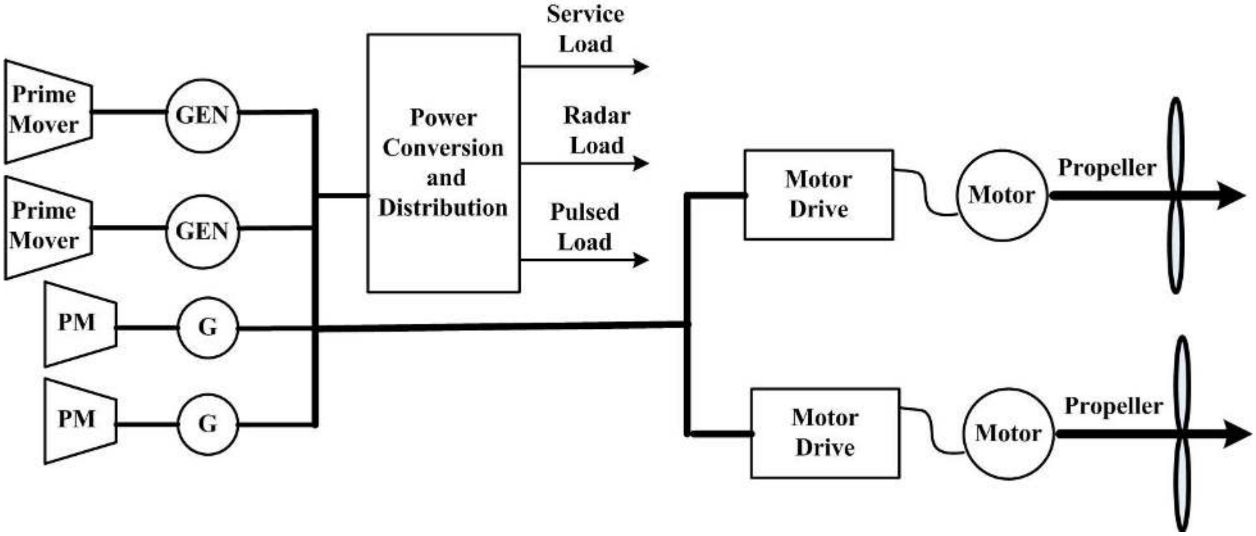

(b) An integrated power system.

Figure 1.1: Comparison between a segregated power system and an integrated power system.

IPS structure between 1992 and 2007 [3]. A radical change of mechanical propulsion to electric propulsion produces a significant increase of electric power demand for the shipboard power system. The electric power demand is increased even more with the incorporation of railguns and lasers along with the regular ship service loads. Those pulsed loads demand high amplitude electric power

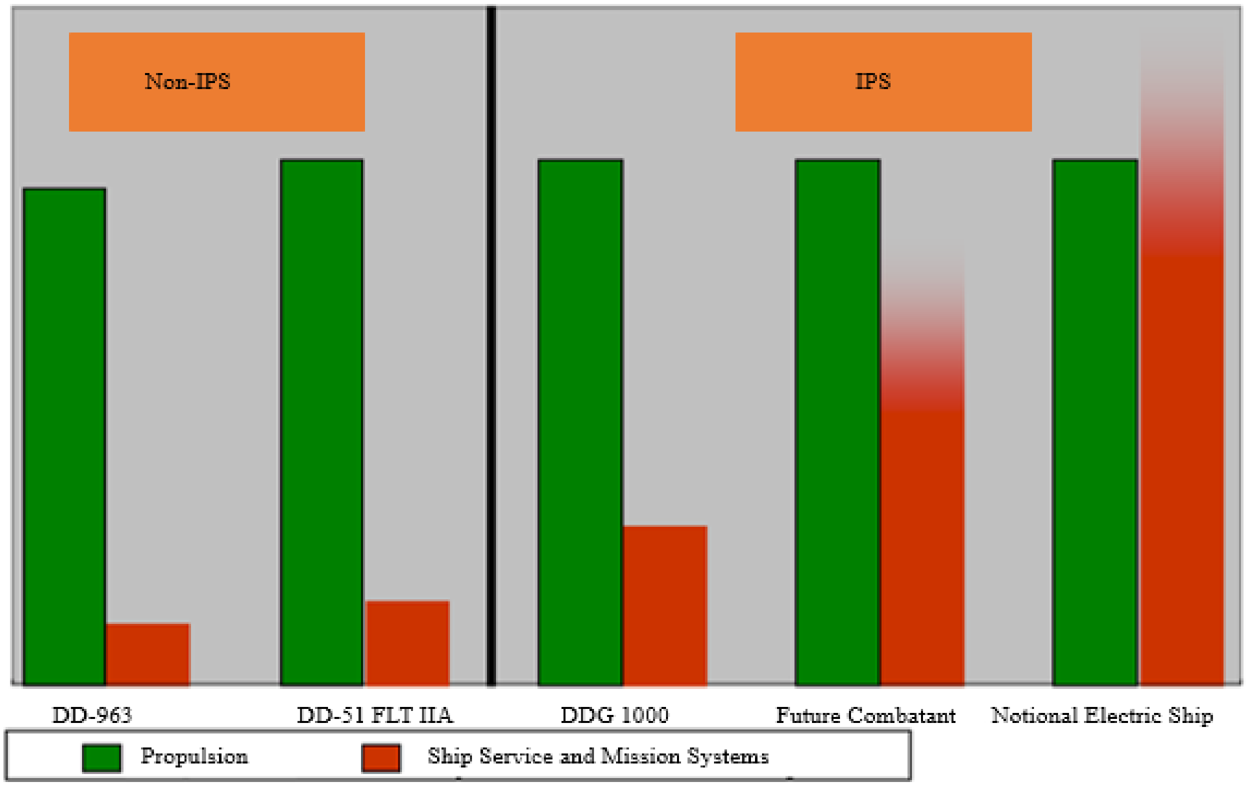

Figure 1.2: Comparison of Non-IPS and IPS power demand.

(tens of MW range) within a very short time [5]. Figure 1.2 shows the projected propulsion load and ship service load for IPS and segregated structured based ship. It shows that ship service load is increasing because of incorporation pulsed load such as railguns and lasers.

The modern ship design is migrating towards the IPS architecture with electric propulsion, advanced radar, and weapons system. In this IPS structure based power system, both the propulsion or ship service load receives power from the common source. The Office of Naval Research (ONR) has initiated a new program called Next Generation Integrated Power System (NGIPS) to provide direction for future IPS based electric ship development [3]. The NGIPS technology development roadmap [3] is shown in Figure 1.3 which has three phases. The first phase is medium voltage alternating current (MVAC) based configuration with voltage between 4kV to 13.8kV at 60Hz frequency. This phase is already implemented in the DDG-1000 and the T-AKE-1 [4]. In order to reduce the size and weight of the components the second phase will be based on high frequency AC (HFAC) that uses same voltage range like MVAC (4kV to 13.8kV AC), but that can operate higher than 60Hz and lower than 400 Hz [3]. The final phase is based on MVDC with voltage range between 5kV to 20kV.

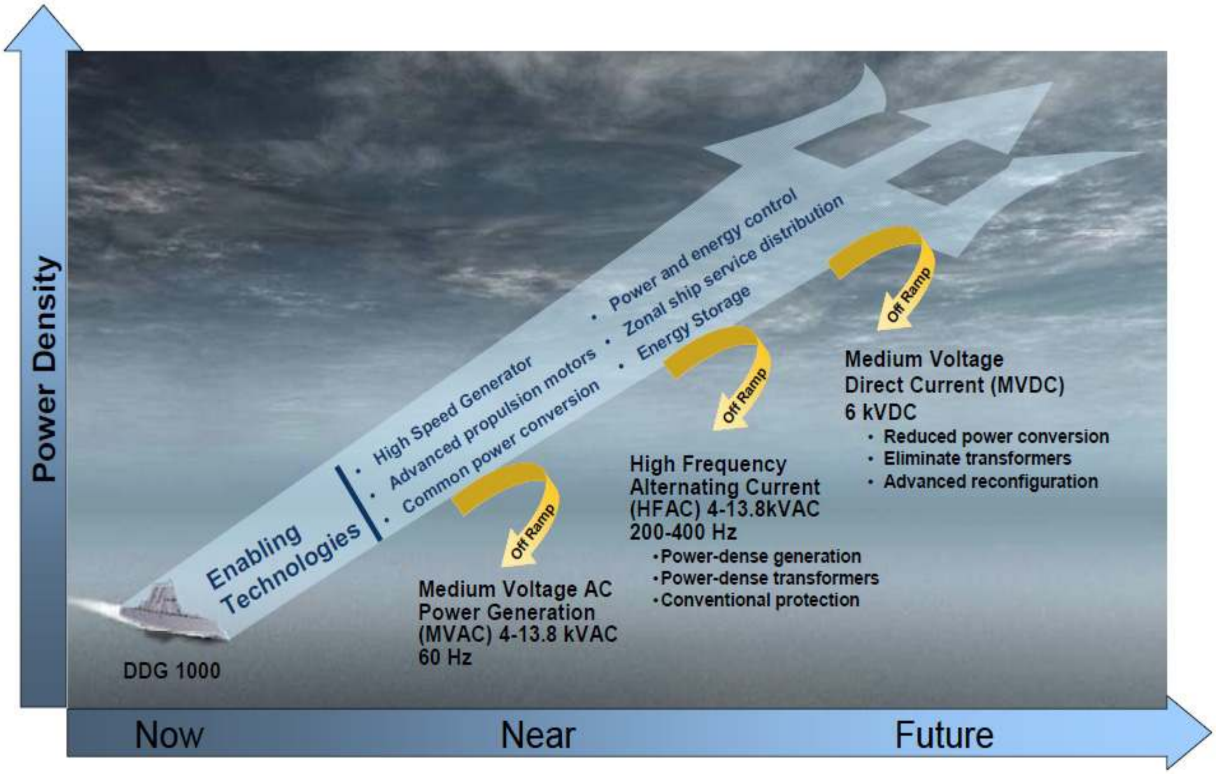

Figure 1.3: Projected development path for the IPS based structure for the shipboard power system [3].

1.1.2 Energy Storage Management System

Because of transformation of the mechanical propulsion system into an electrical propulsion system, the electric power demand of AES increases significantly. Traditional ships deal with only a few MWs of electrical power, but an AES with electrical propulsion system needs to deal with nearly 100MW of electrical power generation and distribution [5]. Pulsed load or electromagnetic aircraft launch system (EMALS), and electromagnetic rail gun (EMRG) are two major loads which demand impulse power of very high amplitude. Incorporation of intermittent weaponry loads (EMALS, and EMRG) lead to the degradation of power quality. Traditional generators are not capable of fulfilling the desired power demand of the pulsed load as they have limited ability to follow sudden changes of the load. Since the generators have long time constants for control of fuel valves and combustors, they cannot meet transient power demand. Considering the issues of high electric power demand for various loads including propulsion load and pulsed load, the energy storage system has become a vital part of the electric shipboard. The main objectives of using energy storages are: (i) to maintain proper balance between sources and load power demand, (ii) to keep the MVDC bus voltage with in the acceptable range, (iii) to supply power to the pulsed load, (iv) to remove the negative effects of voltage degradation and (v) to store surplus energy. Now the main issue is to design an intelligent ESM system to control the operation of the energy storages (charging and discharging operations).

In [6], the potential uses of energy storages in AES are discussed elaborately. Except meeting transient and peak power demand, energy storages can also be used to store extra energy and to increase system efficiency. In conventional ship, prime movers are connected with the propulsion system but in AES, prime movers are connected to the generators and production of electrical energy can exceeds the demand. In that case, energy storages can store the extra electrical energy and give it back to the system when it is required. Eventually it will increase system's efficiency. In [6], the potential applications of the battery, flywheel, superconducting magnetic energy storage (SMES), and supercapacitor are discussed regarding the requirements of the AES.

Shipboard power system faces adverse situation with load fluctuations due to sudden operation of large loads and the use of HESS is an effective solution to reduce the negative effects of these operations on AES's power system. The use of energy storages for the shipboard power system is discussed in [7–11]. In order to calculate the interactions among the multiple energy sources with the incorporation of HESS, a model based analysis is performed in [8]. For coordinated control, a system-level energy management strategy is used in [8]. In [7], a model predictive control strategy is used to coordinate the controls of the primary energy sources and propulsion motors with the addition of HESS to get better performance. In order to reduce the power fluctuations of the shipboard power system, the potential use of the battery energy storage is discussed in [11]. While dealing with large amount of power fluctuations, battery can be overheated. To save the battery from risk of overheating, a model predictive control based strategy is used to smooth battery power in [11]. In order to solve the problem of energy management of hybrid ships with the presence of disturbances and uncertainties, a nonlinear robust turbo-based model predictive control strategy is proposed in [10]. In this control strategy, a multi-level predictive control strategy is used to control the ship speed and to estimate demanded reference power. A conventional model predictive control strategy is used to track the demanded reference power and to split the demanded power among multiple energy sources. To reduce the amount of fuel consumption in marine hybrid power plant, energy storages are used as the potential devices in [9]. In this thesis, a battery and a supercapacitor are used as the energy storages to supply the transient power demand.

The operation of pulsed load is very uncommon for a conventional power system. Conventional generators are not capable of satisfying pulsed power demand [12]. During the operation of pulsed load, the generator faces adverse situations and high transient power demand stresses prime-mover and excitation system of the generator. To maintain the power quality of the shipboard power system, the use of pulsed power compensator is a potential solution. In [13], flywheel energy storage system (FESS) is used to compensate the operation of pulsed load. In [14], the impacts of pulsed load on the shipboard power system are compared with and without energy storages. The operation of FESS is shown in maintaining the ship board power system's stability in [14]. In [15], the operation of pulsed load compensator is shown in maintaining the power quality of the system. In [16], supercapacitor based pulsed load compensator is used to support the operation of pulsed load (EMALS, and EMRG).

Switching on or off of large loads instantly from the bus has adverse effects on the power system. Adding pulsed load to the bus is a switching effect. Adding MWs of pulsed load momentarily to the bus produces large voltage and current transients. It can lead a power system to damage completely. In order to avoid the negative effects of pulsed load, in [17] FESS is added with the generators (Figure 1.4). FESS can be also used to maintain the continuity of power supply if a generator fails.

In [18], battery and supercapacitor are used as the backup energy storage devices for the shipboard power system. Buck-boost DC-DC converters with bi-directional capability are used to connect energy storages to the shipboard power system. A PI based control model is used to control the charging and discharging of the energy storages. Battery management system is designed to keep the state of charge (SOC) within 40%-80%. Here, battery is charged only when the SOC of the battery goes below 40%. From Figure 1.5, energy management subsystem is responsible

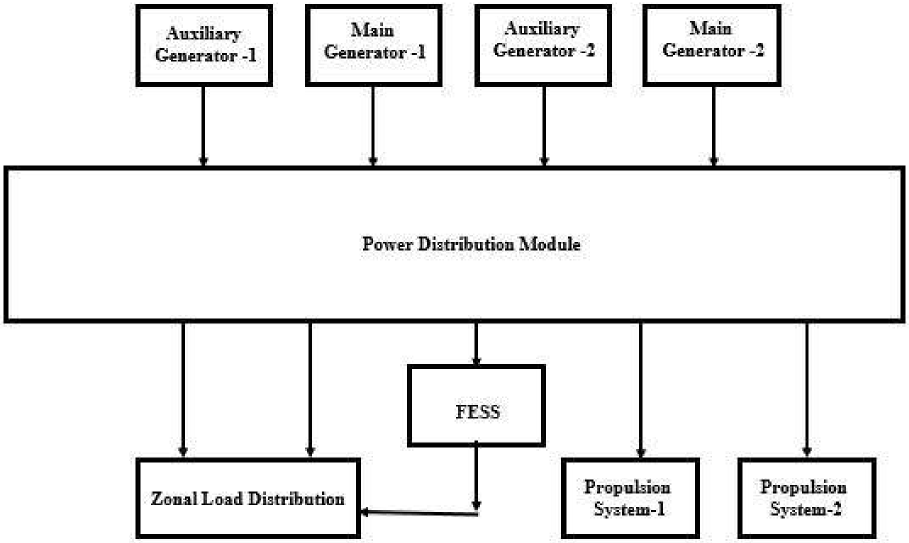

Figure 1.4: Integration of FESS with the power distribution module.

to monitor motor power and total available power from the battery and generators [18]. From the speed changes curve and look-up table, the required motor drive power (P^*_{drive}) is calculated. The required generator power (P^*_{Gen}) is calculated from the required motor drive power, (P^*_{drive}), and the battery recharge power, ($P^*_{char,bat}$) given in (1.1). Where $P^*_{char,bat}$ is negative for charging. Required battery power ($P^*_{dis,bat}$) for discharging is obtained from the subtraction of the required generator power (P^*_{Gen}) and measured generator power (P_{Gen}) according to (1.2).

$$P^*_{Gen} = P^*_{drive} - P^*_{char,bat} \tag{1.1}$$

$$P^*_{dis,bat} = P^*_{Gen} - P_{Gen} \tag{1.2}$$

In [19], fuzzy logic control technique is used to control the operation of the energy storages for naval pulsed power application. In [19], hybrid energy storage module (HESM) consisted of a lithium-ion battery (LIB) and a supercapacitor, both being used to support the generators. A simple buck-boost converter with bi-directional capability is used to control the operation of the HESM. DC bus voltage and HESM's current are used as the fuzzy input variables. DC bus voltage is used as the input variable as it is critical to maintain within the limit, and HESMs current is

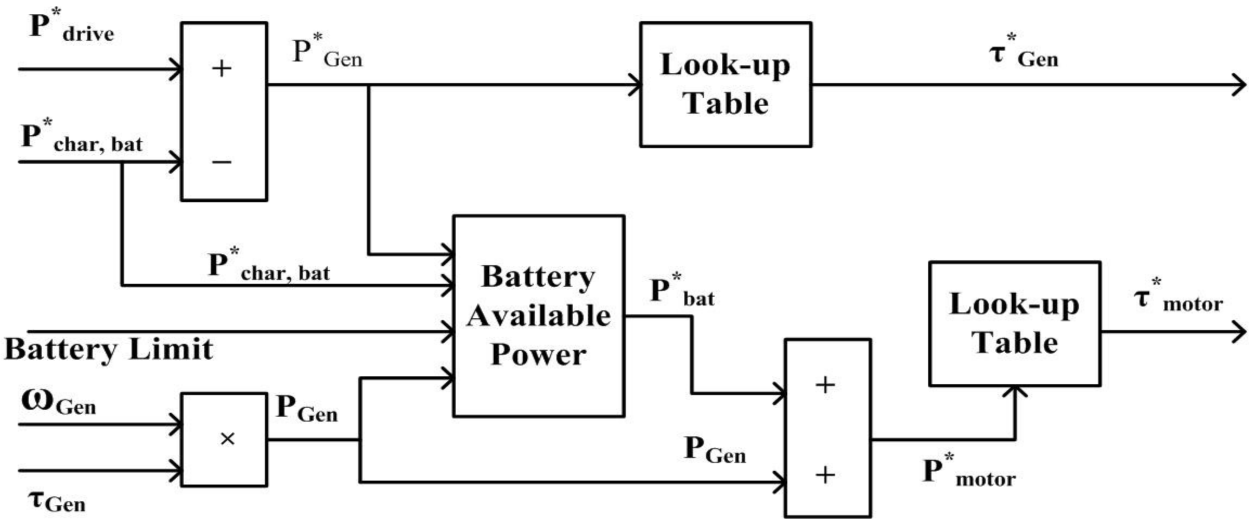

Figure 1.5: Power management system for energy storages of electric ship power system.

used as it changes with the change of the bus voltage. The output fuzzy variable is the battery current limit as it has superb control over the HESM.

In [20], three potential positions of incorporating energy storages are described. From Figure 1.6, the first potential option is to add the energy storages with power conversion module (PCM)-2A. In this location, the energy storages can provide the best survivability and quality of service (QOS) to the vital loads. Energy storages are added very near to the location of the vital loads which make them to act as reliable sources of power for the vital loads. The main drawback of this option is that energy storages cannot support the generators and supply power to the propulsion motors. They also do not help to maintain the bus voltage. Moreover, the emergency loads connected to PCM-1A do not get any support from the energy storages. The second potential option is to add energy storages within PCM-1A. In this position, energy storages can support all the zonal loads. But they cannot provide QOS and survivability for the critical loads connected across PCM-2A like as the option 1. In this option, energy storages cannot support the generators directly to maintain bus voltage and to meet power demand of the propulsion loads. Another potential option is to add energy storages with ports or starboards on the longitude bus with 5kV MVDC bus voltage. In this option, energy storages can support generators to maintain bus voltage and supply power to the propulsion loads. This option is economical as the number of required energy storages is reduced compared to the other two options. The main disadvantage is that the QOS and survivability for the critical loads provided by the energy storages in this position is lower than the previous two options.

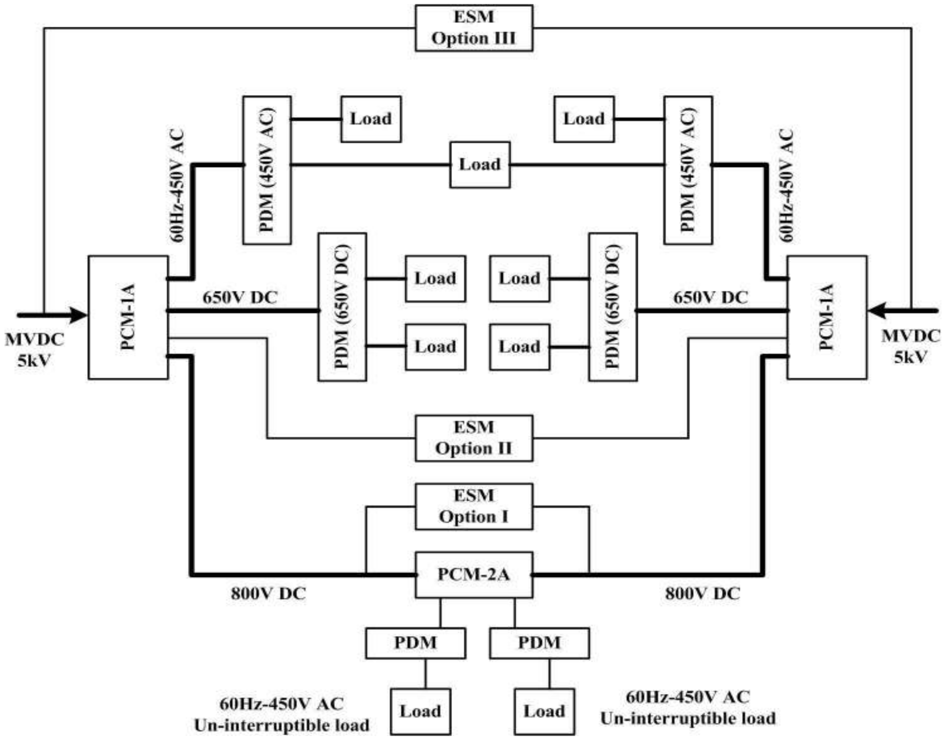

Figure 1.6: Potential positions of energy storages in shipboard power system [20].

Pulsed load needs high amplitude power within a very short time. The IPS structure based MVDC system faces difficulty to support pulsed load. In [16], to support pulsed load , supercapacitor based energy storage system is used. Figure 1.7 shows supercapacitor based pulsed power system proposed in [16]. Here all the supercapacitor are connected together to support pulsed load. Energy storage management systems for a local DC distribution system of More Electric Aircraft are proposed in [21]. To ensure voltage stability, energy efficiency and storage availability, energy management strategies based on PI control and FL control are proposed. To compare different strategies, voltage performances and efficiency are observed. Supercapacitor is used as the energy storage. Conventional buck-boost converter is used to connect the supercapacitor to the DC test system.

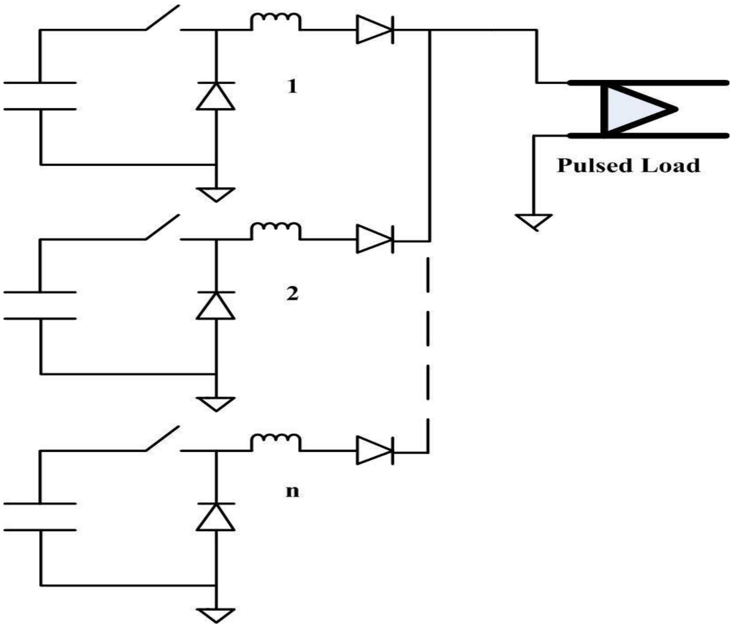

Figure 1.7: Supercapacitor based pulsed power system.

Composite energy storages (battery and supercapacitor) are used for microgrid application with photovoltaic (PV) generation in [22]. Because of intermittent nature of PV generation, energy storage with high energy density (example: battery) is required. To prevent load fluctuations, high power density energy storage (example: supercapacitor) is suitable for the microgrid. Modular interleaved bidirectional DAB converters are used to connect the HESS with the microgrid.

1.2 Motivation and Objective

The extensive electrification of ship power leads to the concept of AES with power demand to reach hundreds of MW in the near future [5]. To overcome the technical challenges related to the generation, distribution and optimization of such large electrical power, it is required to redesign the power system architecture of the AES. A promising solution is to design an IPS which is based on a MVDC power system [23].

Warships have intermittent weaponry loads (EMALS, and EMRG) along with the propulsion load, ship service load and radar load. Due to the transient nature of the weaponry load, it demands impulsive power of very high amplitude. Traditional generators are not capable of supporting the transient load demand as these have relatively long time constants for control of fuel valves &

combustors, mechanical inertia etc. To meet the transient power demand of the MVDC power system, the energy storage technology is an essential part of the MVDC ship board system [24–26]. The storages are capable of supporting sudden load demand and reduce the negative effects on power quality. The energy storage system also helps to maintain the MVDC bus voltage within desired margin which is usually 10% around the nominal voltage [27]. Conventional warships use gas turbine as the prime mover for propulsion system. For AES, it will be coupled to the generator to produce electrical energy. In some cases, the generated electrical energy can exceed the total load demand of the MVDC system. The excess energy can then be stored in the energy storages and returned to the system when needed.

There are two modes of operation of the ESM system. The normal operation of the ESM system is to maintain the power balance between the load and generation. The transient mode of operation of the ESM system is to prevent power fluctuations. It is difficult for a single type of energy storage to perform efficiently both type of operations. For meeting the steady power demand of the MVDC system, an energy storage with high energy density is required. For the purpose of supplying transient power demand, an energy storage with high power density is required. If the battery is used as the only energy storage, then it has to be oversized to take care of transient power demand. If the supercapacitor is used as the only energy storage, then it is needed to increase the size of the supercapacitor. The supercapacitor cannot support the load for a long time as the supercapacitor energy density is low. The use of HESS is a promising solution to meet the transient and steady power demand [22].

Now the main issue is to design an intelligent ESM system to control the operation of the energy storages. The key function of this ESM system is to properly balance the power demand of the sources and loads, to support the generators during transient operations and pulsed load activation. In order to support the MVDC system, the ESM system needs to control the charging and discharging of the energy storages.

Some power management strategies with hybrid energy storage systems (batteries and supercapacitors) are presented in ([28–31]) for hybrid electric vehicles. In [28], the FL control technique is used to control the operation of the battery and supercapacitor to support the fuel cell for electric vehicular applications. The operation of energy storage management system for more electric aircraft is discussed in [21]. The use of battery as energy storage with the photovoltaic (PV) and wind power generation are discussed in [32]. In [19], fuzzy logic based control is used for managing hybrid energy storage module for naval pulsed power applications, but the state of charge of the HESS was not considered in designing fuzzy logic controller. Fuzzy logic based control strategy is used in [33] for energy management of a hybrid ship, but the operation of pulsed load is not considered. In [34] and [35], supercapacitor's voltage and SOC are used as fuzzy logic control variables but they did not consider voltage and SOC of the battery. Bus power and voltage difference of the battery and supercapacitor are used for determining output reference power in [36], but SOC of the battery and supercapacitor are not considered. In [37], fuzzy logic strategy is used for selection of energy storages for smart grid applications.

The main objective of this research is to design an ESM system for proper management of charging and discharging of the energy storages based on SOC. The main function of the ESM system is to generate total storage reference power signal for charging and discharging of the energy storages. In order to generate the reference power signal, the ESM system needs to consider the transient power demand and whether the total power demand of the load exceeds the total generation capacity. The ESM system maintains power balance between the generation and demand by controlling HESS. The ESM system also needs to ensure the efficient and optimal utilization of the energy storage for making the MVDC system of AES cost-effective. One of the main objective of this research is to use HESS composed of battery and supercapacitor, an strategy for separation of total storage reference power between high energy density device (battery) and high power density device (supercapacitor) is required to implement. Another objective of this research is to design a deep discharging and overcharging protection controller to save the energy storages from the damages due to overheating during deep discharging and overcharging. One of the aim of this research is to incorporate multiple batteries and supercapacitors in the ship board system. In order to add multiple batteries and supercapacitors to the AES, algorithms for power sharing among multiple energy storages are required to design. The final goal of this research is to validate the results of the offline simulation of the ESM system by CHIL based testing.

1.3 Phases of the Research

Figure 1.8 shows the the phases of the research according to which this research study progressed. As different technologies are used for this research, different phases required its own literature reviews and studies. The goal of phase-1 is to find the suitable energy storages for the MVDC system of AES. There are lots of energy storages with different energy densities, power densities, sizes, weights, life times, efficiencies, costs. As the size of the ship is fixed and the energy storages need to meet the steady and transient power demand, it is required to find the suitable energy storages for the shipboard power system. In phase-2, the electrical models of the suitable energy storages (battery and supercapacitor) are developed and tested with individual load. In this phase, different kinds of bi-directional DC-DC converters are studied for power transfer among the MVDC system and the energy storages. DAB converter with galvanic isolation is selected for its superior characteristic. The average model of the DAB converter is developed and it is tested with loads, DC source and energy storages. Phase-3 is the hardest part of this research. In this phase, a time domain simulation model of the MVDC system is developed with different components as described in the IEEE standard 1709. The MVDC system has two gas turbine based generators, MMC converters, propulsion loads, ship service loads, pulsed load, radar load, energy storages, DAB converters. The challenging part of this phase is to interface different components of the MVDC system. In phase-4, FL based ESM system is designed to control the power transfer among the energy storages and the MVDC system. The input variables of the fuzzy logic supervisor are the difference between the total generated current and the total reference current, the MVDC bus voltage and the SOC of the battery and supercapacitor. In phase-5, in order to perform a comparative study, a PI based ESM system is designed for the control of the energy storages. The FL and PI based EMS systems performances are compared for different conditions of SOC. In phase-6, for installation of multiple energy storages distributed around the ship, two power sharing strategies are designed and implemented. In phase-7, the FL and PI based ESM systems with the MVDC shipboard system are modeled in real-time simulator Opal-RT. In phase-8, FL and PI based ESM system are implemented in field-programmable gate array (FPGA) (Vertex 707) and CHIL based validation are performed.

1.4 Thesis Outlines

The chapters of this thesis are arranged according to the phases of the research. In chapter-1, motivation and objectives of this research were discussed. A brief introduction about the potential

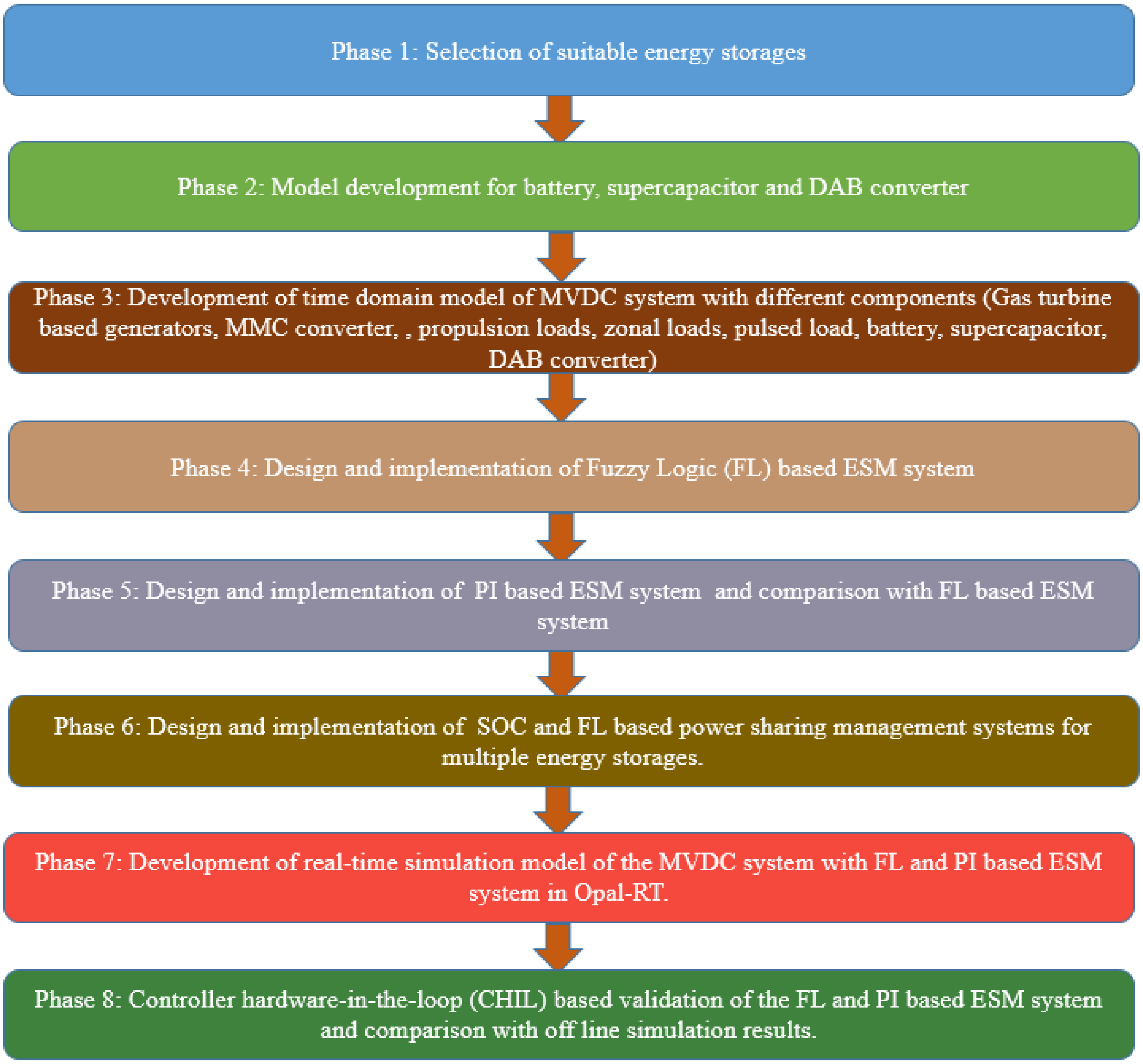

Figure 1.8: Block diagram of the different phases of this research.

use of using energy storages in shipboard power system is also given in chapter-1. The synopsis of different phases of this research is given in the first chapter. In chapter-2, potential energy storages for shipboard power system are introduced. In this chapter, the basic working principles of the battery, supercapacitor, SMES, and FESS are summarized. Their pros and cons related to the applications for shipboard power system are discussed concisely. The significances of using HESS are analyzed at the end of this chapter. Chapter-3 contains the detail description about the modeling of the components of shipboard power system. The advantages of the MVDC based IPS structure are explained at the beginning of this chapter. The working principles and corresponding diagrams are given for the components (generators, MMC converters, propulsion systems, bi-directional DC-DC converter, battery, supercapacitor, pulsed load, ship service loads, radar loads, cables) of the shipboard power system. In chapter-4, the designs of the energy storage management systems (FL and PI based) are explained elaborately. At the end of this chapter, two power sharing strategies are given for the installation of the multiple energy storages units in the shipboard power system. Chapter-5 contains the simulation results regarding the performances of the FL and PI based ESM systems. In this chapter, the applications of the energy storages are shown for the management of the transient and steady power demand. The operations of the pulsed load and the supportive behavior of the energy storages are illustrated in this chapter. The simulation results of the FL and PI based ESM systems with the different condition of SOC of the energy storages are given in this chapter. Later the comparison of the performances of the FL and PI based ESM systems are shown. The operations of the two power sharing strategies are shown in the chapter-5. Finally, CHIL based experimental results are added at the end of the chapter-5 to validate the offline simulation of the FL based ESM system. Chapter-6 contains conclusion and future work.

CHAPTER 2

POTENTIAL ENERGY STORAGES FOR SHIPBOARD POWER SYSTEM

In order to minimize size, weight, and to increase system efficiency of the shipboard power system, the selection of proper energy storages has become very important. Determining the type of energy storages, load profile and the generation profile of the shipboard power system plays an important rule. For ship power system, energy storages have two modes of operations: (1) normal mode and (2) transient mode. During normal operation, energy storages are required to maintain the load balance, and during transient mode they mitigate the effects of load variations. A single type of energy storage cannot perform these tasks efficiently. For energy balance, energy storages with high energy density are required. For mitigating the load variation, high power density energy storages are required. High energy density energy storages such as battery can be used for normal operation due to their high energy density characteristic, whereas high power density energy storages such as supercapacitors, FESS, and SMES can be used for fast dynamic response due to their high power density characteristic [38]. A Pugh chart is given in Figure 2.1 to show relative advantages and disadvantages of the potential energy storage technologies relative to lead-acid battery. Lead-acid battery is chosen for comparison as U.S. Navy are very familiar with this energy storage [39].

The size of energy storages can be optimized to support the generators for peak power demand. Energy storages can be used to support critical loads for example emergency lights and signals, internal communications, navigational radar, weapons and sensors [40]. Incorporation of energy storages in the shipboard power system will increase system's survivability, redundancy, and efficiency [6]. Though there are lots of available energy storage technologies but due to some specific requirements of the shipboard power system, the number of energy storages technologies capable of meeting the desired demands of AES are relatively few. As the size of the AES is limited, the sizes and weights of the energy storages are big issue. In order to feet the energy storages with the shipboard power system, some major characteristics of the energy storages for example energy storage capacity, specific energy, energy density, power density, life time, round-trip efficiency, capacity degradation, complexity, cost, and safety issue are required to be considered. In the following subsections a brief description about the potential energy storages for the shipboard power system application is given.

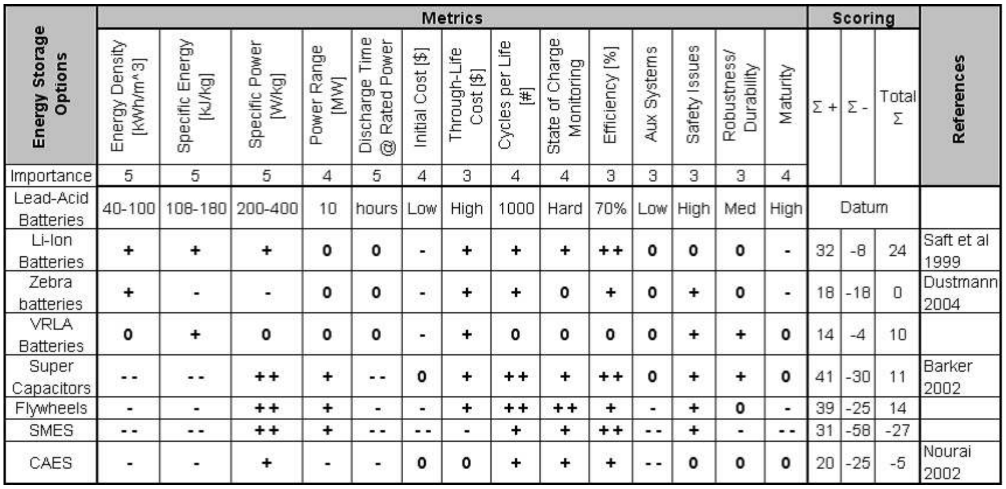

Energy Storage Options	Metrics														Scoring			References
	Energy Density [kWh/m^3]	Specific Energy [kJ/kg]	Specific Power [W/kg]	Power Range [MW]	Discharge Time @ Rated Power	Initial Cost [$]	Through-Life Cost [$]	Cycles per Life [#]	State of Charge Monitoring	Efficiency [%]	Aux Systems	Safety Issues	Robustness/ Durability	Maturity	Σ +	Σ -	Total Σ	
Importance	5	5	5	4	5	4	3	4	4	3	3	3	3	4				
Lead-Acid Batteries	40-100	108-180	200-400	10	hours	Low	High	1000	Hard	70%	Low	High	Med	High	Datum			
Li-Ion Batteries	+	+	+	0	0	-	+	+	+	++	0	0	0	-	32	-8	24	Saft et al 1999
Zebra batteries	+	-	-	0	0	-	+	+	0	+	0	+	0	-	18	-18	0	Dustmann 2004
VRLA Batteries	0	+	0	0	0	-	+	0	0	0	0	+	+	0	14	-4	10	
Super Capacitors	- -	- -	++	+	- -	0	+	++	+	++	0	+	+	0	41	-30	11	Barker 2002
Flywheels	-	-	++	+	-	-	+	++	++	+	-	+	0	-	39	-25	14	
SMES	- -	- -	++	+	- -	- -	-	+	+	++	- -	+	-	- -	31	-58	-27	
CAES	-	-	+	-	-	0	0	+	+	+	- -	0	0	0	20	-25	-5	Nourai 2002

Figure 2.1: Pugh Chart of Energy Storage Technologies [6].

2.1 Battery

A battery is an electrochemical device. It is the most familiar technology to store electrical energy. It can store energy in the form of chemical energy and convert chemical energy directly into electrical energy by means of oxidation-reduction reactions. For a battery, the chemical reactions occur in a cell where two electrodes are set in to an electrolyte. The reactions involve the transfer of electrons from one electrode to the other through an external electric circuit/load. Figure 2.2 shows the simple architecture of a battery [41]. Battery modules are connected in series or in parallel to get the required voltage and current. The advantages of the battery are high energy density, high round trip efficiency, cycling capability. The life span of the battery is also reliable and initial cost of installation is low. The concerns with the battery are deep discharging and overcharging and heat due to deep discharging and overcharging that reduces the lifetime of the battery.

Compared to other batteries, lead-acid battery is the most familiar energy storage technology for our daily life. It has been representing an established and matured technology for storing

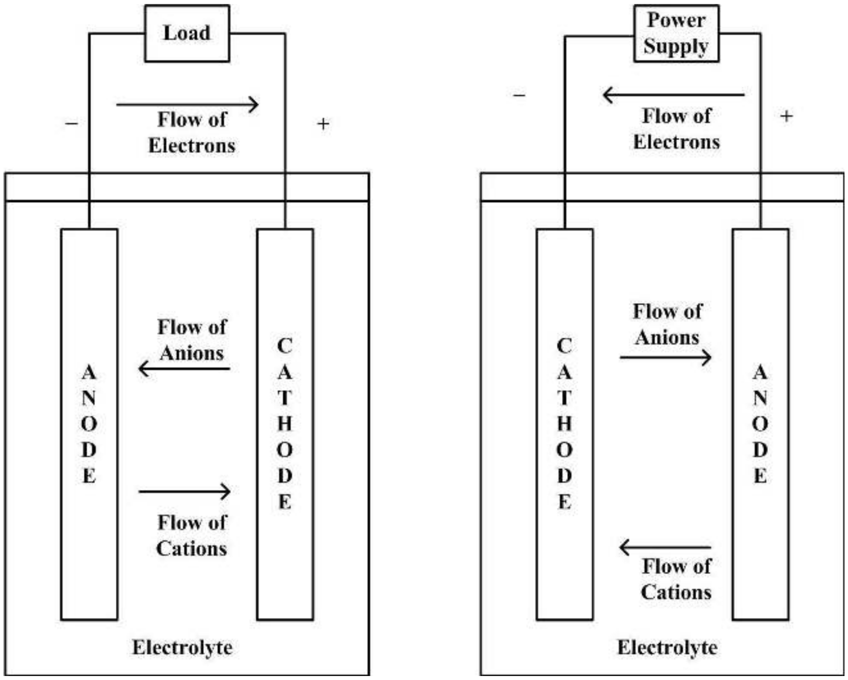

Figure 2.2: A simple battery with different conditions.

electrical energy in the form of chemical energy for many years. It can be used to store bulk energy and for rapid charging and discharging. Research have been going on to improve energy density and charging characteristics of lead-acid battery.

Lithium-ion battery is a new technology for storing electrical energy. Figure 2.3 shows the diagram of lithium-ion battery. A Li-ion battery has a high energy-to-weight ratio and low self-discharge loss [42, 43]. In Li-ion battery, Graphite is used as negative electrode and lithiated metal oxide (Lithium cobalt (III) oxide ($LiCoO_2$), Lithium nickel dioxide powder ($LiNiO_2$) or $LiMnO_2$) is used as positive electrode. The electrolyte is a lithium salt such as Lithium hexauoro phosphate ($LiPF_6$) or Lithium perchlorate ($LiClO_4$). The negative and positive electrodes take part in a chemical reaction in lithium-ion battery where the electrolyte provides a conductive medium for lithium-ions. During charging, positive lithium ion moves from the negative electrode (usually graphite) and enters the positive electrode (lithium oxide) and for discharging process, the reverse chemical reaction occurs. The positive and negative electrode half-reaction are given in (2.1) and (2.2).

The positive electrode half-reaction is [44]:

$$LiCoO_2 \rightleftharpoons Li_{1-x}CoO_2 + xLi^+ + xe^- \tag{2.1}$$

The negative electrode half-reaction is:

$$xLi^+ + xe^- + xC_6 \rightleftharpoons xLiC_6 \tag{2.2}$$

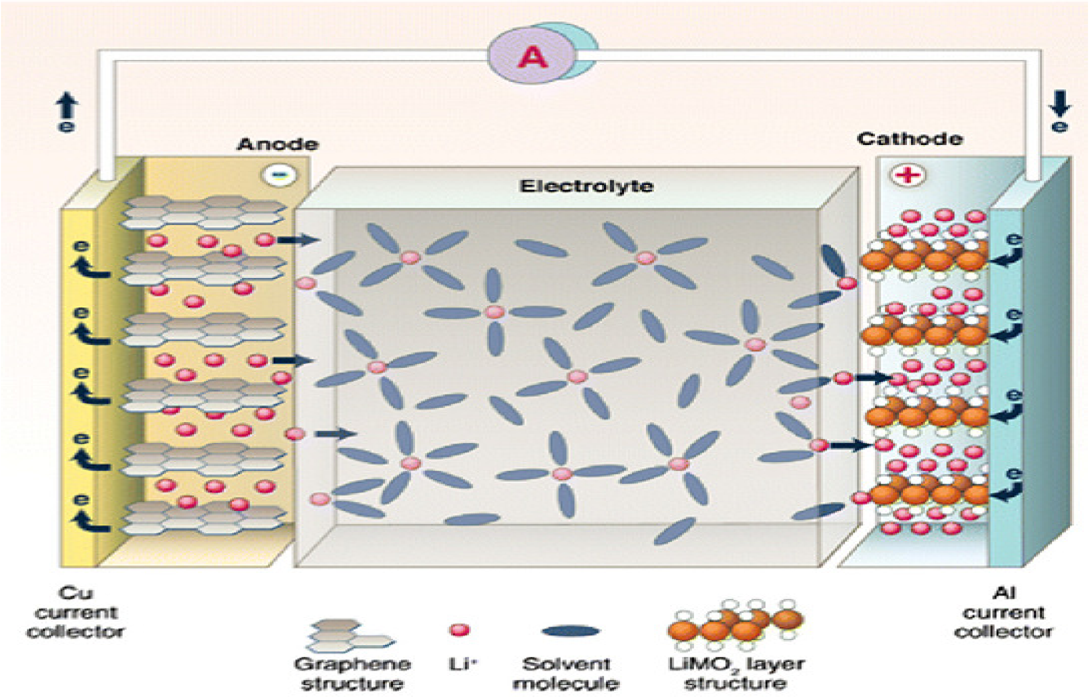

Figure 2.3: Schematic diagram of a Li-ion battery [45].

Lithium-ion battery shows several superior capabilities comparing to lead-acid battery in case of power density, energy density, life time and round-trip efficiency. The comparison of lead acid and lithium ion battery is shown in Table 2.1 in terms of different characteristics.

Table 2.1: Characteristics of Lead Acid and Lithium-ion Batteries [46, 47]

Characteristics	Lead acid	Lithium ion
Energy Density (Wh/L)	54-95	250-360
Specific energy (Wh/kg)	30-40	110-175
Depth of discharge (DOD)	50%	80%
Temp range of Charge	-40°C - 27°C	-20°C - 55°C
Efficiency	75%	97%
Replacement timeframe (year)	1.5-2	5-7

2.2 Supercapacitor

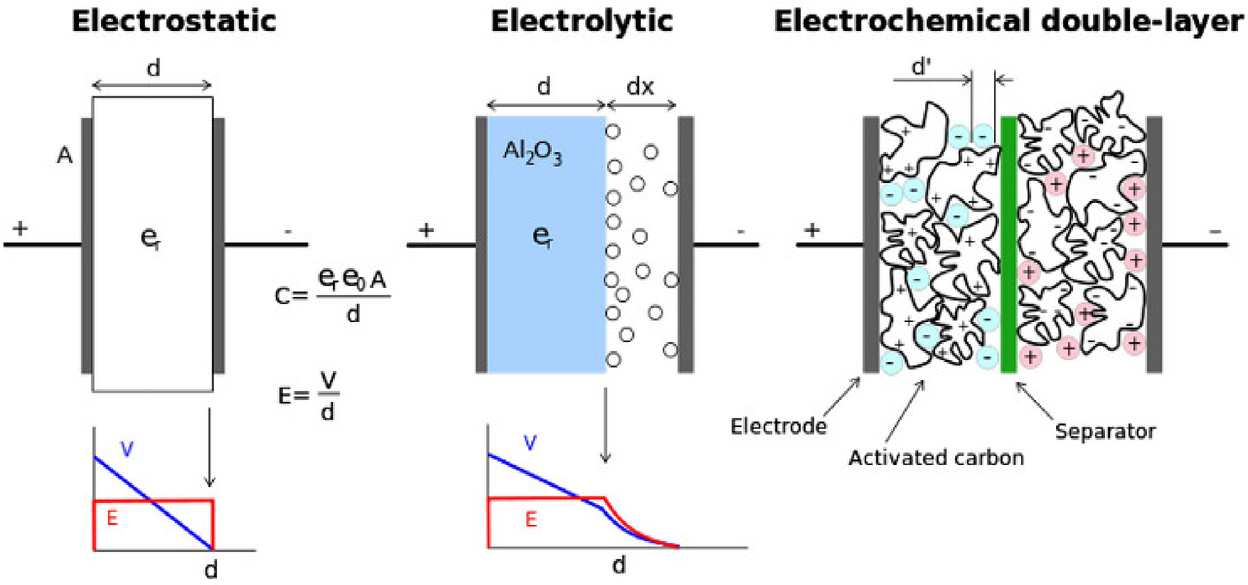

Figure 2.4: Schematic diagrams of three types of capacitors [48].

Capacitor offers a direct storage of electricity. It can store and deliver electricity at a very fast rate. It can process several thousands charging/discharging cycles without material degradation compared to batteries. Its fast charging and discharging rate made it suitable for transient voltage stability applications [49–51]. Both the electrostatic and electrolytic capacitor store energy through two parallel plates separated by a dielectric material. For electrostatic capacitor, dielectric is used for the separation of the plates, but for electrolytic capacitor, liquid electrolyte (aluminum oxide) is used. For electrochemical double-layer capacitor (supercapacitor) electrolyte solution (propylene carbonate) is used between two plates, instead of dielectric [42, 43]. Their structural schematics are shown in Figure 2.4. Though the energy and power density of supercapacitor are higher than the conventional capacitor, still energy density is lower than the battery [50, 51]. Supercapacitor bridges the gap between conventional capacitors and rechargeable batteries.

2.3 Superconducting Magnetic Energy Storage (SMES)

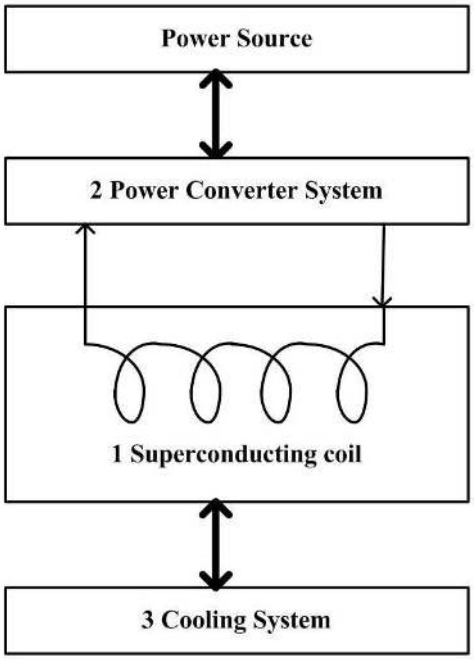

Figure 2.5: A simple structure of SMES.

SMES uses superconducting coil to store electrical energy in the form of magnetic energy. It stores magnetic energy by creating magnetic field with the flow of direct current (DC) through the superconducting coil. SMES shows the same kinds of advantageous characteristics like supercapacitor (high power density, high energy storage efficiency, long application lifetime and few environmental pollution). A typical SMES system includes three major parts [52] (shown in Figure 2.5): 1) superconducting coil 2) power conditioning system (PCS) 3) cryogenically cooled refrigerator. During charging process, the PCS converts AC energy to DC energy and maintains a positive voltage across the superconducting coil for charging. The superconducting coil uses DC current to create magnetic field and store electrical energy as magnetic energy. During discharging process, the PCS acts as a load across the coil, produces a negative voltage across the superconducting coil, and causes the superconducting coil to discharge. The Cryogenically cooled refrigerator is used to maintain the temperature of the superconducting coil below the critical temperature [53].

Though it is advantageous like a supercapacitor, it is very costly and it has significant auxiliary equipment. In order to maintain the superconducting characteristics of the magnetic coil, the coil must be placed in liquid helium to get the temperature below -260°C [54]. It is very costly to maintain this kind of very low temperature. It is also required to install additional equipment for cooling. It is yet not suitable for use in the shipboard power system as it lacks of robustness to unpredictable environment.

2.4 Flywheel Energy Storage (FES)

Flywheel is an electromechanical energy storage device which stores energy in the rotation of a cylindrical rotor. A FES device is composed of five major components: flywheel, bearings, electrical rotating machine, power electronics converter, and a vacuum chamber [55]. Figure 2.6 shows the simple schematic diagram of a flywheel energy storage system [54]. The rotating machine is connected to the flywheel. The rotating machine can work as a generator or motor depending on the power demand. During charging process, electrical energy is used to accelerate the flywheel and it stores energy in the form of kinetic energy. At this condition, a rotating machine works as a motor. During discharging process, the flywheel decelerates and delivers electrical energy to the connected load. At this condition, the rotating machine works as a generator. The energy storing capability of flywheel energy storage system depends on the rotating speed of flywheel and its inertia.

FES has significant advantages for using power system application as it has high cycle life and power density. It can meet high power demand for only a short time. The main shortcomings of using FES are low energy density, high self-discharge and additional auxiliary equipment. As it has low energy density, it cannot be used as standalone backup power. It has to be used with other high energy density storage device like a battery. Another significant drawback of using flywheel is very high self-discharging (nearly 20% of stored capacity per hour) [41]. For high self-discharging,

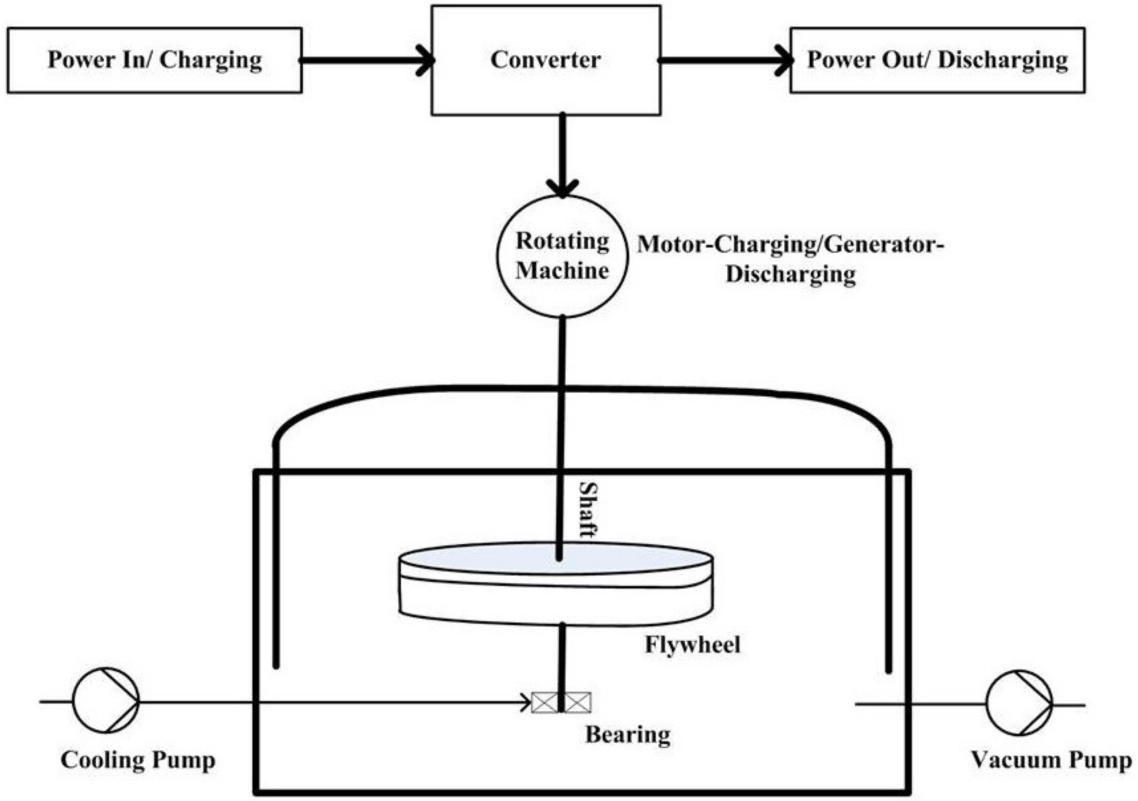

Figure 2.6: Schematic diagram of flywheel energy storage system.

it can store energy for a very short time and is not suitable for using longer storage time. Another drawback of not using FES in the shipboard power system is that it has large auxiliary equipment. The flywheel of FES is needed to put in high vacuum environment for reducing energy loss due to air resistance. To increase the energy storage capacity of FES, high-strength composite materials can be used to form the rotating mass with low inertia and high-velocity rotor. The cost of FES system made of composite materials will be higher than the FES system made of conventional materials. With the increase of speed, concerns related to safety will increase. The worst scenario can be sudden disintegration of the rotor. For solving the problem with high speed, it is required to increase the volume, mass and complexities [6]. For reducing self-discharging, superconducting magnetic bearing and high vacuum chamber can be used. Eventually, it will increase the cost for maintaining very low temperature of the superconducting magnetic bearing [54].

From the above discussion, it is clear that battery and supercapacitor are the potential energy

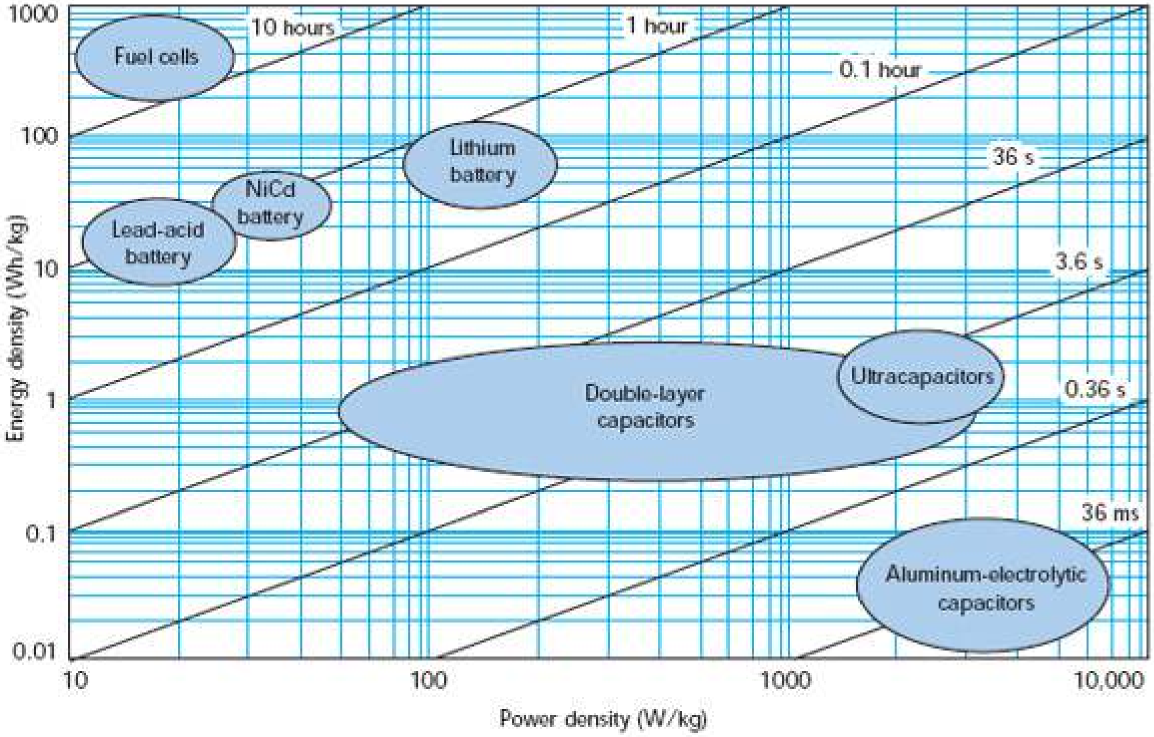

Figure 2.7: The Ragone chart of different energy devices and their relative power and energy densities [22].

storages for shipboard power system. As there are two modes of operation of energy storages: one is load balancing and the another is preventing load fluctuations. For each mode, ship power system requires different energy storages. A single battery or single supercapacitor is not capable of performing both the operations, as the battery has a higher energy density than the supercapacitor, and that characteristic is required for load balancing. But for preventing load fluctuations and meeting pulsed load demand, an energy storage with high power density is required, however, the battery has a lower power density than the supercapacitor. Figure 2.7 shows power and energy density of different energy storage devices. So, the best solution for AES is incorporating HESS in the shipboard composed of high energy density devices (battery) and high power density devices (supercapacitor).

CHAPTER 3

MVDC SYSTEM AND IT'S MODELING

3.1 Advantages of IPS Structure Based MVDC System

In the near future, warships will be incorporated with high electric power demanding weapons and sensors. The EMALS and EMRG will be added to the future warships with high power sensors. To keep pace with the supply of high electric power demand, it is required to change the shipboard power system to an IPS architecture based on a MVDC power system [56]. In this IPS structure frame, total ship loads (propulsion load, ship service load, pulsed load, radar load) will be served electrical power in an integrated concept. For a traditional ship, it is required to have the separated power generation facilities for a ship service distribution [3]. But for the new AES, all ship service loads including propulsion loads will be powered from the same electrical sources [57]. Benefits of IPS structure are fewer prime movers and improved fuel savings. It also increases flexibility in locating prime movers and improves survivability [3]. In this new IPS architecture frame, there will be very few amounts of mechanical parts and most of the components of the system will be energized electrically. This extensive electrification of ship power leads to the concept of the AES. The radical change from mechanical propulsion system to electric propulsion system will increase electrical power demand of the shipboard [58]. The electric power demand of AES will reach hundreds of MW in the near future.

Traditionally, all loads of a shipboard can be supplied by a single DC feeder. But in this single DC feeder architecture frame, all ship loads are provided electrical power from a single cable line. The current of the single DC feeder line is high at full load. So, a very large cable conductor with high cross section are required to flow high current. Further, the single DC feeder architecture frame is responsible for outages of the whole system for the failure of a single load. If for example, a fault occurs at the cable line connecting the active rectifier with the nearest test bench, this line will have to be switched off. This will create power outages at remote locations of the feeder. But the new IPS ring structure has the facility to avoid the shut down the whole grid even if there is any fault between two terminals. Moreover, it helps to isolate the faulty part of the grid and keep the continuity of operation of the rest of the grid [59].

The new MVDC system architecture is advantageous over the AC system as there is no need to maintain a common frequency. For paralleling power sources, it is required only to match the voltage, not frequency or phase. This MVDC architecture frame also helps power conversion equipment to operate at high frequencies which eventually helps to reduce the size of the transformer. There is no problem of skin effect loss like AC system and the full cross section of a DC system is used for power transmission. There is also no concern about power factor matching [56].

3.2 Notional MVDC System of Shipboard

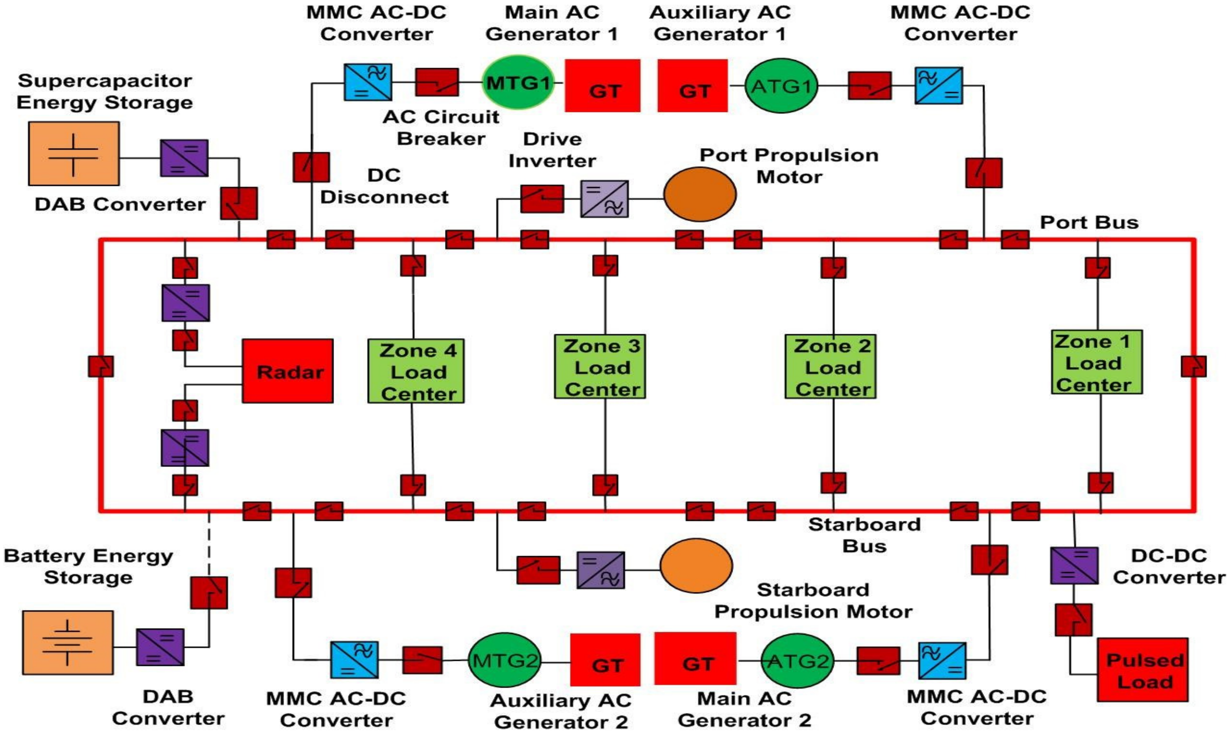

Figure 3.1: Notional MVDC power system [27].

The notional MVDC power system of AES with IPS structure is discussed in [27, 60]. The IPS structure of the MVDC system increases the operational capability of the electric shipboard under adverse condition. Figure 3.1 shows the notional MVDC system. The MVDC system has two

Main AC Turbine Generators (MTG1, MTG2) and two Auxiliary AC Turbine Generator (ATG1, ATG2) as the source of power. The generators are connected to the MVDC system via modular multilevel converter (MMC). The capability of high energy conversion makes it suitable for using MVDC and HVDC systems [61]. MMC converter shows modularity and scalability in the case of meeting voltage requirements compared to other voltage source converters [62]. The total load of the MVDC system is divided into propulsion load, ship service load, radar load. It has also pulsed load as electric weaponry system. In order to maintain the bus voltage within the limit and supporting the generators when the total load requirement exceeds the total generation capacity, HESS are added to MVDC system consisting of the battery and supercapacitor. The HESS are connected to the MVDC system via DAB DC-DC converters with bi-directional capability of power conversion. The whole system is modeled and simulated in Matlab/simulink environment. The modeling of the MVDC system components are described in the following sections.

3.3 Generators

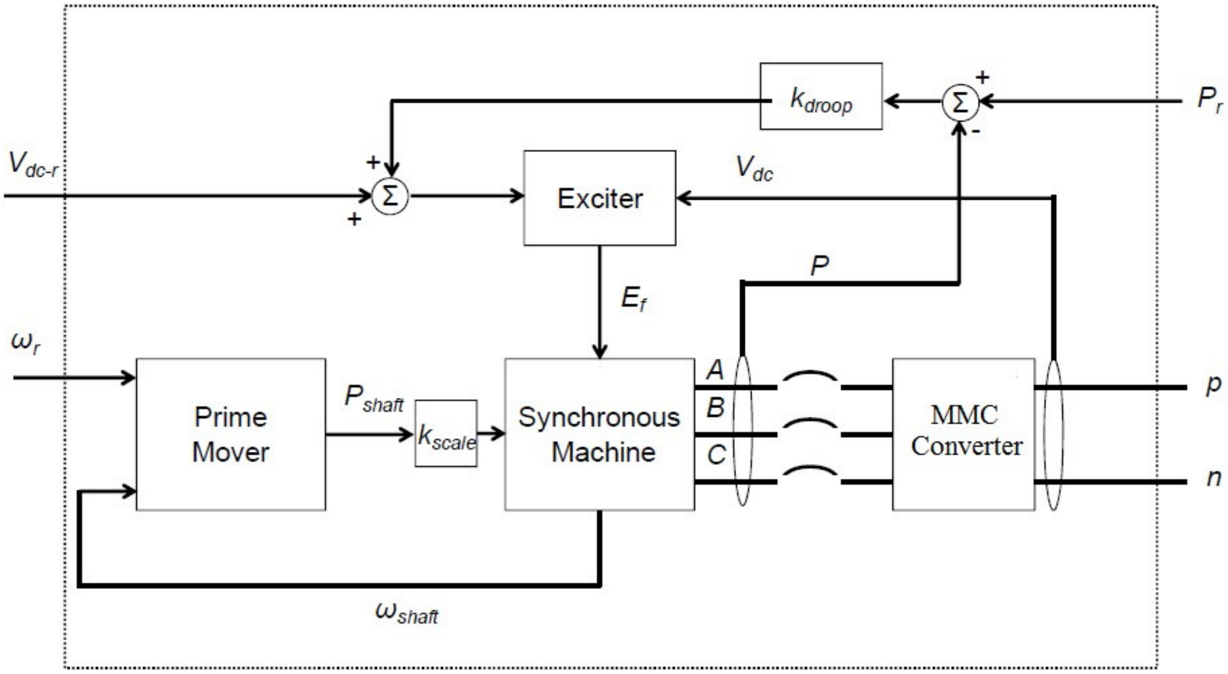

Figure 3.2: Main generator sets for baseline MVDC system [63].

The main generators (MTG1, MTG2) of the ship power system are consisted of twin-shaft gas turbine as governor or prime mover, round rotor synchronous machine, IEEE Type AC8B excitation system. Figure 3.2 shows the generator architecture for MVDC power system of the shipboard. The generators are connected to the MMC converters for AC-DC power conversion. The MMC converters are connected to the main ring bus. The inputs of the prime mover are the reference synchronous speed, ω_r and the output shaft speed, ω_{shaft} of the synchronous motor. The output of the prime mover is shaft power, P_{shaft}. It is passed to the synchronous machine after scaling. The excitation system also provides winding excitation voltage, E_f, to the synchronous machine. The difference between reference power, P_r and the measured power, P, of the synchronous machine is passed to a droop controller. The output of the droop controller and the reference DC voltage, V_{dc-r}, are summed and then passed to the excitation system. The output voltage of the MMC converter is measured and passed to the excitation system. The output of the excitation system is field excitation voltage, E_f, which is passed to the synchronous motor. For auxiliary generators, instead of twin-shaft gas turbine, single-shaft gas turbine is used.

3.3.1 Notional Twin Shaft Gas Turbine

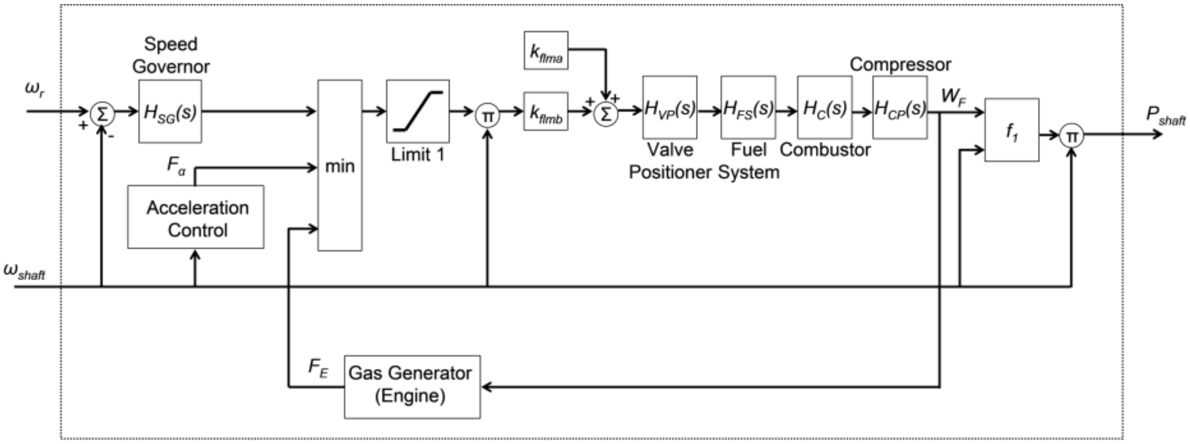

Figure 3.3: Notional twin-shaft gas turbine model [63].

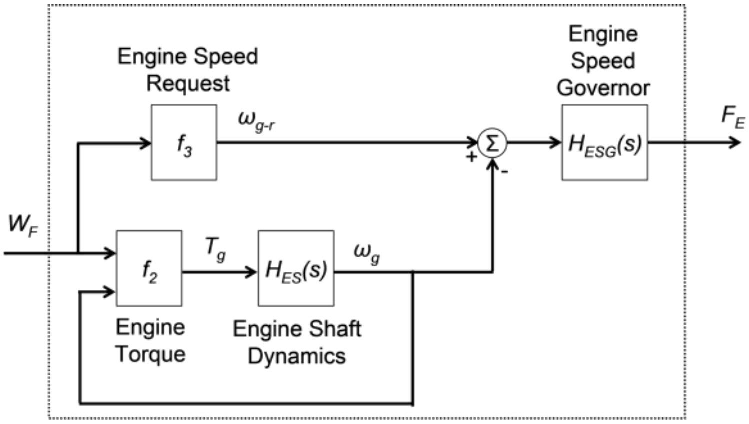

Figure 3.4: Gas generator (engine) model for notional twin-shaft gas turbine model [63].

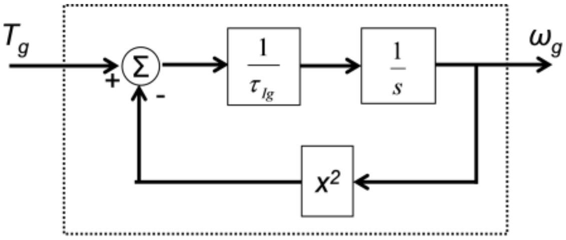

Figure 3.5: Engine shaft dynamics of gas generator (engine) model for notional twin-shaft gas turbine model [63].

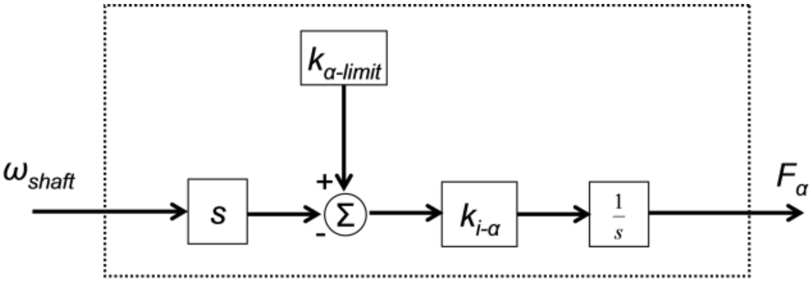

Figure 3.6: Acceleration control for notional twin-shaft gas turbine model [63].

The notional twin-shaft gas turbine model is shown in Figure 3.3. Figure 3.4 shows the gas generator model and Figure 3.5 shows the engine shaft dynamics. Figure 3.6 shows the acceleration control diagram. The regarding equations for twin-shaft gas turbine model are given from (3.1) to (3.9) [63]. The parameters and default values for the notional twin shaft gas turbine model are given in Table 3.1.

Table 3.1: Parameters for Notional Twin-Shaft Gas Turbine Model [63]

Parameter	Description	Default Value
a	Valve positioner constant	1
b	Valve positioner constant	0.05
c	Valve positioner constant	1
k_{flma}	No-load fuel parameter	0.2
k_{flmb}	No-load fuel parameter $(1 - k_{flma})$	0.8
k_{EFR1}	Engine speed request function slope	0.25
k_{EFR2}	Engine speed request function intercept	0.75
$k_{\alpha-limit}$	Acceleration limit (pu/s)	0.01
$k_{i-\alpha}$	Acceleration control integral gain	100
$L_{lower-Limit1}$	Lower limit for limit block "Limit 1" (fuel limit)	-0.1
$L_{upper-Limit1}$	Upper limit for limit block "Limit 1" (fuel limit)	1.5
T_c	Combustor delay time (s)	0.01
W	Speed governor constant	25
W_E	Engine Speed governor constant	30
X	Speed governor constant	0
X_E	Engine Speed governor constant	1
Y	Speed governor constant	0.01
Y_E	Engine Speed governor constant	1
Z	Speed governor constant	1
Z_E	Engine Speed governor constant	0
τ_{lg}	Time constant for engine shaft dynamics (s)	8
τ_{FS}	Fuel system time constant (s)	0.4
τ_{CP}	Compressor discharge volume time constant (s)	0.2

$$H_{SG}(s) = \frac{\frac{W(sX+1)}{Z}}{1 + s\frac{Y}{Z}} \tag{3.1}$$

$$H_{VP}(s) = \frac{\frac{a}{c}}{1 + \frac{b}{c}s} \tag{3.2}$$

$$H_{FS}(s) = \frac{1}{1 + \tau_{FS}s} \tag{3.3}$$

$$H_C(s) = e^{-sT_c} \tag{3.4}$$

$$H_{CP}(s) = \frac{1}{1 + \tau_{CP}s} \tag{3.5}$$

$$f_1(W_F, \omega_{shaft}) = \frac{1}{k_{flmb}}(W_F - k_{flma}) + 0.6(1 - \omega_{shaft}) \tag{3.6}$$

$$f_2(W_F, \omega_g) = \frac{1}{k_{flmb}}(W_F - k_{flma}) + 3(1 - \omega_g) \tag{3.7}$$

$$f_3(W_F) = k_{EFR1} W_F + k_{EFR2} \tag{3.8}$$

$$H_{ESG}(s) = \frac{\dfrac{W_E(sX_E + 1)}{Z_E}}{1 + s\dfrac{Y_E}{Z_E}} \tag{3.9}$$

3.3.2 Notional Single Shaft Gas Turbine

The notional single shaft gas turbine model is shown in Figure 3.7. Figure 3.8 shows the acceleration control diagram. The regarding equations for notional single shaft gas turbine model are given from (3.10) to (3.15) [63]. The parameters and default values for the notional single shaft gas turbine model are given in Table 3.2.

Table 3.2: Parameters for Notional Single-Shaft Gas Turbine Model [63]

Parameter	Description	Default Value
a	Valve positioner constant	1
b	Valve positioner constant	0.05
c	Valve positioner constant	1
k_{flma}	No-load fuel parameter	0.2
k_{flmb}	No-load fuel parameter $(1 - k_{flma})$	0.8
$k_{\alpha-limit}$	Acceleration limit (pu/s)	0.01
$k_{i-\alpha}$	Acceleration control integral gain	100
$L_{lower-Limit1}$	Lower limit for limit block ”Limit 1” (fuel limit)	-0.1
$L_{upper-Limit1}$	Upper limit for limit block ”Limit 1” (fuel limit)	1.5
T_c	Combustor delay time (s)	0.01
W	Speed governor constant	25
X	Speed governor constant	0
Y	Speed governor constant	0.05
Z	Speed governor constant	1
τ_{FS}	Fuel system time constant (s)	0.4
τ_{CP}	Compressor discharge volume time constant (s)	0.2

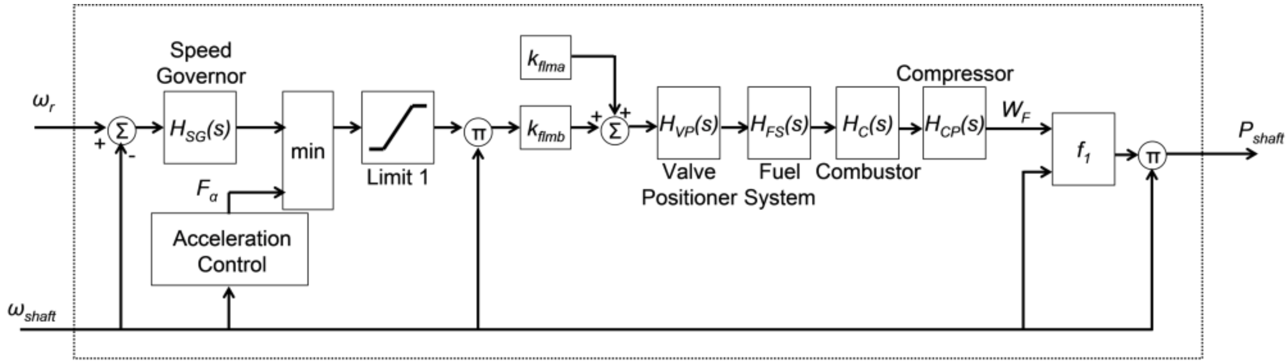

Figure 3.7: Notional single-shaft gas turbine model [63].

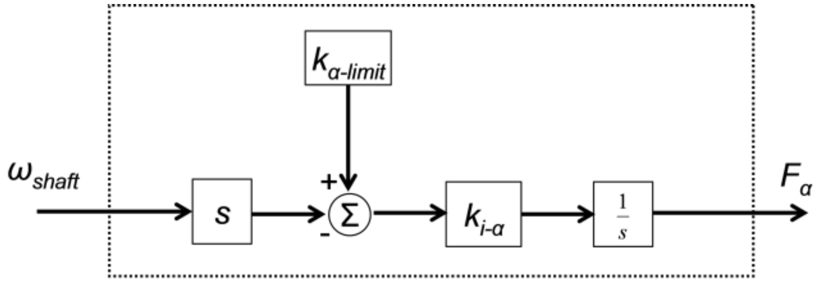

Figure 3.8: Acceleration control for notional single-shaft gas turbine model [63].

$$H_{SG}(s) = \frac{\dfrac{W(sX+1)}{Z}}{1+s\dfrac{Y}{Z}} \tag{3.10}$$

$$H_{VP}(s) = \frac{\dfrac{a}{c}}{1+\dfrac{b}{c}s} \tag{3.11}$$

$$H_{FS}(s) = \frac{1}{1+\tau_{FS}s} \tag{3.12}$$

$$H_C(s) = e^{-sT_c} \tag{3.13}$$

$$H_{CP}(s) = \frac{1}{1+\tau_{CP}s} \tag{3.14}$$

$$f_1(W_F, \omega_{shaft}) = \frac{1}{k_{flmb}}(W_F - k_{flma}) + 0.5(1-\omega_{shaft}) \tag{3.15}$$

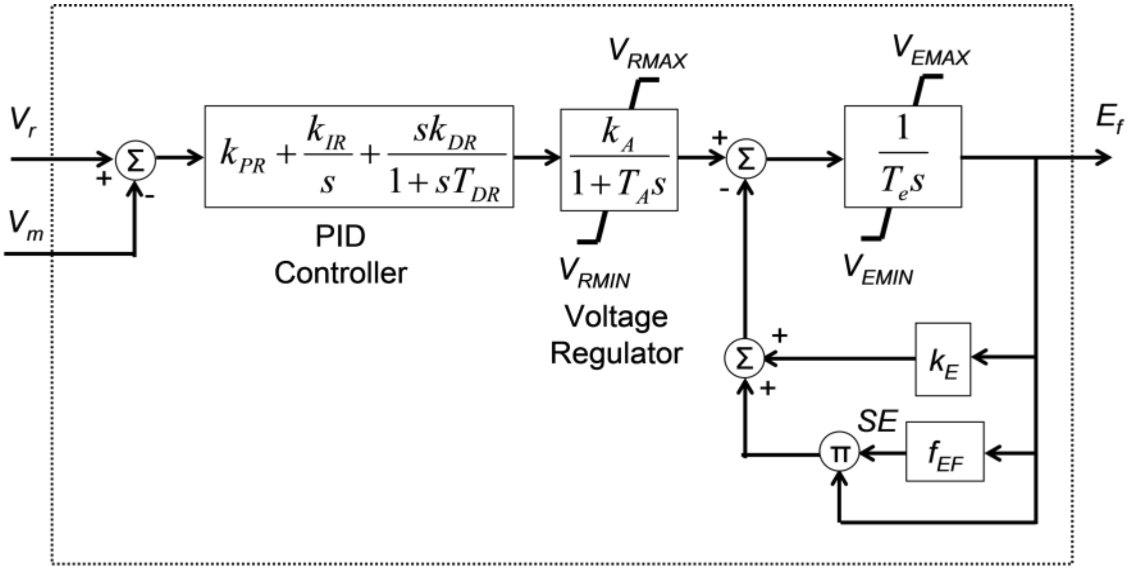

Figure 3.9: Simplified implementation of the IEEE type AC8B exciter model [63].

3.3.3 IEEE Type AC8B Exciter

The circuit diagram of the excitation system is shown in Figure 3.9 and transfer function of excitation voltage, E_f, is given in (3.16). The inputs of the excitation system are, reference voltage, V_r, and actual measured voltage, V_m. The output is field winding excitation voltage, E_f. The parameters and default values of the model are described in Table 3.3.

$$f_{EF}(E_f) = k_{EF1}e^{k_{EF2}E_f} \tag{3.16}$$

3.3.4 Electric Machines

For simulation purpose, synchronous machine model of the SimPowerSystems is used. Figure 3.10 shows the interface diagram of the synchronous machine. The inputs of the synchronous machine are, shaft power, P_{shaft}, from the gas turbine module and the excitation voltage, E_f, from the excitation system. The output of the mode is shaft rotational speed, ω_{shaft}. Three nodes are exposed from the synchronous machine model, A, B, C. They are connected to the MMC converter. The parameters for the notional synchronous machine are given in Table 3.4.

Table 3.3: Parameters for Simplified IEEE Type AC8B Exciter [63]

Parameter	Description	Default Value
k_A	Voltage regulator gain	1
k_{DR}	PID controller derivative gain	0
k_{IR}	PID controller integral gain	0.08
k_{EF1}	Saturation function coefficient	1.0119
k_{EF2}	Saturation function coefficient	0.0875
k_{PR}	PID controller proportional gain	200
T_A	Voltage regulator time constant (s)	0.0001
T_e	Integration time constant (s)	1
T_{DR}	Filter time constant for PID controller derivative branch (s)	0.001
V_{EMAX}	Field winding excitation voltage upper limit	∞
V_{EMIN}	Field winding excitation voltage lower limit	0
V_{RMAX}	Voltage regulator upper limit	5
V_{RMIN}	Voltage regulator lower limit	0

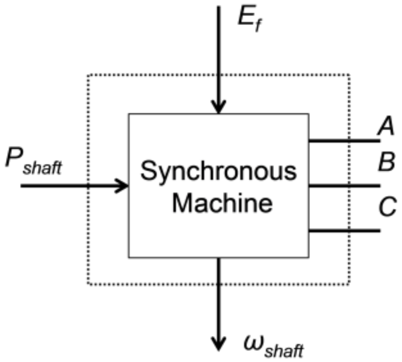

Figure 3.10: Interface for notional round rotor synchronous machine [63].

3.4 MMC Converter

With the aim of implementing a promising solution of DC fault current limiting in the MVDC shipboard system, the MMC converter is the new technology in the case of AC-DC power conversion. The MMC converter is consisted of submodules. The submodules are identical but individually controllable. These submodules are responsible for the large number of discrete voltage levels, whose characteristics make the converter to operate as a controllable voltage source converter [61]. This helps the converter to reduce the total harmonic distortion. Figure 3.11 shows the basic structure of MMC converter. The number of submodules depends on the voltage level. The submodules

Table 3.4: Parameters for Synchronous Machine [63]

Parameter	Description	Default Value
S_r	Rated apparent power (MVA)	47
V_r	Rated voltage (line-line, RMS) (kV)	4.16
f_r	Rated frequency (Hz)	60
R_s	Stator resistance (pu)	2.8544e-3
Xd	d-axis synchronous reactance (pu)	1.305
Xd'	d-axis transient reactance (pu)	0.296
Xd''	d-axis subtransient reactance (pu)	0.252
Xq	q-axis synchronous reactance (pu)	0.474
Xq''	q-axis subtransient reactance (pu)	0.243
Xl	Leakage reactance (pu)	0.18
H	Inertia constant	3.2
F	Friction factor (pu)	0
p	Pole pairs	2

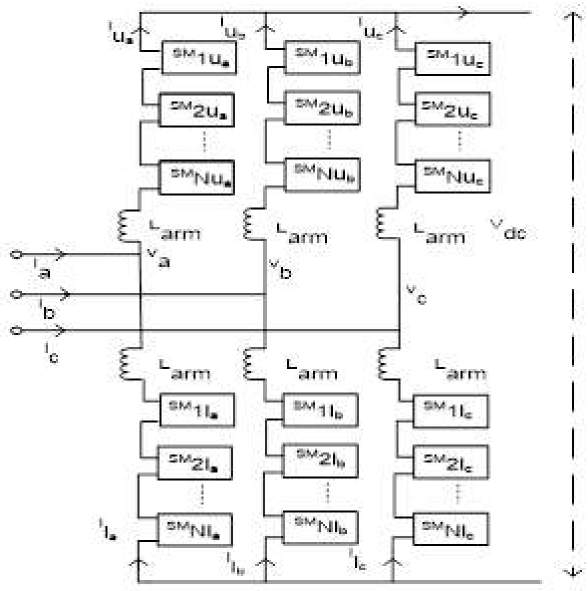

Figure 3.11: MMC structure.

can be half-bridge or full-bridge in configuration. Figure 3.12 shows the full-bridge and half-bridge configuration of submodule. The half-bridge submodules produce $+V$ or zero voltage level and full-bridge submodules produce $\pm V$ or zero voltage. There is also the clamp-double, three level flying capacitor (FC), three level neutral-point-clamped (NPC), five level cross connected submodule configuration for different purposes [62].

(a) Half-bridge.

(b) Full-bridge.

Figure 3.12: Half-bridge and full-bridge configuration of submodule.

From Figure 3.12a, the half-bridge configuration has two valves (S1 and S2) and a capacitor. The valve consists of an IGBT and an antiparallel freewheeling diode. The charging and discharging of the capacitor depends on the direction of the current flow. A valve is on when either the IGBT or the diode is conducting. There are three possible switching states. In state 1, S1 is on and S2 is off, the submodule output voltage is equal to capacitor voltage V_c. In state 2, the S1 is off and S2 is on, the submodule output voltage is equal to zero and this state is called bypassed state. In state 3, neither S1 nor S2 is on. This state is called blocked state. In this state, the capacitor cannot discharge but if the direction of current is positive it can be charged. The half-bridge configuration cannot limit DC fault current.

From Figure 3.12b, the submodule is in full-bridge configuration. As it has a double number of switching devices, the power losses and costs are higher than half-bridge configuration submodule. But this full-bridge configuration of submodule limits DC fault current. The output terminal voltage is positive when the valve S1 and S4 are on and is negative when valve S2 and S3 is on. This negative output voltage is not usually used. It is used for DC fault current limiting. When S1 and S3 or S2 and S4 are on, it represents the bypassed state. Due to avoiding short circuit condition of capacitor, two IGBT in one pair will not be allowed to conduct at the same time.

3.4.1 MMC Converter Operation Principle

As the MMC converter has three-phase circuit configuration and each phase has identical configuration, here circuit equations are derived for a single phase. The same equations are also applicable for the other two phases. Figure 3.13 shows the circuit configuration for a single phase MMC. From Figure 3.13, the voltage difference of the upper arm voltage and phase voltage is given

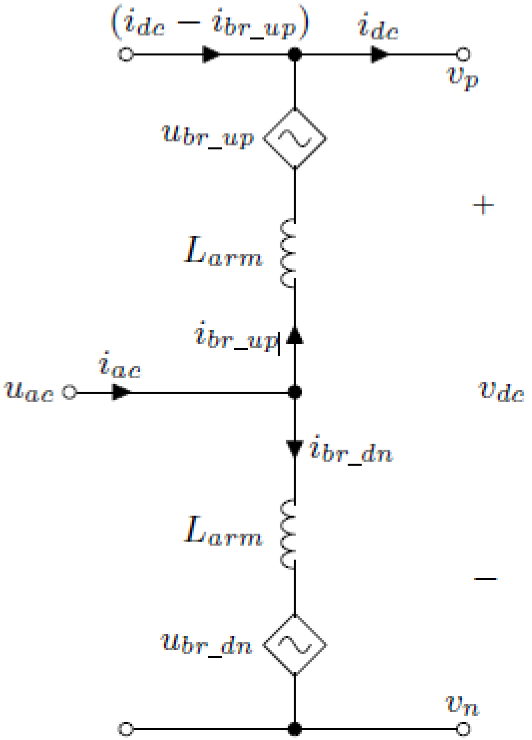

Figure 3.13: Equivalent AC circuit of a single phase of MMC [64].

in (3.17) [64]. The phase voltage is given in (3.18).

$$v_p - v_a = u_{br\_up} + L_{arm}\frac{di_{br\_up}}{dt} \tag{3.17}$$

$$v_a - v_n = u_{br\_dn} + L_{arm}\frac{di_{br\_dn}}{dt} \tag{3.18}$$

If there is no load on the DC side, then the branch currents are half of the phase current given in (3.19), and (3.20).

$$i_{br\_up} = \frac{i_{ac}}{2} \tag{3.19}$$

$$i_{br\_dn} = \frac{i_{ac}}{2} \tag{3.20}$$

If load is connected to the DC side, then the DC side load current, i_{dc}, will be summed of the each phase current. Here, for each phase, DC current and AC current are coupled in the branch currents. So the upper and lower branch currents for the single phase are given in (3.21), and (3.22).

$$i_{br\_up} = \frac{i_{ac}}{2} + \frac{i_{dc}}{3} \tag{3.21}$$

$$i_{br\_dn} = \frac{i_{ac}}{2} - \frac{i_{dc}}{3} \tag{3.22}$$

After adding (3.17) and (3.18),

$$v_p - v_n = u_{br\_up} + u_{br\_dn} + L_{arm}\frac{di_{br\_up}}{dt} + L_{arm}\frac{di_{br\_dn}}{dt} \tag{3.23}$$

After substitution of (3.21), and (3.22) into (3.23),

$$v_{dc} = u_{br\_up} + u_{br\_dn} + L_{arm}\frac{di_{br\_up}}{dt} + 2L_{arm}\frac{\frac{di_{dc}}{3}}{dt} \tag{3.24}$$

Replacing (3.21) into (3.17) gives

$$u_{br\_up} = v_i + \frac{v_{dc}}{2} \tag{3.25}$$

$$u_{br\_dn} = -v_i + \frac{v_{dc}}{2} \tag{3.26}$$

3.4.2 MMC Average Value Model (AVM)

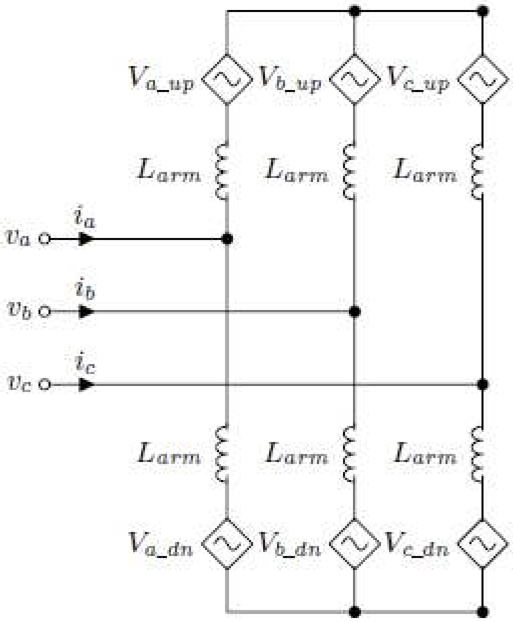

Figure 3.14: MMC AVM AC side representation [64].

3.4.2.1 AC side representation. The main working principle of AC side is power exchange between the generator and the MMC converter. Actually, this part controls how much power will

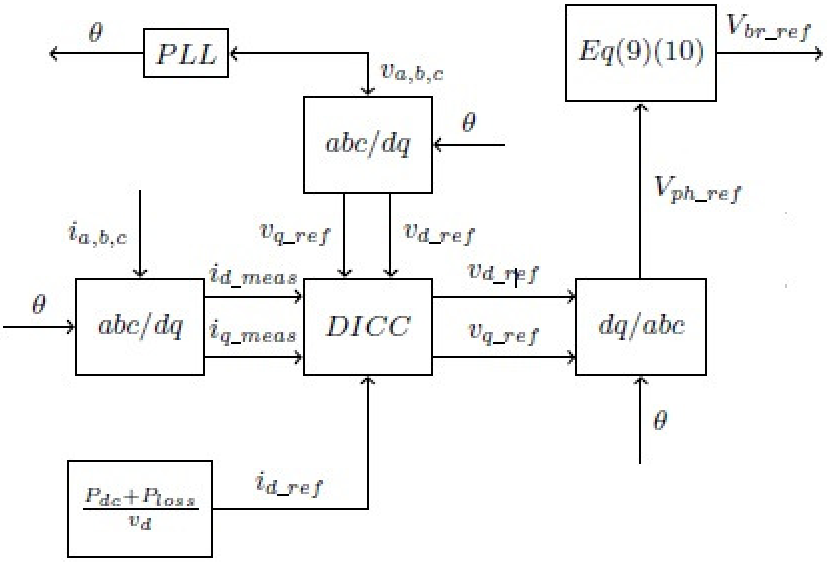

Figure 3.15: MMC AC side control architecture [64].

be transferred from the generator to the MMC converter. Figure 3.14 shows the diagram of the AC side of the MMC converter and Figure 3.15 shows the AC side control diagram. Decoupled inner current control (DICC) is used to generate the phase voltage. In this control, the reference d-axis current, i_{d_ref}, is compared with the measured current, i_{d_meas}. The output of the DICC is the phase reference d-axis voltage, v_{d_ref} , and q-axis voltages, v_{q_ref}. After dq/abc transformation, the phase voltage, V_{ph_ref} is applied in (3.25) and (3.26) to get the branch voltage in each branch.

3.4.2.2 DC side representation. Figure 3.16 shows the diagram of the DC side representation of the MMC converter. Here the basic principle is to balance the average power between the AC side and DC side of the MMC converter. The power of the AC side and DC side are not equal due to losses for switching and circulating current. The power relation of DC and AC side is given in (3.27). The equivalent inductance of each phase, L_{dc_eq}, can be found from (3.28), where L_{br} is the branch inductance. Similar computation technique is used to calculate the DC side equivalent resistance, R_{dc_eq}, in (3.29). Figure (3.17) shows the control diagram of the DC side of MMC converter. The outer DC voltage control and inner DC current control is used for controlling the DC output voltage. The final output is V_{d_ref}, which is sent to the controlled voltage source as the

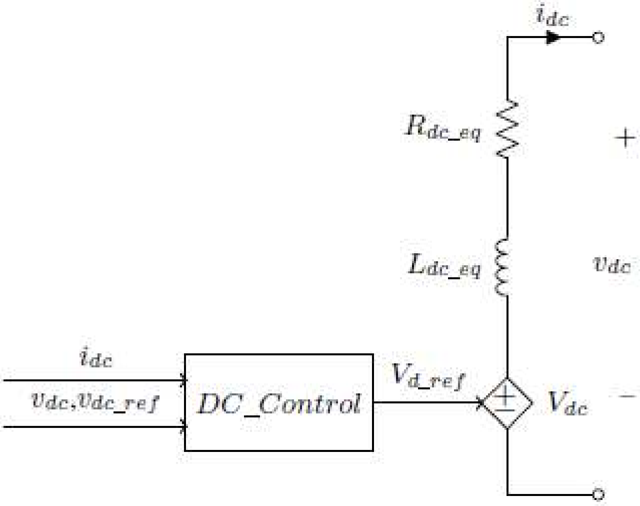

Figure 3.16: MMC DC side representation [64].

.

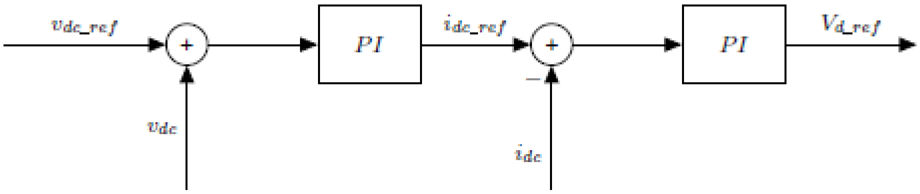

Figure 3.17: MMC DC side control [64]

.

output voltage of the MMC converter. The DC output voltage of the MMC converter is actually the MVDC voltage of the shipboard power system.

$$P_{ac} = P_{dc} + P_{loss} \tag{3.27}$$

$$L_{dc\_eq} = \frac{2L_{br}}{3} \tag{3.28}$$

$$R_{dc\_eq} = \frac{2R_{br}}{3} \tag{3.29}$$

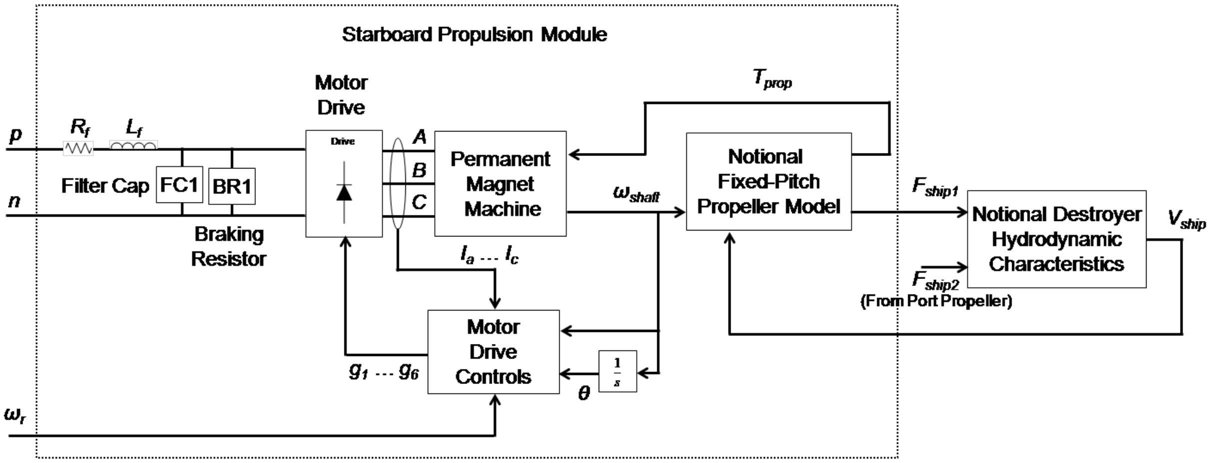

Figure 3.18: Propulsion system module and hydrodynamics module for baseline MVDC system [63].

.

3.5 Propulsion Systems

The propulsion system model is shown in Figure 3.18. The propulsion system is consisted of five major components. The notional permanent magnet synchronous machine is connected to the motor drive inverter. It produces the shaft speed, ω_{shaft}. It takes the counter torque, T_{prop} as the input which is produced by the notional fixed-pitch propeller model. The propeller model takes the shaft speed, ω_{shaft} as the input. It produces the torque, T_{prop} and thrust, F_{ship1}, as the output. The propeller thrusts, F_{ship1} and F_{ship2} produced by the notional fixed propeller models of the starboard and port propulsion systems are passed to the notional destroyer hydrodynamics model. The notional destroyer hydrodynamics model eventually produces the final ship speed, V_{ship}, in knots. The motor drive controller uses hysteresis current control technique to control the motor drive inverter. The inputs of motor drive controller are, reference propeller speed, ω_r, actual propeller speed, ω_{shaft}, the rotor angle, θ, the input currents of the propulsion motor (I_a, I_b, I_c). The gating pulses (g1 to g6) are passed to the motor drive inverter. For motor drive inverter, two levels IGBT bridge is used. BR represents shunt breaking resistor to dissipate the power generated from the drive during breaking the propellers. FC represents filter capacitor with charging resistor. The propulsion system is connected to the MVDC system. The description of the propulsion system components are given here.

3.5.1 Notional Permanent Magnet Machine

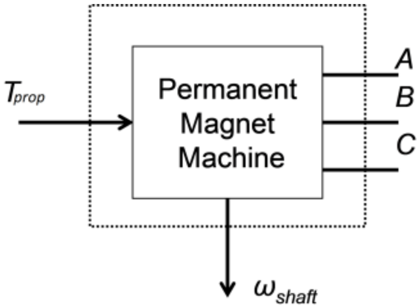

Figure 3.19: Interface for notional permanent magnet machine [63].

.

Figure 3.19 shows the input and output interface of the notional permanent magnet machine model. The permanent magnet machine model of Simulink, SimPowerSystems is used as the notional permanent magnet motor. It takes the propeller counter torque, T_{prop} as the input. It produces the propeller rotational speed, ω_{shaft}, as the output. This model shows three electrical nodes (A, B, C) which are connected to the motor drive inverter. The parameters for the notional permanent magnet machine are given in Table 3.5.

Table 3.5: Parameters for Notional Permanent Magnet Machine [63]

Parameter	Description	Default Value
R_s	Stator resistance (Ω)	0.005
L_d	D-axis stator inductance (H)	0.8e-3
L_q	Q-axis stator inductance (H)	0.8e-3
λ	Flux linkage established by magnets ($V \cdot s$)	16.58
J	Moment of inertia ($kg \cdot m^2$)	1.6e3
F	Friction ($N \cdot m \cdot s$)	0.0005
p	Pole pairs	12

3.5.2 Motor Drive Inverter

Figure 3.20 shows the basic circuit configuration of the motor drive inverter. It has five electrical nodes (A, B, C, p, n). For inverter model, universal bridge model of Simulink, SimPowerSystems is used. The bridge model has three bridge arms and uses IGBT/Diode as the power electronic device.

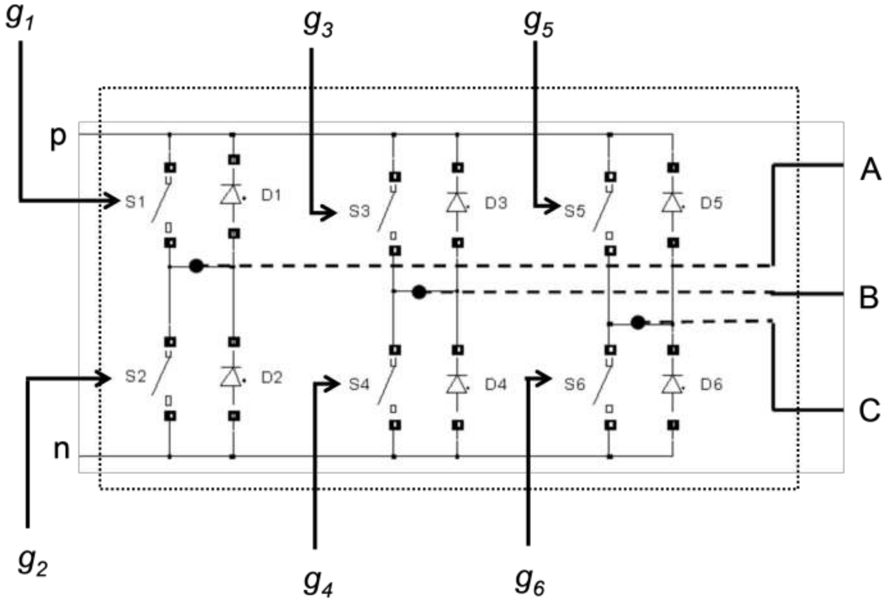

Figure 3.20: Two-level IGBT bridge [63].

.

3.5.3 Motor Drive Controller

Hysteresis based current control technique of the motor drive inverter is shown in Figure 3.21. The inputs of the motor drive controller are, reference rotational speed, ω_r, measured shaft speed, ω_{shaft}, rotor angle, θ, measured three phase currents (I_a, I_b, I_c). The outputs of the controller are gating pulse signals (g1 to g6) for the inverter. Here, f_{hys} implements hysteresis based comparison function for the measured currents (I_a, I_b, I_c), and the reference currents $(I_{a-r}, I_{b-r}, I_{c-r})$. For example, the generation of the gating signals g1 and g2 is described here. If the gating signal, g1, is on (value = 1), then the signal will be on unless measured current, I_a, becomes larger than an upper threshold current, $(I_{a-r} + \Delta I)$. If measured current, I_a, reaches to the upper threshold current $(I_{a-r} + \Delta I)$, then g1 will be turned off (value = 0). Then the gating signal (g1) will be in the off-state (value = 0) until measured current, I_a, becomes smaller than the lower threshold

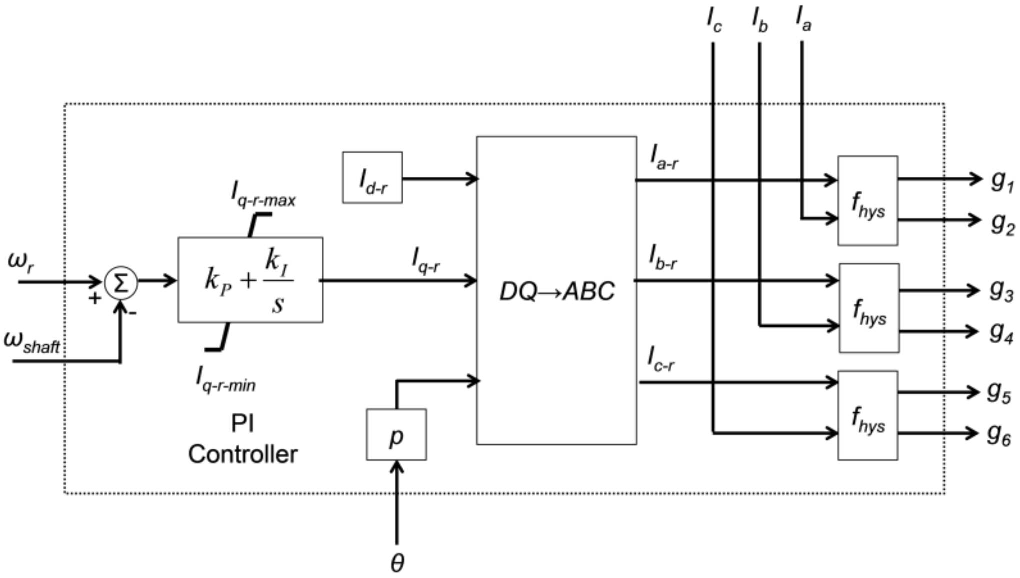

Figure 3.21: Hysteresis current control for two-level drive for permanent magnet synchronous machine [63].

.

current $(I_{a-r} - \Delta I)$. If measured current, I_a, reaches to the lower threshold current $(I_{a-r} - \Delta I)$, then the gating signal (g1) will be turned on. In the whole process, g2 is the complement of the g1. By the same process, gating signals (g3 to g6) are generated by the currents $(I_b, I_c, I_{b-r}, I_{c-r})$. The parameters for the motor drive controller are given in Table 3.6.

Table 3.6: Parameters for Motor Drive Controller [63]

Parameter	Description	Default Value
I_{d-r}	Requested d-axis current (A)	0
$I_{q-r-max}$	PI controller upper limit (A)	∞
$I_{q-r-min}$	PI controller lower limit (A)	$-\infty$
k_i	PI controller integral gain	10
k_p	PI controller proportional gain	7500
p	The number of pole pairs of the machine	12
ΔI	Hysteresis comparator dead-band width parameter	0

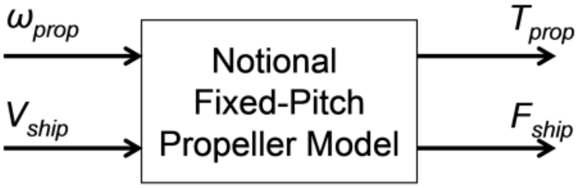

Figure 3.22: Interface for notional fixed-pitch propeller model [63].

.

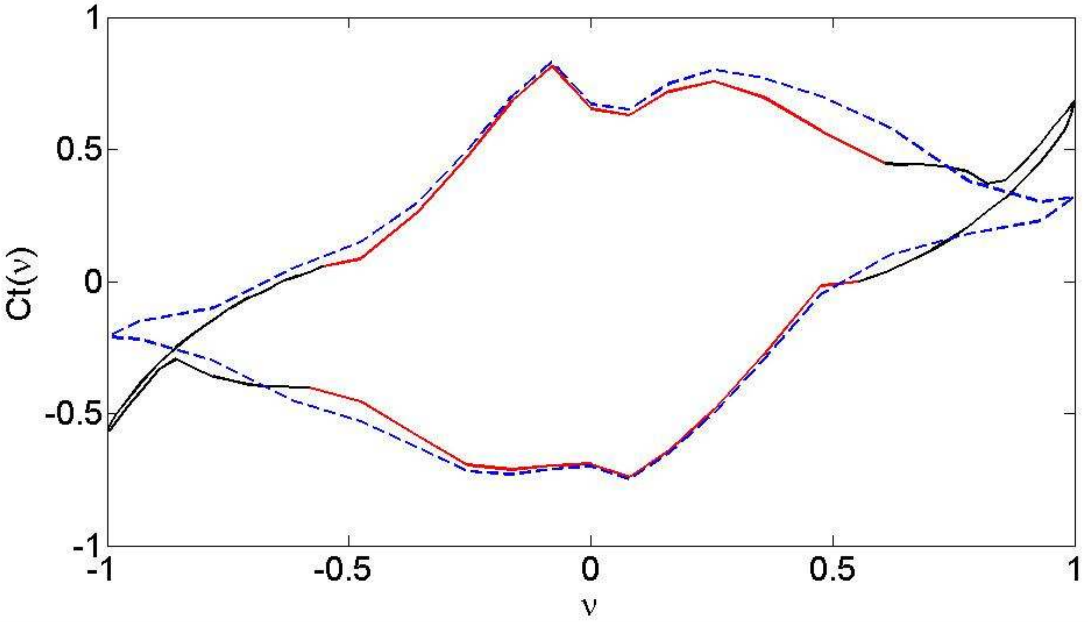

Figure 3.23: Thrust coefficient curves for notional fixed-pitch propeller model [63].

3.5.4 Notional Fixed-Pitch Propeller

Figure 3.22 shows the simple interface diagram of the notional fixed-pitch propeller. It produces the counter torque, T_{prop}, and thrust, F_{ship}. It takes the output shaft speed of the permanent magnet motor, ω_{shaft}, and the ship speed, V_{ship}, as the inputs. The mathematical model of the propeller is described in [65] given in (3.30)- (3.34). Parameters for the model are given in the Table 3.7. Figure 3.23 and Figure 3.24 show the thrust coefficient curves and torque coefficient curves for the propeller mode. But, information provided by [66], do not cover the entire range of the advance ratio, ν. To cope up with this situation, information provided by [67] are used (dotted curves of

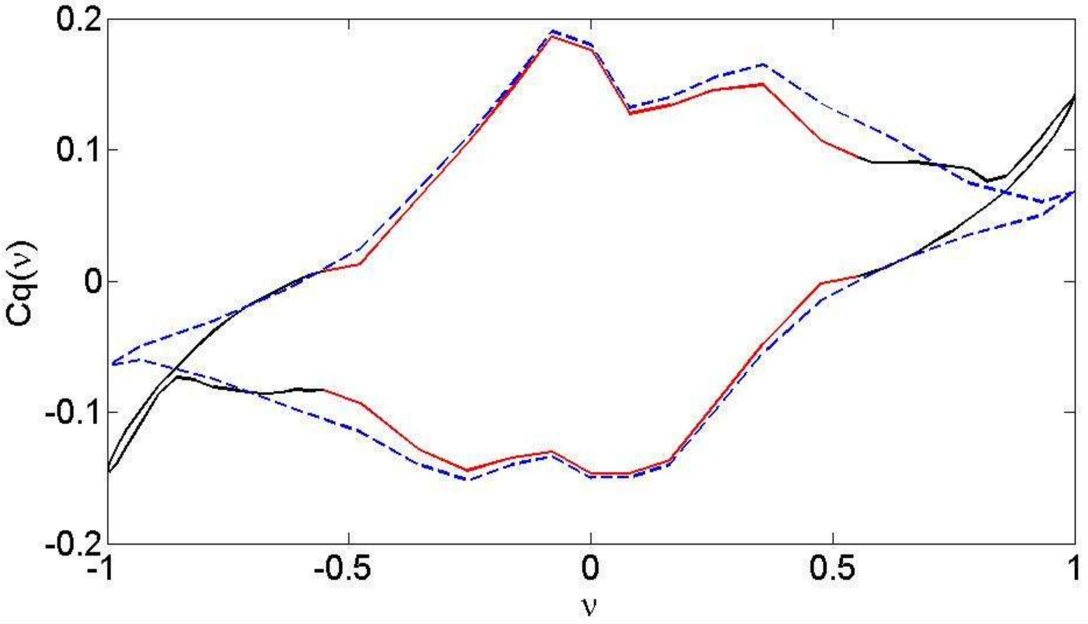

Figure 3.24: Torque coefficient curves for notional fixed-pitch propeller model [63].

.

Figure 3.23 and Figure 3.24). A curve fitting technique is used to match the data provided by [66] and [67], and eventually generate the solid curves (red and black) of Figure 3.23 and Figure 3.24. Figure 3.25 shows the Taylor Wake Factor vs ship speed (knots). The moment of inertia for the port propeller and starboard propeller are given in Table 3.8.

$$T_{prop} = C_Q(\nu)\rho(\frac{D^3}{\eta_r})(V_a^2 + (nD)^2) \tag{3.30}$$

$$F_{ship} = C_\tau(\nu)\rho D^2(V_a^2 + (nD)^2)(1 - t) \tag{3.31}$$

$$n = \frac{\omega_{prop}}{2\pi} \tag{3.32}$$

$$\nu = \frac{nD}{\sqrt{V_a^2 + (nD)^2}} \tag{3.33}$$

$$V_a = V_{ship}(1 - w_T) \tag{3.34}$$

3.5.5 Ship Hydrodynamic Characteristics

Figure 3.26 shows the ship hydrodynamics model. The ship hydrodynamics model is from [66]. But, [66] provides information about hydrodynamic characteristics when ship speed is equal or above

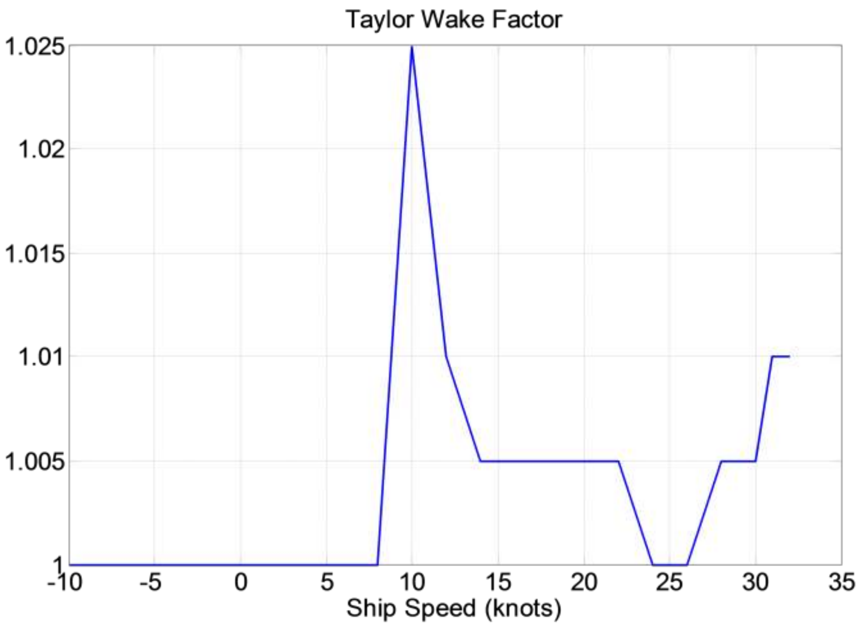

Figure 3.25: Taylor Wake Fraction curve for notional fixed-pitch propeller model [56, 63].

.

Table 3.7: Parameters for Notional Fixed-Pitch Propeller Model [66, 67]

Parameter	Description	Default Value
ρ	Density of salt water	1027 kgm^{-3}
D	Propeller diameter	7.01m
η_r	Relative rotative efficiency	1.0
$C_Q(\nu)$	Open water propeller torque coefficient	Figure 3.24
$C_\tau(\nu)$	Open water propeller thrust coefficient	Figure 3.23
$1 - w_T$	Taylor wake fraction	Figure 3.25
$1 - t$	Thrust deduction factor	0.96, $V_{ship} \geq 0$; 0.97, $V_{ship} < 0$

Table 3.8: Additional Parameters Associated with Notional Fixed-Pitch Propeller Model [66]

Parameter	Description	Default Value
J_1	Moment of inertia of the starboard propeller	2.0573e5 $kg \cdot m^2$
J_2	Moment of inertia of the port propeller	2.2767e5 $kg \cdot m^2$

10knots. Hydrodynamic characteristics for ship speed lower than 10knots are provided in [68]. The hydrodynamics model takes the thrusts (F_{ship1}, F_{ship2}) from the port and starboard propellers as inputs. It finally produces ship speed, V_{ship}, in knots as the output. The hydrodynamics model takes

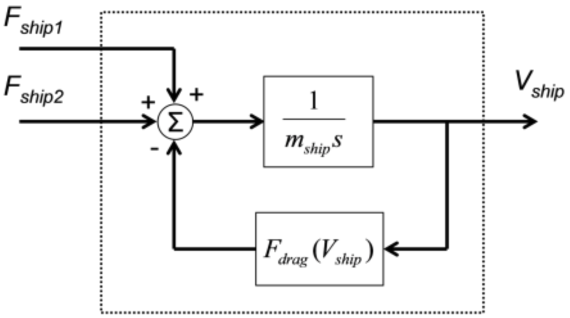

Figure 3.26: Notional destroyer hydrodynamic characteristics [63].

.

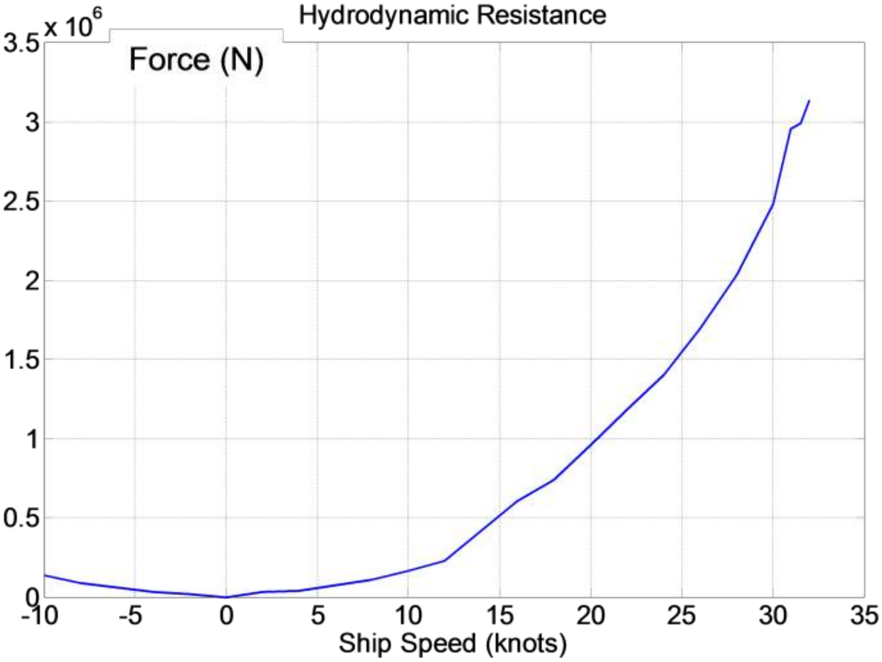

Figure 3.27: Hydrodynamic resistance for notional destroyer model [63].

into account the mass of the ship, m_{ship}, and the ship hydrodynamics resistance, F_{drag}, as a function of the ship speed in knots. Parameters for the ship mass, m_{ship}, ship hydrodynamics resistance, F_{drag}, are given in the Table 3.9. Figure 3.27 shows the variation of the ship hydrodynamics resistance with the variation of the ship speed in knots. Data for ship hydro dynamics resistance, F_{drag}, for ship speed at 10 knots or above are given in [66]. But for ship speed less than 10 knots are given in [68].

Table 3.9: Parameters for Notional Destroyer Hydrodynamic Characteristics Model [66, 68, 69]

Parameter	Description	Default Value
m_{ship}	Mass of the ship	14.29e6 kg
$F_{drag}(V_{ship})$	Hydrodynamic resistance	Figure 3.27

3.6 Bi-directional DC-DC Converter

A DC-DC converter with the bi-directional capability is required to exchange energy between energy storage devices and the MVDC system. For efficient power transfer, the bi-directional DC-DC converter should be light weight, compact in size and highly reliable. Depending on the isolation property, bi-directional DC-DC converters can be categorized into non-isolated bi-directional DC-DC converter and isolated bi-directional DC-DC converter.

Basic DC-DC converter with unidirectional capability can be turned into non-isolated DC-DC converter with bi-directional capability by replacing the diode with a controllable switch in the circuit configuration [70]. Some of the lacking of non-isolated bi-directional converters is there is no galvanic isolation between two sides, the structure of the converter becomes impractical with the increase of voltage ratio, and operation of buck or boost mode is in one direction only. To overcome the lacking of non-isolated bi-directional DC-DC converter, bi-directional DC-DC converter with galvanic isolation is used. Figure 3.28 shows the dual active bridge bi-directional DC-DC converter with high frequency transformer to maintain galvanic isolation between two sources. It is also used to maintain voltage matching between two sides of the sources. Some of the advantages of dual active bridge DC-DC converter are: for soft switching purpose there is no need for additional active or passive elements for soft switching purposes, all the switches on both sides experience equal current stresses, and the design and manufacture of this DC-DC converter becomes simpler for the high frequency transformer.

3.6.1 Average Model of the DAB Converter

To show the steady state and transient behavior of the DAB converter, the average model equations of the DAB converter are derived based on one switching period (T_s) [71]. For buck mode operation of the DAB converter, the average model equations are,

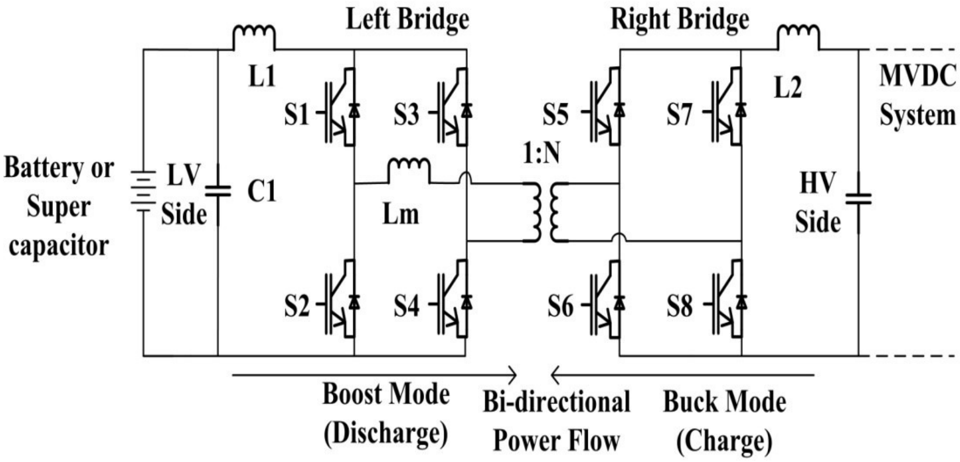

Figure 3.28: Topology of the bi-directional DC-DC converter.

.

$$L\frac{d < i_L >}{dt} = \frac{1}{N} < V_{HV} > .d- < v_{LV} > \tag{3.35}$$

Current following through the capacitor C_1 is

$$C_1\frac{d < v_{LV} >}{dt} =< i_L > -\frac{< v_{LV} >}{R_1} \tag{3.36}$$

$$< i_{HV} >=< i_p > .d \tag{3.37}$$

Where the symbol $<>$ represents the average value over the switching period T_s and d, denotes the duty cycle. R_1 represents the equivalent load resistance at the low voltage side, i_p is the transformer primary current. For the boost mode operation of the DAB converter, the average model equations are,

$$L\frac{d < i_L >}{dt} =< v_{LV} > -\frac{1}{N} < V_{HV} > .(1-d) \tag{3.38}$$

$$C_2\frac{d < v_{HV} >}{dt} = \frac{1}{N} < i_L > .(1-d) - \frac{< v_{HV} >}{R_2} \tag{3.39}$$

To get the steady state model of the DAB converter, DC terms are taken after Taylor series expansion of (3.35) to (3.39). It leads to (3.40) - (3.42) for the buck mode operation of the DAB converter

$$V_{LV} = \frac{D}{N}V_{HV} \tag{3.40}$$

$$I_L = \frac{1}{R_1} V_{LV} \tag{3.41}$$

$$I_p = \frac{1}{N} I_L \tag{3.42}$$

Where D represents the duty cycle. Similarly, for the boost mode

$$V_{HV} = \frac{N}{D'} V_{LV} \tag{3.43}$$

$$I_L = \frac{N}{R_2 D'} V_{HV} \tag{3.44}$$

Where $D' = 1 - D$

3.6.2 DAB Converter Controller

The controller of the interleaved DAB converter for the battery is shown in Figure 3.29 [72]. For the supercapacitor, the same control technique is used for controlling the DAB converter. In the control technique of the DAB converter, the battery reference power ($P_{Bat-ref}$) is divided by the measured bus voltage (V_{Bus}) and it provides the reference current (I^*_{Bat}) for the batteries. Then the battery reference current (I^*_{Bat}) is divided by the total number of batteries. The difference between the individual battery reference current and measured current is passed to a PI controller. Here $G_1(s)$ represents the transfer function of the PI controller for a single battery system. For simulation purpose, the average model of DAB converter is used.

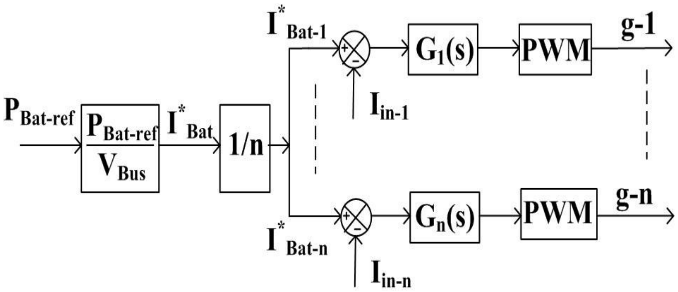

Figure 3.29: Controller of DC-DC converter for battery.

.

3.7 Battery

Battery can be modeled in different ways depending on the system requirement and accuracy. Battery modeling study is done from a very simple battery model to a complex battery model.

3.7.1 Simple Battery Model

Figure 3.30 shows the simple battery model [73]. In this model, E_0 represents the electromotive force of the battery and R_s represents the constant equivalent resistor as an internal series resistance, V_0 represents terminal voltage [74].

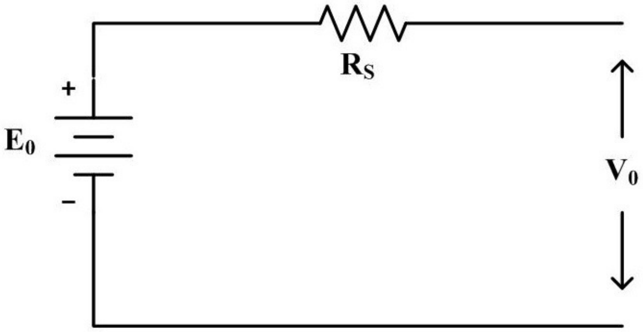

Figure 3.30: Equivalent circuit of simple battery model.

3.7.2 Modified Battery Model

In this model with the simple battery model, the internal resistance is changed to vary with the state of charge [75]. Figure 3.31 shows the equivalent circuit of the modified simple battery model [73]. Here the resistance, R_s, varies with the battery state of charge. The internal resistance is given in (3.45). Here, R_0, is the fixed internal resistance, k is the capacity coefficient, and S is the state of charge which varies from 0 to 1.

$$R_s = \frac{R_0}{N} S_k \tag{3.45}$$

Advanced Battery Model: Keeping similarity with the modified simple battery model, advanced battery model is presented in [76]. Figure 3.32 shows the equivalent circuit of the advanced

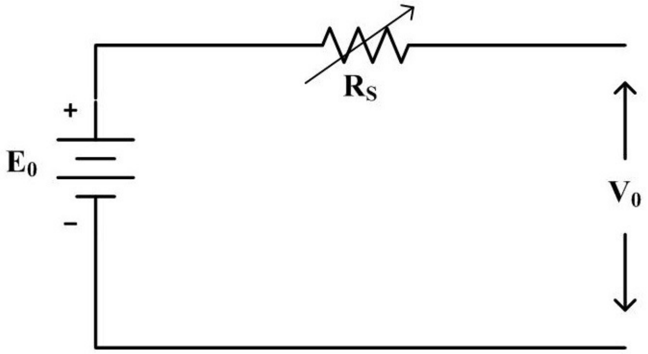

Figure 3.31: Equivalent circuit of modified battery model.

.

battery model [73]. In this model, the internal series resistance varies with the depth of discharge. The variation is either linear or nonlinear. The output terminal voltage, V_0, is given in (3.46). Where, E_0 is the open circuit voltage, I_{batt} is the battery current and R_i is the internal resistance which varies with the depth of discharge (Q). Where Q is given in (3.47).

$$V_0 = E_0 - I_{batt} \times R_i \tag{3.46}$$

$$\begin{aligned} Q &= \frac{q}{q_{max}} \\ q &= I_{batt} \times t \end{aligned} \tag{3.47}$$

Thevenin Battery Model: Thevenin model is the one of the most commonly used battery

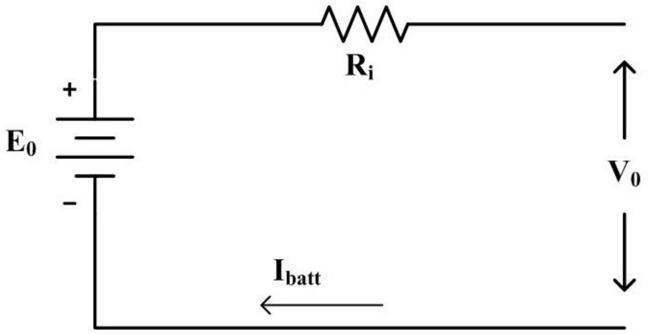

Figure 3.32: Equivalent circuit of advanced battery.

.

models. Figure 3.33 shows the equivalent circuit of the Thevenin battery model [73]. In this model,

E_0, is no load battery voltage, R_i, is internal resistance, R_0 represents the battery overvoltage resistance due to the contact resistance of plate to electrolyte and C_0, is capacitance between electrolyte and electrodes [77]. For Thevenin battery model, the battery terminal voltage, V_0, is given in (3.48), voltage drop, V_{drop}, across R_0 and C_0 is given in (3.49).

$$V_0 = E_0 - (I_{batt} \times R_i + V_{drop}) \tag{3.48}$$

$$V_{drop} = (\frac{1}{R_0} + \frac{1}{C_0}) \times I_{batt} \tag{3.49}$$

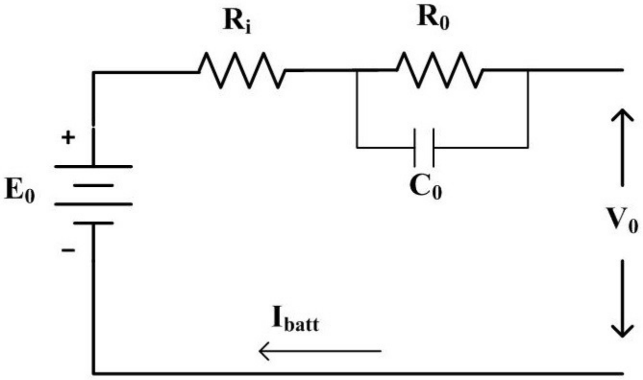

Figure 3.33: Equivalent circuit of Thevenin model.

.

MathWorks Battery Model: Figure 3.34 shows the equivalent circuit diagram of MathWorks battery model [78]. MathWorks battery model implements a generic battery model [78]. This model is applicable for most popular types of rechargeable battery models like the Lead-Acid battery model, Lithium-ion battery model, Nickle-Cadmium battery model, and Nickle-Metal-Hydride battery model. This battery model is similar to the Shepherd battery model [79] but the exception with the Shepherd model is that it can represent voltage dynamics with the change of current. It takes into account the open circuit voltage as a function of SOC [80]. The battery voltages for Lithium-ion battery model during charging and discharging are given in (3.50) and (3.51). Here, E_0, represents constant battery voltage, K, polarization resistance or polarization constant, Q, battery capacity, it, actual battery charge, A, exponential zone voltage amplitude,

B, exponential zone time constant inverse, R_i, internal resistance, i, battery current, i^*, filtered battery current [80].

$$E_{batt-discharge} = E_0 - R_i.i - K\frac{Q}{Q-it}.(it + i^*) + Ae^{-B.it} \quad (3.50)$$

$$E_{batt-charge} = E_0 - R_i.i - K\frac{Q}{it-0.1.Q}.i^* - K\frac{Q}{Q-it}.it + Ae^{-B.it} \quad (3.51)$$

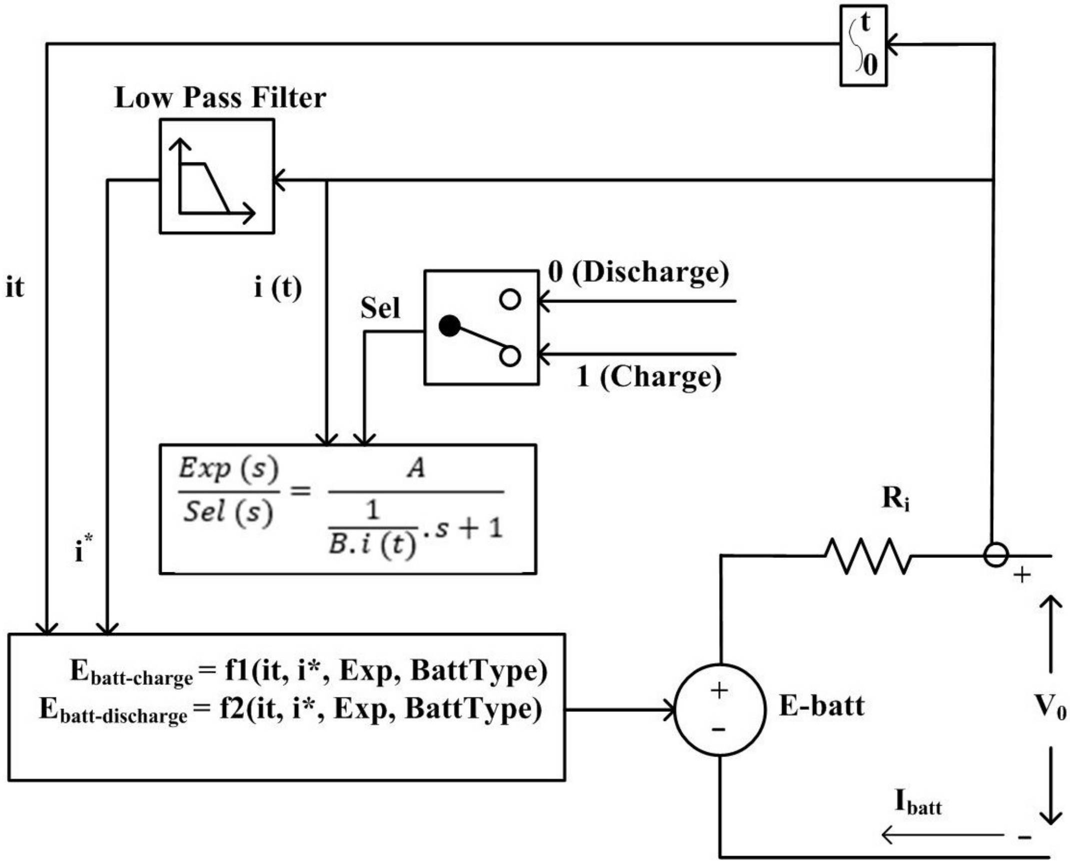

Figure 3.34: Equivalent circuit of the MathWorks battery model.

.

3.8 Supercapacitor

Figure 3.35 shows the typical construction of a supercapacitor. It has two electrodes which is separated by a permeable membrane. The electrolyte of supercapacitor connects both electrodes electrically. The separator prevents physical contact of the electrodes but allows ion transfer between them. From Figure 3.35, the components of supercapacitor are

1. Power source
2. Collector
3. Polarized electrode
4. Helmholtz double layer
5. Electrolyte having positive and negative ions
6. Separator

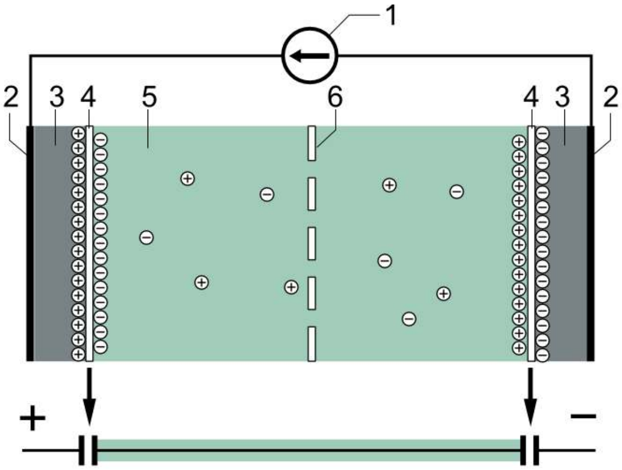

Figure 3.35: Construction of supercapacitor [81].

.

3.8.1 Supercapacitor Equivalent Circuit

Figure 3.36 shows the effective classical RC model of supercapacitor [82]. From Figure 3.36, R_s represents equivalent series resistance which is very small, R_p, is equivalent parallel resistance which is very high, C, is an ideal capacitor. Equivalent series resistance, R_s, represents heat losses and

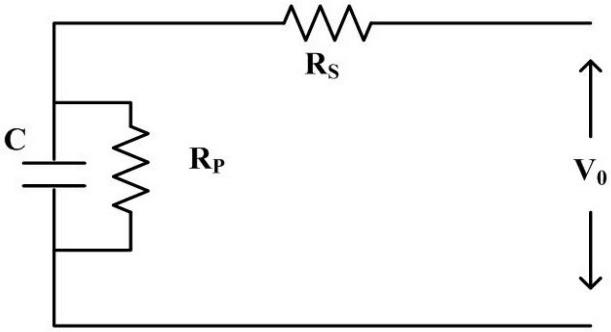

Figure 3.36: RC equivalent model of supercapacitor.

.

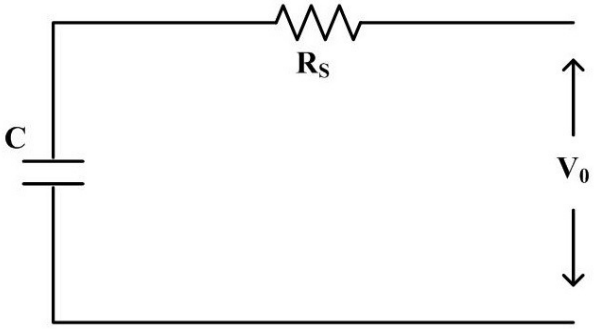

Figure 3.37: RC equivalent model of supercapacitor after neglecting self-discharge.

.

charge-discharge voltage transient mutation in the process of charging and discharging. Equivalent parallel resistance, R_p, represents self-discharge leakage loss. If self-discharge is neglected and DC operation of supercapacitor is considered, then r_p can be eliminated and the circuit becomes simpler which is shown in Figure 3.37 [83].

3.8.2 MathWorks Supercapacitor Model

MathWorks implemented a generic model of supercapacitor to represent most popular types of supercapacitors. Figure 3.38 shows the equivalent circuit of supercapacitor designed by MathWorks [84]. The supercapacitor output voltage is expressed in (3.52). Where the no load voltage, V_T, is given in (3.53).

$$V_0 = V_T - R_i.i_{sc} \tag{3.52}$$

$$V_T = \frac{N_S Q_T d}{N_p N_e \varepsilon \varepsilon_0 A_i} + \frac{2N_w N_s RT}{F} sinh^{-1}\left(\frac{Q_T}{N_p N_e^2 A_i \sqrt{8RT\varepsilon\varepsilon_0 c}}\right) \tag{3.53}$$

The meaning of the symbols are given here

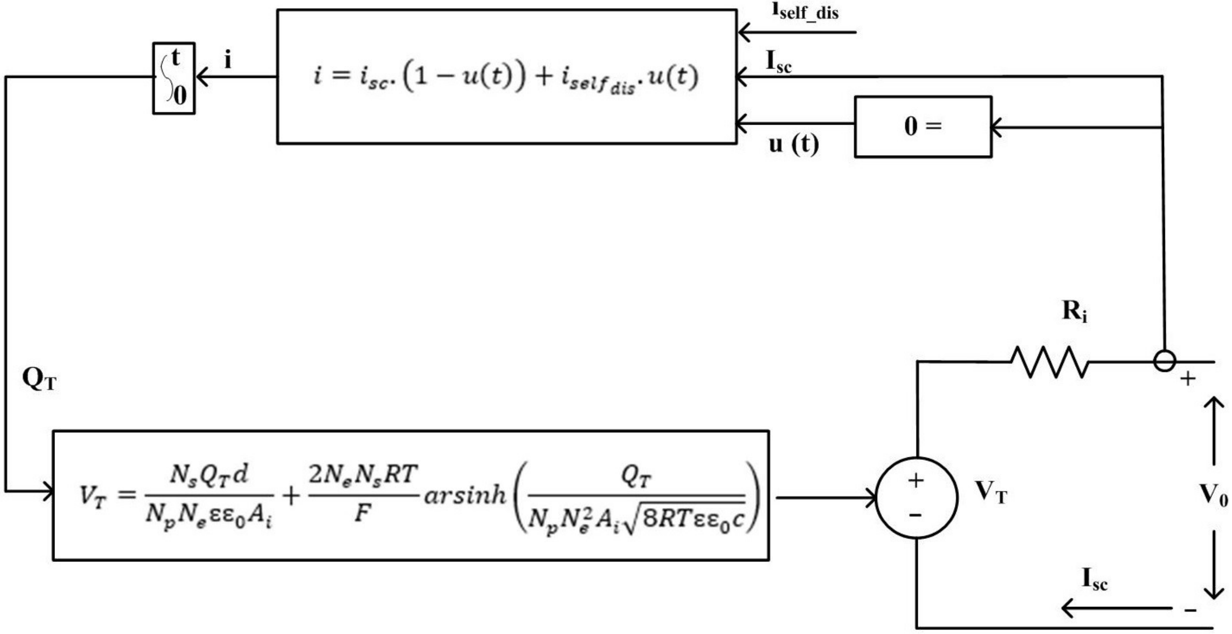

Figure 3.38: The equivalent circuit of the supercapacitor model of MathWorks.

.

- A_i, Interfacial area between electrodes and electrolyte (m^2)
- c, Molar concentration (mol/m^3)
- F, Faraday constant
- i_{SC}, Supercapacitor current (A)
- V_{SC}, Supercapacitor voltage (V)
- C_T, Total capacitance (F)
- R_{SC}, Total resistance (ohms)
- N_e, Number of layers of electrodes

- N_A, Avogadro constant
- N_p, Number of parallel supercapacitors
- N_s, Number of series supercapacitors
- Q_T, Electric charge (C)
- R, Ideal gas constant
- d, Molecular radius
- T, Operating temperature (K)
- ε, Permittivity of material
- ε_0, Permittivity of free space

3.9 Pulsed Load

Here pulsed load is represented as a constant power load. Figure 3.39 shows the model for the pulsed load. The look-up table is used to generate the required pulse train. It generates a power signal for a very short specified time. The power signal is divided by the measured voltage, and the final output signal is passed to the constant current source as the reference current signal for the pulsed load. The positive edge of the trigger signal is used to activate the pulsed load. With the activation of pulsed load, minimum voltage is restricted to 4000V.

3.10 Cables

Shipboard power system is much smaller compared to a grid power system. For this reason, the cables for different zones and connectors are small with low inductance and shunt capacitance. But the existence for the small inductance and shunt capacitance in the cable present very small time-constants. To show the effect of the small time constants, it is required to run the model in small time-step sized. But as the intention is to show the steady state power analysis, the cables are represented only by series resistances. The parameters for the cable models are summarized in Table 3.10.

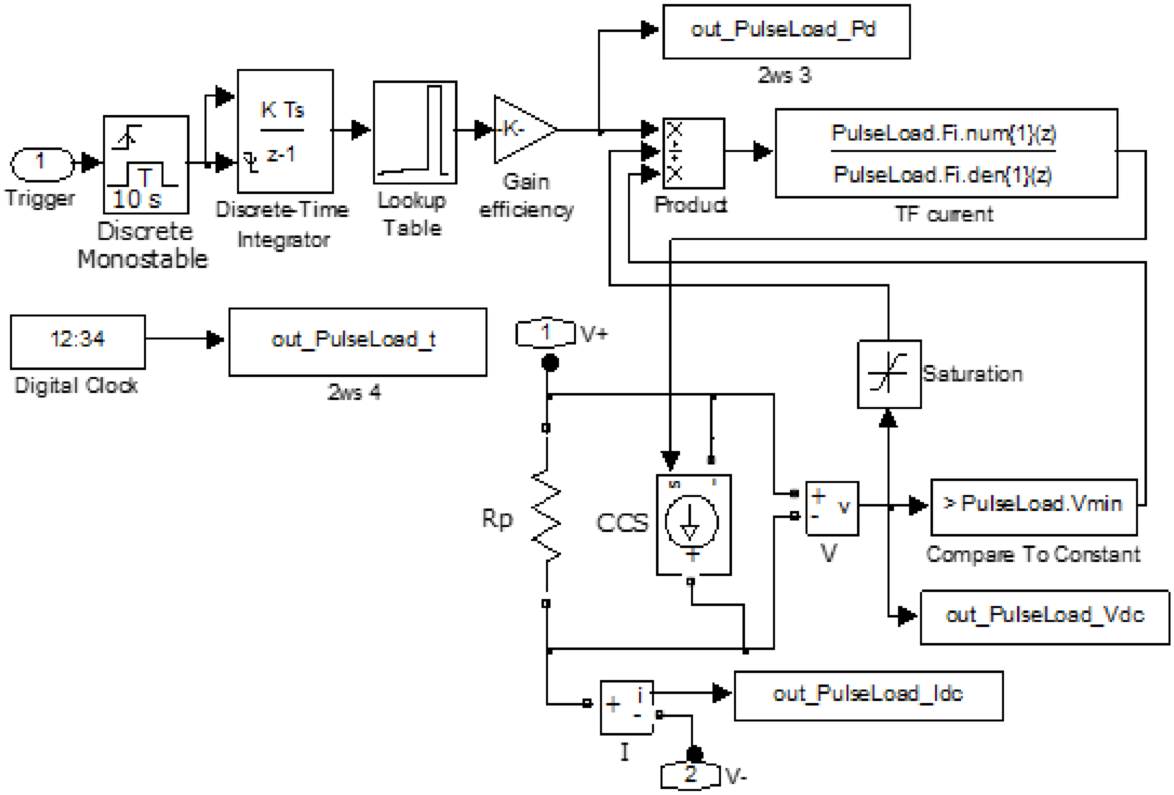

Figure 3.39: Pulsed load model [63].

.

Table 3.10: Cable Parameters for MVDC System [63]

Switchboard 1	Switchboard 2	Resistance	Inductance
Zone 1 Port	Zone 2 Port	1.69e-4 Ω	0H
Zone 1 Port	Zone 1 Starboard	2.35e-4 Ω	0H
Zone 1 Starboard	Zone 2 Starboard	1.95e-4 Ω	0H
Zone 2 Port	Zone 3 Port	1.84e-4 Ω	0H
Zone 2 Starboard	Zone 3 Starboard	1.82e-4 Ω	0H
Zone 3 Port	Zone 4 Port	2.14e-4 Ω	0H
Zone 3 Starboard	Zone 4 Starboard	1.66e-4 Ω	0H
Zone 4 Port	Zone 4 Starboard	2.99e-4 Ω	0H

CHAPTER 4

DESIGN OF ENERGY STORAGE MANAGEMENT SYSTEMS

In this section, the design of two energy storage system (ESM) systems will be discussed. One is based on the FL controller and the another is based on PI controller.

To demonstrate the operations of the proposed ESM systems, the notional MVDC power system of IEEE standard 1709 [27] is simplified. The modified MVDC system architecture is given in Figure 4.1, which has one Main AC Turbine Generator (MTG) and one Auxiliary AC Turbine Generator (ATG) as the source of power. The modular multilevel converters (MMC) with AC-DC power conversion topology are used to connect the generators with the MVDC system. The total load of the MVDC system are divided into propulsion load, ship service load and radar load. It has also pulsed load as electric weaponry system. To maintain the power demand and the MVDC bus voltage, it integrates HESS. The HESS is connected to the MVDC system via DAB bi-directional DC-DC converters. The whole system is modeled and simulated in Matlab/simulink environment.

4.1 Fuzzy Logic (FL) Controller Based ESM Strategy

Figure 4.2 shows the block diagram of the FL controller based ESM strategy. In this control strategy, two level FL based control technique is used. The level I (FL1) is designed to provide the total storage reference power ($P_{stor-ref}$) for charging and discharging of HESS. A generation limit checking controller is added to check whether the total demand including the charging and discharging reference power crosses the total generation limit. The level II (FL2) is designed to separate the ($P_{stor-ref}$) between battery reference power ($P_{Bat-ref}$) and supercapacitor reference power (P_{SC-ref}) for charging or discharging. When $P_{stor-ref}$ is less than zero, the storage system will play a role of power supply to meet the increased power demand of the MVDC system. When the load is suddenly unloaded, $P_{stor-ref}$ becomes greater than zero, the storage system will absorb the surplus energy from the MVDC system.

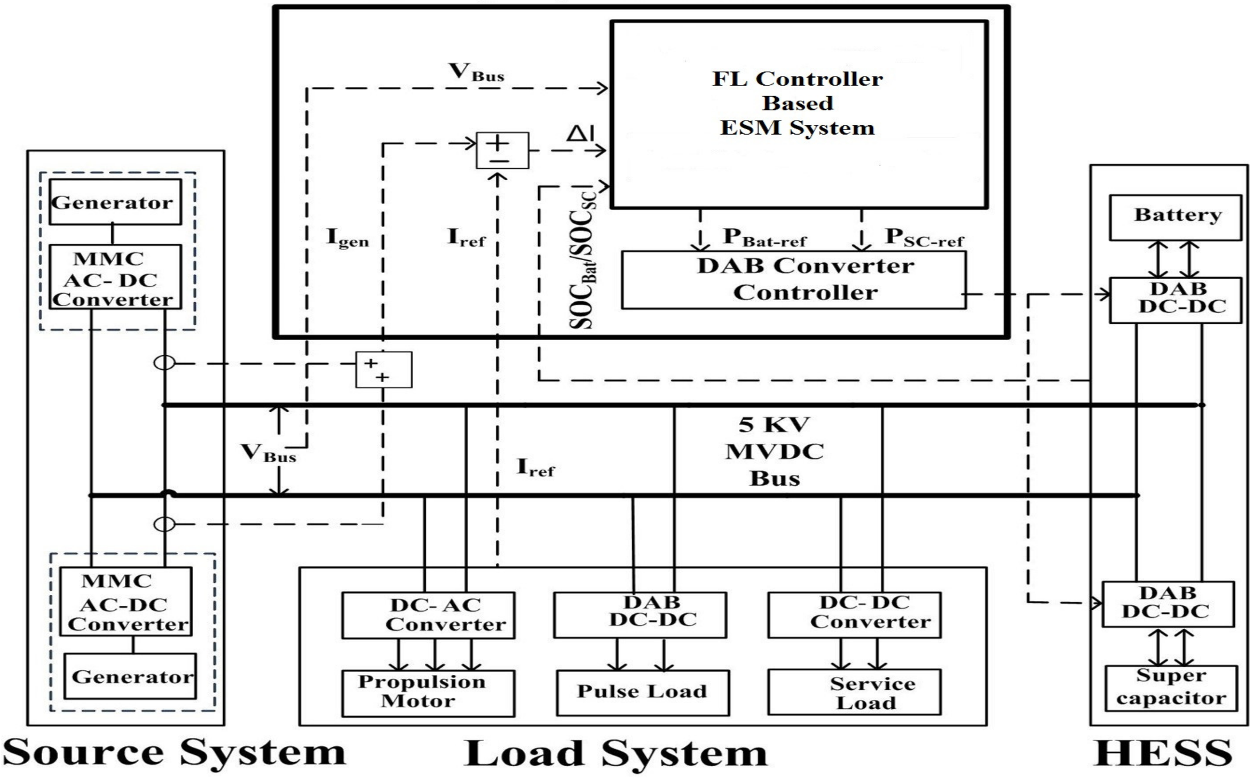

Figure 4.1: MVDC system with FL controller based ESM system.

4.1.1 Total Storage Reference Power ($P_{stor-ref}$) Estimation

The aim of the FL controller is to determine the total storage reference power ($P_{stor-ref}$) to balance the demand and supply of power. The input variables of the fuzzy logic supervisor are the difference (ΔI) between the total generated current (I_{gen}) and the total reference current (I_{ref}), the MVDC bus voltage (V_{Bus}) and the SOC of the battery and supercapacitor (SOC_{Bat}, SOC_{SC}) [21, 85]. Here, total generated current (I_{gen}) is the sum of output DC currents of the two MMC converters, which are supplied by the two gas turbine based generators, and the total reference current (I_{ref}) is calculated based on the power demand from individual load. The load power demand is divided by the ideal MVDC voltage (5kV) to get the individual reference current. Then the sum of individual reference currents provides the total reference current (I_{ref}). The total storage reference power ($P_{stor-ref}$) for the battery and supercapacitor is estimated from these input variables. A fuzzy logic control strategy has three parts: *fuzzification*, *inference*, and *defuzzification*.

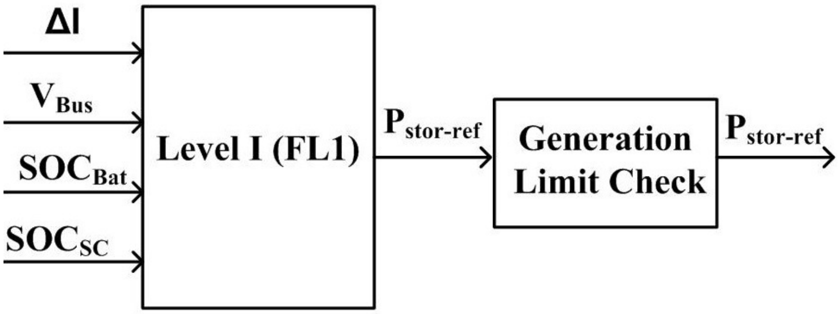

(a) Level I control.

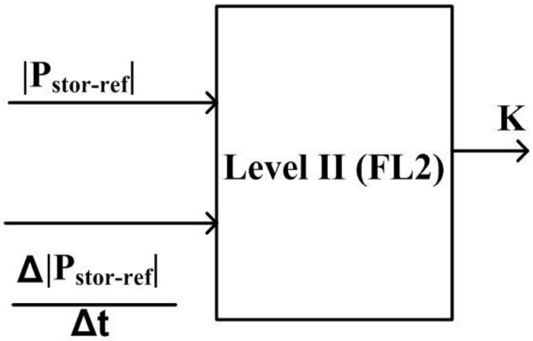

(b) Level II control.

Figure 4.2: FL based two level ESM strategy.

4.1.1.1 Fuzzyfication. The membership functions of four input variables (ΔI, V_{Bus}, SOC_{Bat}, SOC_{SC}) of the FL controller are shown in Figure 4.3. The ΔI and V_{Bus} decide the demanded reference power and the SOC of the battery (SOC_{Bat}) and supercapacitor (SOC_{SC}) adjust the demanded reference power for the HESS. Three membership functions (Negative, Zero, Positive) are chosen for the input variable, ΔI. The associated limits for ΔI are -1600A as lower limit and 1600A as upper limit. The limits are chosen based on the power, energy rating of the battery, supercapacitor, and the maximum power mismatch of generation and load demand of the MVDC system. For Negative and Positive membership functions, trapezoidal shape and for Zero membership function, triangular shape are chosen. Negative and Positive membership functions represent the discharging and charging conditions, respectively. Zero membership function represents the balanced condition, i.e. the total load demand is equal or lower than the total generation capacity

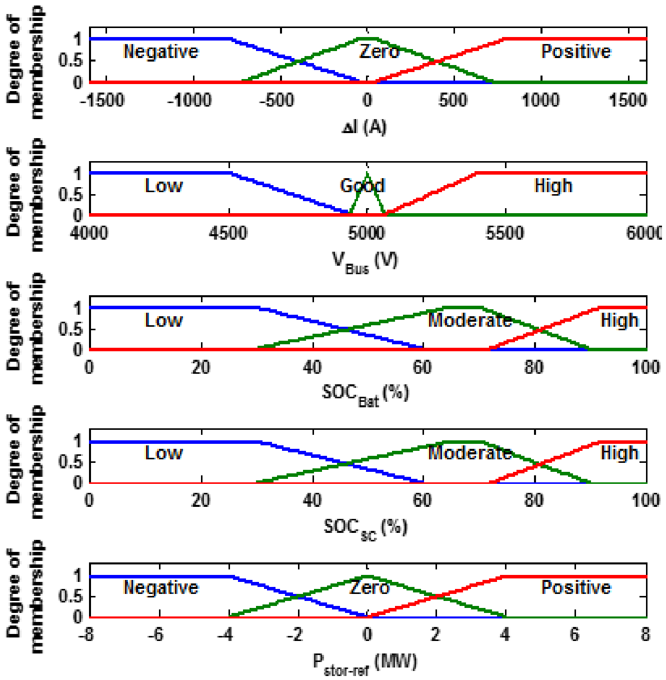

Figure 4.3: Membership functions of input and output variables for FL1 controller.

(40MW) and energy storages (battery and supercapaictor) are not required to operate ($\Delta I = 0$). For another input variable, V_{Bus}, three membership functions (Low, Good, High) are chosen. The associated limits for V_{Bus} are 4000V as lower limit and 6000V as upper limit, respectively. To represent under voltage and over voltage situation, 4000V is chosen as the lower limit and 6000V is chosen as upper limit. Low and High membership functions represent under voltage and over voltage condition, respectively, and trapezoidal shape are chosen for them. For Good membership function, triangular shape is chosen and represents balanced condition. For other input variables (SOC_{Bat}, SOC_{SC}), trapezoidal shaped three membership functions (Low, Moderate, High) are chosen. The associated limits of SOC of the battery and supercapacitor are chosen as 0% to 100% (0% SOC means fully discharged and 100% means fully charged). Low and High membership functions help the battery and supercapacitor to escape the deep discharging and overcharging condition. Moderate membership function represents the normal operating range of the battery and supercapacitor. For the output variable, $P_{stor-ref}$, three membership functions (Negative, Zero, Positive) are chosen. Negative and Positive membership functions represent discharging and charging reference power and trapezoidal shape are chosen for them. For Zero membership function, triangular shape is chosen and it represents the balanced condition.

4.1.1.2 Inference. As there are four input variables and each variable has 3 membership functions, a total of 81 fuzzy rules are required and a 2-D table is not sufficient to explain all the fuzzy rules. The fuzzy rules of the FL controller are shown in Table 4.1 with meanings of L = Low, M = Moderate, H = High; Z = Zero, P = Positive, N = Negative, G = Good. The first fuzzy rule is expressed as follows: IF V_{Bus} is L (Low), ΔI is N (Negative), SOC_{Bat} is L (Low) and SOC_{SC} is L (Low), THEN $P_{stor-ref}$ is Z (Zero). It means the FL controller will provide no reference power for discharging although the V_{Bus} is low and ΔI is negative as the SOC of the battery and supercapacitor are low. It shows that the FL controller saves the HESS from deep discharging. Another fuzzy rule can be expressed as follows: IF V_{Bus} is G (Good), ΔI is P (Positive), SOC_{Bat} is H (High) and SOC_{SC} is H (High), THEN $P_{stor-ref}$ is Z (Zero). Here, the FL controller will provide no reference power for charging although the V_{Bus} is good and ΔI is positive as the SOC of the battery and supercapacitor are high. It shows that the FL controller saves the HESS from overcharging/excessive charging. When the HESS are not required to be charged while the load is rejected, the generators will reduce their power supply automatically by controlling their gas turbine based governor systems and will supply only required load. But, if a situation happens that there is extra available energy on the shipboard power system due to transients operation and there is no need to charge the HESS (battery and supercapacitor), then the dissipation system will consume the extra available energy until the generators reduce their output.

4.1.1.3 Defuzzyfication. The membership function of the output variable, $P_{stor-ref}$ is also shown in Figure 4.3. Figure 4.4 shows the surface plot for the FL controller which shows the evolution of $P_{stor-ref}$ versus ΔI and V_{Bus} when SOC_{Bat} and SOC_{SC} are set to 75% and 82.65%, respectively.

4.1.2 Reference Power Separation by FL2 Controller

The objective of the level II (FL2) controller is to allocate the total reference power ($P_{stor-ref}$) between the battery and supercapacitor to control the DAB converter for the charging or discharging of HESS. The diagram of FL2 controller is shown in Figure 4.2b. Inputs of FL2 controller are absolute value of total storage reference power ($|P_{stor-ref}|$), rate of change of $|P_{stor-ref}|$ ($\Delta|P_{stor-ref}|/\Delta t$), and output is partition coefficient (K). FL2 controller is used to determine a

Table 4.1: Fuzzy Rules: $P_{stor-ref}$

	$\mathbf{P_{stor-ref}}$		ΔI		
			N	Z	P
When SOC_{Bat}=L AND SOC_{SC}=L	V_{Bus}	L	**Z**	**Z**	**P**
		G	**Z**	**Z**	**P**
		H	**Z**	**Z**	**P**
	$\mathbf{P_{stor-ref}}$		ΔI		
			N	Z	P
When SOC_{Bat} =L AND SOC_{SC}=M/H, SOC_{Bat}=M/H AND SOC_{SC}=L, SOC_{Bat}=M AND SOC_{SC}=M	V_{Bus}	L	**N**	**N**	**P**
		G	**N**	**Z**	**P**
		H	**N**	**Z**	**P**
	$\mathbf{P_{stor-ref}}$		ΔI		
			N	Z	P
When SOC_{Bat}=H AND SOC_{SC}=M, SOC_{Bat}=M AND SOC_{SC}=H	V_{Bus}	L	**N**	**N**	**Z**
		G	**N**	**Z**	**P**
		H	**N**	**Z**	**P**
	$\mathbf{P_{stor-ref}}$		ΔI		
			N	Z	P
When SOC_{Bat}=H AND SOC_{SC}=H	V_{Bus}	L	**N**	**N**	**Z**
		G	**N**	**Z**	**Z**
		H	**N**	**Z**	**Z**

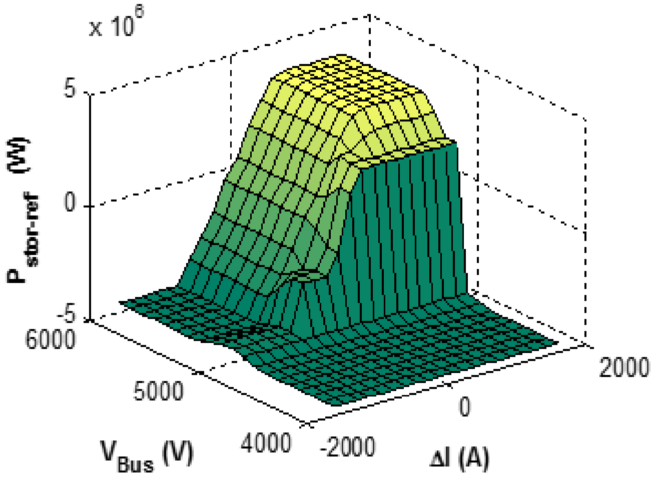

Figure 4.4: Generated surface of FL controller for $P_{stor-ref}$ versus ΔI, V_{Bus} when SOC_{Bat}, SOC_{SC} are set to 75% and 82.65%, respectively.

partition coefficient (K) which divides $P_{stor-ref}$ into $P_{Bat-ref}$ and P_{SC-ref} as expressed in (4.1) and (4.2). As the battery response is slower than the supercapacitor response in the case of meeting sudden load demand, the FL2 controller is designed to allocate the sharp change in total storage reference power ($P_{stor-ref}$) to the supercapacitor as the P_{SC-ref} and steady change of $P_{stor-ref}$ to the battery ($P_{Bat-ref}$). The design procedure of FL2 is as follows.

$$P_{SC-ref} = P_{stor-ref} \times K \tag{4.1}$$

$$P_{Bat-ref} = P_{stor-ref} \times (1 - K) \tag{4.2}$$

4.1.2.1 Fuzzyfication. The membership functions of the two input variables ($|P_{stor-ref}|$, $\Delta|P_{stor-ref}|/\Delta t$) of FL2 controller are shown in Figure 4.5. The input variables are used to determine the power sharing coefficient, K. Three membership functions (Small, Medium, and Big) are chosen for the input variable, $|P_{stor-ref}|$. For Small and Big membership functions, trapezoidal shape and for Medium membership function, triangular shape are chosen. For another input variable, $\Delta|P_{stor-ref}|/\Delta t$, three membership functions (Small, Medium, and Big) are chosen. For Small and Big membership functions, trapezoidal shape and for Medium membership function, triangular shape are chosen. For the output variable, K, three membership functions (Small, Medium, and Big) are chosen. For Small and Big membership functions, trapezoidal shape and for Medium membership function, triangular shape are chosen.

4.1.2.2 Inference. According to the objectives mentioned earlier, the fuzzy rules for FL2 are listed in Table 4.2. As there are 2 inputs, one output and each has 3 membership functions, so a total of 9 rules are designed. The fuzzy rules are designed like that for example, IF $|P_{stor-ref}|$ is Small and $\Delta|P_{stor-ref}|/\Delta t$ is Small then partition coefficient (K) is Small.

Table 4.2: Fuzzy Rules: The Partition Coefficient, K

K		$\Delta\|P_{stor-ref}\|/\Delta t$		
		S	M	B
$\|P_{stor-ref}\|$	S	**S**	**M**	**B**
	M	**S**	**B**	**B**
	B	**S**	**B**	**B**

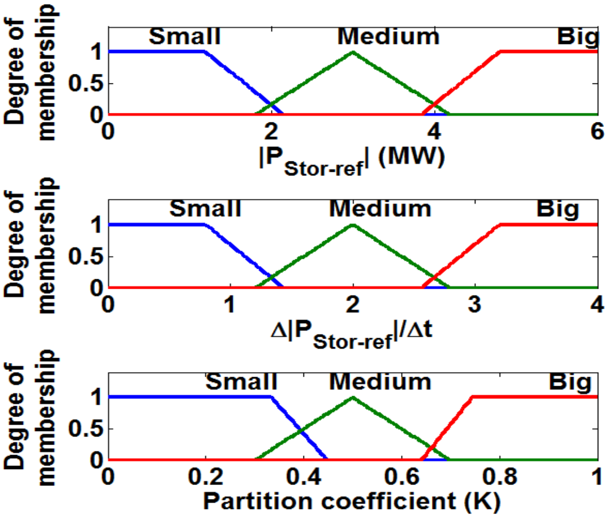

Figure 4.5: Membership functions of input and output variables for FL2 controller.

4.1.2.3 Defuzzyfication. The membership function of the output variable, K, is shown in Figure 4.5. Figure 4.6 shows the surface plot for the FL2 controller which shows the evolution of K versus $|P_{stor-ref}|$ and $\Delta|P_{stor-ref}|/\Delta t$.

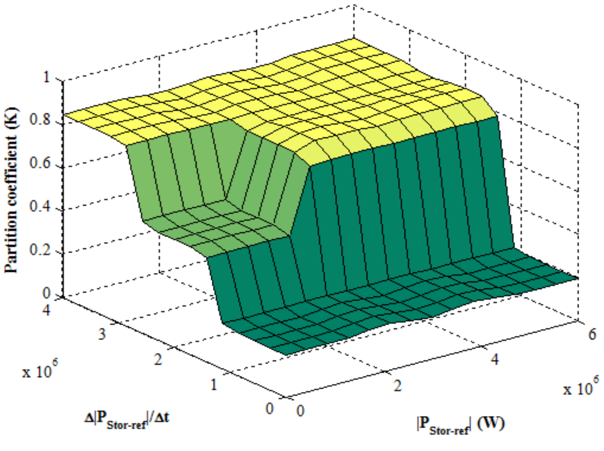

Figure 4.6: Generated surface of FL2 controller for K versus $|P_{stor-ref}|$ and $\Delta|P_{stor-ref}|/\Delta t$.

4.1.3 Reference Power Separation Using Low Pass Filter (LPF)

Power separation between the battery and supercapacitor by the FL2 controller provides very sharp changing reference power for the battery. But the battery is a low power density device and it is difficult for the battery to supply transient power demand. Considering those issues, instead of using FL2 controller for power separation, low pass filter (LPF) is used. Figure 4.7 shows the FL controller and LPF based ESM system. The objective of using a LPF is to divide the total storage reference power ($P_{stor-ref}$) into the steady state and transient power components. The steady state power component is allocated as the reference power for the battery ($P_{Bat-ref}$) and transient power component is allocated as the reference power for the supercapacitor (P_{SC-ref}). In this design, the output of the LPF is used as the storage reference power for the battery ($P_{Bat-ref}$) and the difference between the total storage reference power ($P_{stor-ref}$) and the battery reference power ($P_{Bat-ref}$) is allocated as the reference power for the supercapacitor (P_{SC-ref}). The transfer function of the LPF is given in (4.3), where f_{cf} , is the cutoff frequency of the LPF [86]. As the goal of using low pass filter is to allocate steady power reference to the battery, a cutoff frequency of 1Hz is chosen.

$$G_f = \frac{2\pi f_{cf}}{s + 2\pi f_{cf}} \tag{4.3}$$

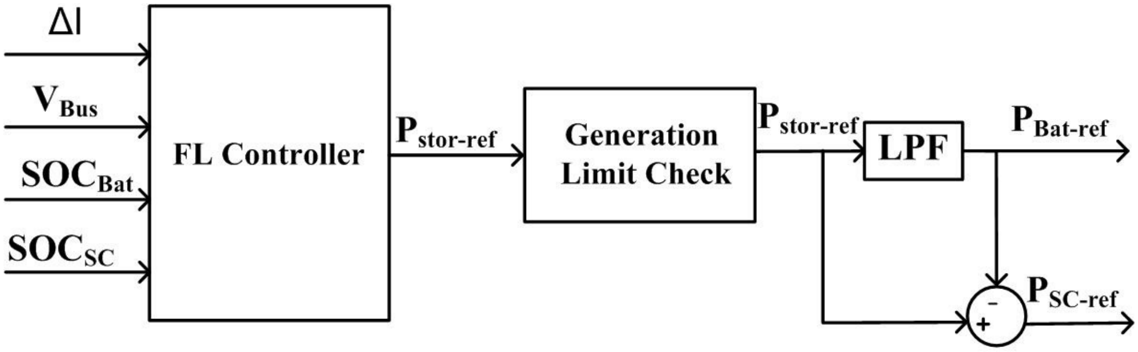

Figure 4.7: FL controller and LPF based ESM system.

4.2 PI Controller Based ESM Strategy

A PI based control strategy has also been designed for comparison purposes. In this control strategy, PI controllers are used to find out the total storage reference power ($P_{stor-ref}$) for the battery and supercapacitor [87,88] and a similar LPF is used to separate the low frequency component and high frequency component of the reference signal ($P_{stor-ref}$). Figure 4.8 shows the block diagram of the PI controller and LPF based ESM system for the MVDC power system of AES. The design of the PI controller based ESM system has three steps.

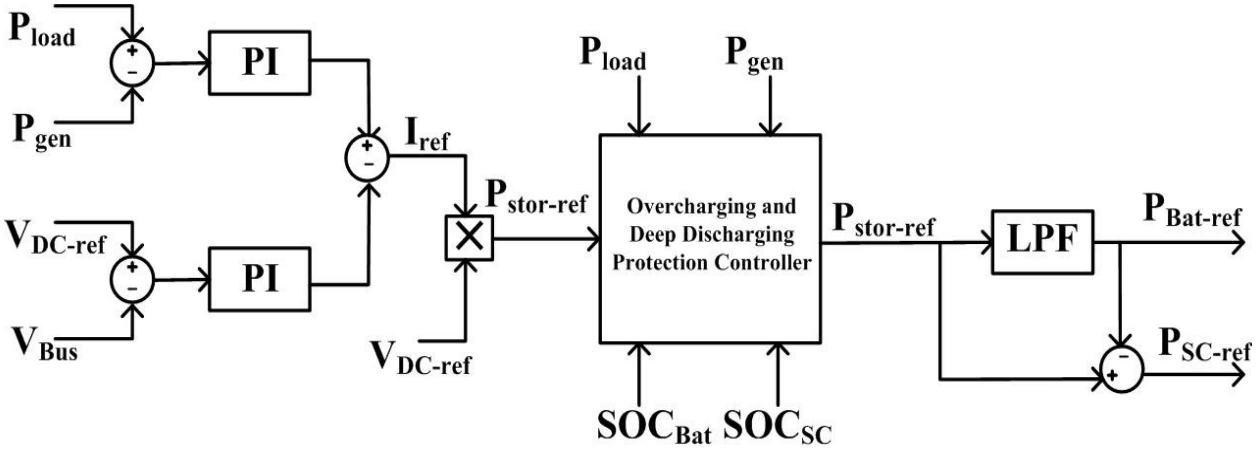

Figure 4.8: PI controller and LPF based ESM system.

4.2.1 Total Storage Reference Power ($P_{stor-ref}$) Estimation

To generate the total storage reference power ($P_{stor-ref}$), the total generated power (P_{gen}) is measured, and then the difference between the total power demand (P_{load}) and the total generated power (P_{gen}) is passed to a PI controller. The MVDC bus voltage (V_{Bus}) is measured and the difference of the reference bus voltage (V_{DC-ref}) and the measured bus voltage (V_{Bus}) is passed to another PI controller. In Figure 4.8, there are two PI controllers. One is for power mismatch and the other is for voltage mismatch. The control technique discussed in [87] is followed. Here PI controllers try to decrease the error of the total demanded load power (P_{load}), and total generation power (P_{gen}) and the error of the reference bus voltage (V_{DC-ref}) and measured bus voltage (V_{Bus}). Then the difference of the PI controllers outputs gives the reference current (I_{ref}) for the energy storages. The reference current (I_{ref}) is multiplied by the reference bus voltage (V_{DC-ref}) to generate the total storage reference power ($P_{stor-ref}$) for the battery and supercapacitor combined.

4.2.2 Overcharging and Deep Discharging Protection Controller

Since the PI controller based ESM system does not consider SOC while generating $P_{stor-ref}$, to save the battery and supercapacitor from the damages due to deep discharging and overcharging, an algorithm for protection from deep discharging and overcharging is shown in Figure 4.9 [31]. The algorithm is designed based on the SOC of the battery and supercapacitor. The SOC of the battery and supercapacitor will be regulated between 30% and 90%. Following are the condition that will be satisfied while charging or discharging.

- Charging the battery and supercapacitor if
    - SOC is 30%-90% and $P_{gen} > P_{load}$
    - SOC <30% and $P_{gen} > P_{load}$
- Discharging the battery and supercapacitor if
    - SOC is 30%-90% and $P_{gen} < P_{load}$
    - SOC >90% and $P_{gen} < P_{load}$

From Figure 4.8, the overcharging and deep discharging protection controller works as a buffer. If the SOC of HESS are higher than the upper limit (90%) and lower than the lower limit (30%), the overcharging and deep discharging protection controller blocks the output signal ($P_{stor-ref}$) of the PI controller based ESM system. For example, from Figure 4.9, if SOC of HESS are higher than 90% and $P_{gen} > P_{load}$, the output of the overcharging and deep discharging protection controller is no action required. It means no charging and discharging. No charging output because the SOC of HESS are higher than 90% and there is no need to charge the HESS. No discharging output (although the SOC of HESS are higher than 90%) because $P_{gen} > P_{load}$. It means the total power demand (P_{load}) is lower than the total generation (P_{gen}) limit, and generators are capable to supply the load power demand and there is no need to supply power from HESS.

4.2.3 Reference Power Separation Using Low Pass Filter (LPF)

The design of the LPF is exactly the same as described in the subsection 4.1.

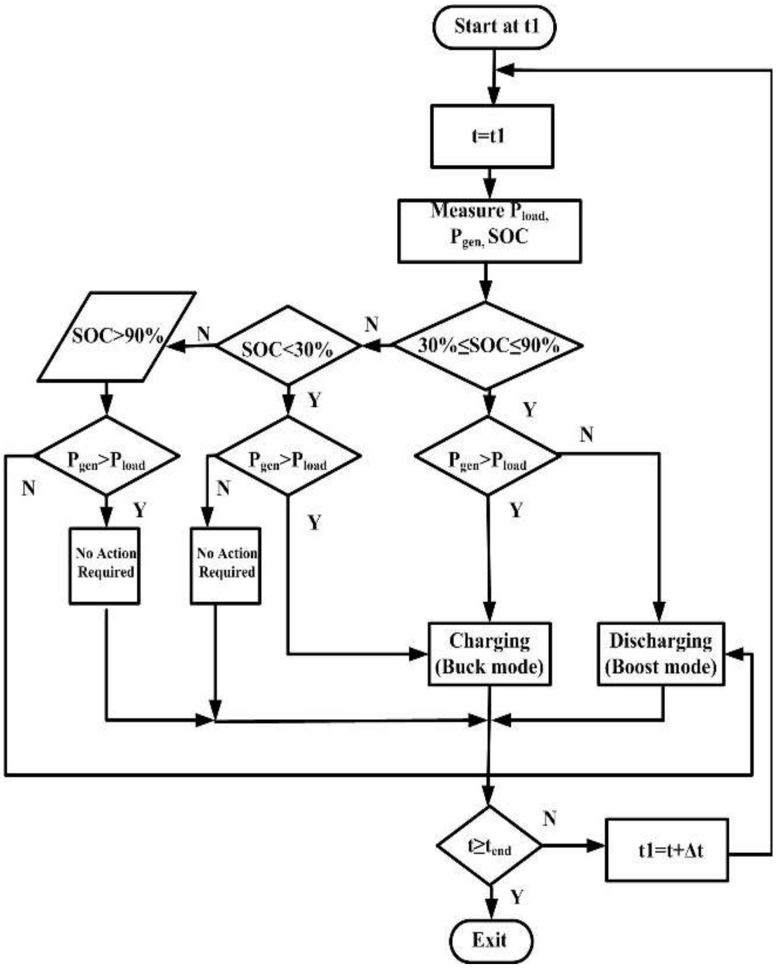

Figure 4.9: The overcharging and deep discharging control algorithm of the battery and supercapacitor.

4.3 Power Sharing Among Multiple Energy Storages

In order to add multiple batteries or supercapacitors to the MVDC system, it is required to redesign the ESM system for the multiple batteries or supercapacitors. For multiple batteries or supercapacitors, the total battery reference power and the total supercapacitor reference power can be equally distributed among the batteries and supercapacitors, respectively. But it may happen that all the batteries will not be available at the same state of charge (SOC). This is also true for the supercapacitor. So, if the same reference power is allocated for the multiple batteries or the multiple supercapacitor, then the batteries or supercapacitors with lower SOC can go into deep discharge. The deep discharging and overcharging protection controller of the PI controller based ESM system and the FL based ESM system help the batteries and supercapacitors from the situation of deep discharging by putting a deep discharge limit. For the deep discharge limit, the batteries and supercapacitors with higher SOC cannot be fully utilized if the same amount of the reference power are allocated among them. Figure 4.10 (a) shows that same amount of reference power are allocated between two batteries with different SOC. For the same amount of reference power allocation, the battery with lower SOC will hit the deep discharge limit earlier then the battery with higher SOC. In order to solve this problem, a promising solution is to allocate the reference power among the multiple batteries and supercapacitors based on their SOC. If the batteries and supercapacitor are allocated reference power based on their SOC, then the batteries and supercapacitors will reach the deep discharge limit together [86]. There is no possibility that the batteries and supercapacitors with high SOC will not be fully utilized. In this strategy, the batteries and supercapacitors with higher SOC will supply higher amount of power comparing to the batteries and supercapacitors with lower SOC. Figure 4.10 (b) shows that reference power allocated between two batteries depending on their SOC and both the batteries reach the deep discharge limit together. Same strategy is followed for the charging of the batteries and the supercapacitors. The batteries and supercapacitors will also be allocated charging reference power based on their SOC. The batteries and supercapacitors with low SOC will be allocated higher reference power for charging than the batteries with high SOC. Here two strategies of power sharing between two batteries will be discussed. Those strategies are also applicable for the supercapacitor.

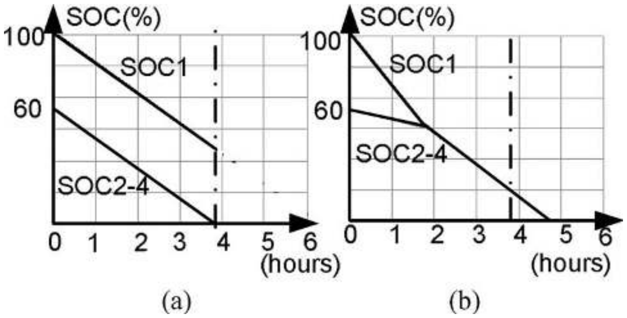

Figure 4.10: Power sharing between two batteries (a) with equal power sharing, (b) power sharing based on SOC [86].

4.3.1 Fuzzy Logic Controller for Power Sharing

The FL based power sharing is used when there are multiple batteries and supercapacitors. Figure 4.11 shows the FL based power sharing strategy with the FL controller and LPF based ESM system.The aim of this control strategy is to allocate the total battery reference power ($P_{Bat-ref}$) and total supercapacitor reference power (P_{SC-ref}) into two batteries ($P_{Bat-1-ref}$ and $P_{Bat-2-ref}$) and two supercapacitors ($P_{SC-1-ref}$ and $P_{SC-2-ref}$), respectively. The FL controller allocates reference power among multiple energy storages based on the SOC of the batteries and supercapacitors [30]. The design of the FL controller here is shown for two batteries. Same design strategy is also applicable for two supercapacitors. The power sharing FL controller has three input variables: 1) total battery reference power ($P_{Bat-ref}$), 2) SOC of the first battery (SOC_{Bat-1}), and 3) SOC of the second battery (SOC_{Bat-2}). The output variable is the power sharing coefficient (D) which divides total battery reference power ($P_{Bat-ref}$) into two batteries ($P_{Bat-1-ref}$, $P_{Bat-2-ref}$) given in (4.4) and (4.5). The three parts: *fuzzification*, *inference*, and *defuzzification* for this controller are explained below.

$$P_{Bat-1-ref} = D * P_{Bat-ref} \tag{4.4}$$

$$P_{Bat-2-ref} = (1 - D) * P_{Bat-ref} \tag{4.5}$$

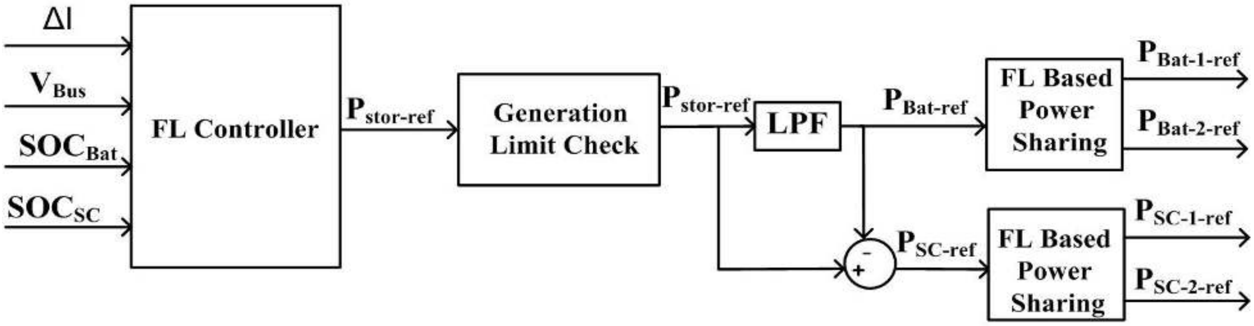

Figure 4.11: FL controller and LPF based ESM system with FL based power sharing.

4.3.1.1 Fuzzyfication. The membership functions of the input and output variables are shown in Figure 4.12. The membership functions of the total battery reference power ($P_{Bat-ref}$)

are listed as 1) Negative 2) Positive. Trapezoidal shape is chosen for them. They signify the total battery reference power ($P_{Bat-ref}$) for discharging and charging, respectively. The trapezoidal shape membership functions of the SOC of the batteries (SOC_{Bat-1}, SOC_{Bat-2}) are listed as 1) Very-Low 2) Low 3) Moderate 4) High 5) Very-High. The membership functions of the batteries represent different operating conditions. The trapezoidal membership functions of the output variable, power sharing coefficient (D), are listed as 1) d1, 2) d2, 3) d3, 4) d4, 5) d5. They represent different power sharing ratios of the batteries at different conditions of SOC.

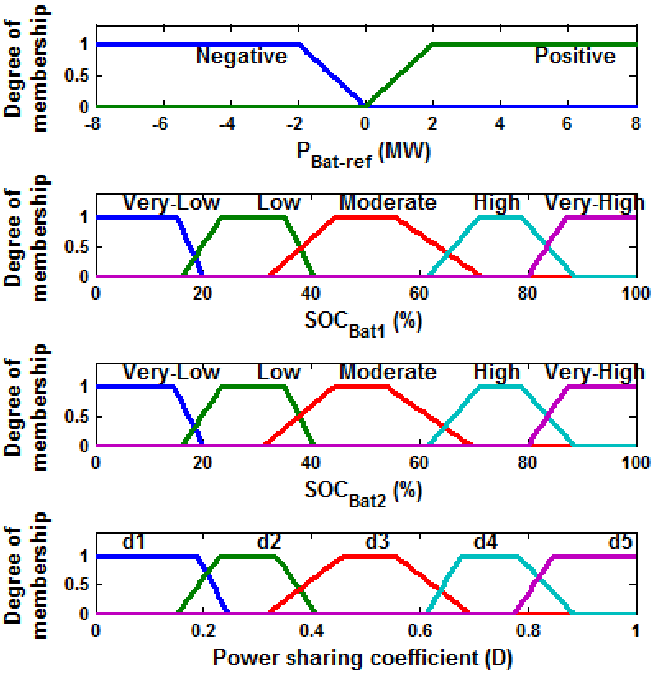

Figure 4.12: Membership functions of input and output variables for FL controller.

4.3.1.2 Inference.

The fuzzy rules are expressed as follows. A total of 50 rules are required to represent all combinations. The fuzzy rules of the FL controller are shown in Table 4.3 and Table 4.4 for different conditions of $P_{Bat-ref}$ (charging and discharging). Table 4.3 shows fuzzy rules when total battery reference power ($P_{Bat-ref}$) is Negative, which means $P_{Bat-ref}$ represents discharging reference power. Table 4.4 shows fuzzy rules when total battery reference power ($P_{Bat-ref}$) is Positive, which means $P_{Bat-ref}$ represents charging reference power. For example, IF $P_{Bat-ref}$ is Negative and SOC_{Bat-1} is Very-High and SOC_{Bat-2} is Very-Low then Power Sharing Coefficient

(D) is d5. It means maximum discharging power of $P_{Bat-ref}$ will be supplied by the first battery and the rest power will be supplied by the another battery following (4.4) and (4.5).

Table 4.3: Fuzzy Rules: Power Sharing Coefficient (D), When $P_{Bat-ref}$ Negative

D		SOC_{Bat-2}				
		Very-Low	Low	Moderate	High	Very-High
SOC_{Bat-1}	Very-Low	d3	d2	d2	d1	d1
	Low	d4	d3	d2	d1	d1
	Moderate	d4	d4	d3	d2	d2
	High	d5	d4	d4	d3	d2
	Very-High	d5	d5	d5	d4	d3

Table 4.4: Fuzzy Rules: Power Sharing Coefficient (D), When $P_{Bat-ref}$ Positive

D		SOC_{Bat-2}				
		Very-Low	Low	Moderate	High	Very-High
SOC_{Bat-1}	Very-Low	d3	d4	d4	d5	d5
	Low	d2	d3	d4	d5	d5
	Moderate	d2	d2	d3	d4	d4
	High	d1	d1	d2	d3	d4
	Very-High	d1	d1	d1	d2	d3

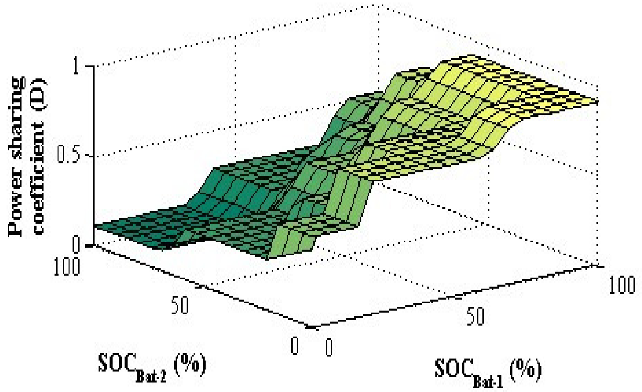

Figure 4.13: Generated surface of FL controller for D versus SOC_{Bat-1}, SOC_{Bat-2} when $P_{Bat-ref}$ is set to -4.5MW.

4.3.1.3 Defuzzyfication. The membership function of the output variable, power sharing coefficient (D) is also shown in Figure 4.12. Figure 4.13 shows the surface plot for the FL controller. It shows the evolution of D versus SOC_{Bat-1}, and SOC_{Bat-2} when $P_{Bat-ref}$ is set to -4.5MW.

4.3.2 SOC Based Power Sharing strategy

In this control strategy, the algorithm of power sharing among multiple batteries will be discussed [32]. Figure 4.14 shows the SOC based power sharing strategy with the PI controller and LPF based ESM system. Same strategy is also applicable for the supercapacitor. This controller is required when the number of battery and supercapacitor is more than one. If the total battery reference power ($P_{Bat-ref}$) is negative (discharging mode) then the initial reference power for discharging of the i^{th} battery is given in (4.6). Where L is the total number of batteries.

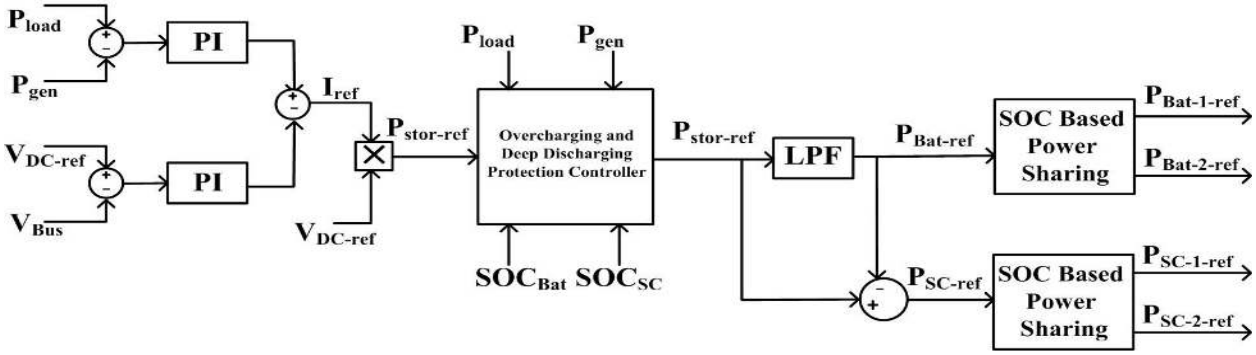

Figure 4.14: PI controller and LPF based ESM system with SOC based power sharing.

$$P^{ini}_{Bat-i-ref} = \frac{SOC_{Bat-i}}{\sum_{i=1}^{L} SOC_{Bat-i}} P_{Bat-ref} \tag{4.6}$$

If the total battery reference power ($P_{Bat-ref}$) is positive (charging mode), then the initial reference power for charging of the i^{th} battery is allocated based on the SOD (state of discharge) given in (4.7).

$$P^{ini}_{Bat-i-ref} = \frac{SOD_{Bat-i}}{\sum_{i=1}^{L} SOD_{Bat-i}} P_{Bat-ref} \tag{4.7}$$

$$SOD_{Bat-i} = 100 - SOC_{Bat-i} \tag{4.8}$$

The battery initial reference power ($P^{ini}_{Bat-i-ref}$) is required to modify according to the SOC. The modified new reference power ($P^{ini-new}_{Bat-i-ref}$) for the i^{th} battery is given in (4.9). Where, A_i is power modification factor and γ_i is SOC modification factor. Here, f_{LT} is a lookup table where the input is SOC_{Bat-i} and output is A_i. Figure 4.15 shows the the value of A_i with the variation of the SOC_{Bat-i}. The variable A_i is used to accelerate the discharging and charging of the battery near the upper and lower limit of SOC, respectively. To ensure the expected status of the battery, the SOC_{Bat-i} of the battery is modified as SOC_{ref} for three modes in (4.13). The modes are: 1) normal mode: if the SOC_{Bat-i} is within the limit then SOC_{ref} is set to SOC_{Bat-i}, 2) lower limit mode: if the SOC_{Bat-i} is less than SOC_{min}, then SOC_{ref} is set to SOC_{min} (here SOC_{min} is 30%), 3) upper limit mode: if the SOC_{Bat-i} is higher than SOC_{max}, then SOC_{ref} is set to SOC_{max} (here SOC_{max} is 90%).

$$P^{ini-new}_{Bat-i-ref} = P^{ini}_{Bat-i-ref} + \Delta P_i \tag{4.9}$$

$$\Delta P_i = A_i \gamma_i \tag{4.10}$$

$$A_i = f_{LT}(SOC_{Bat-i}) \tag{4.11}$$

$$\gamma_i = \frac{SOC_{ref} - SOC_{Bat-i}}{\dfrac{SOC_{max} - SOC_{min}}{2}} \tag{4.12}$$

$$SOC_{ref} = \begin{cases} 30\%, & \text{if} SOC_{Bat-i} \leq 30\% \\ 90\%, & \text{if} SOC_{Bat-i} \geq 90\% \\ SOC_{Bat-i}, & \text{otherwise} \end{cases} \tag{4.13}$$

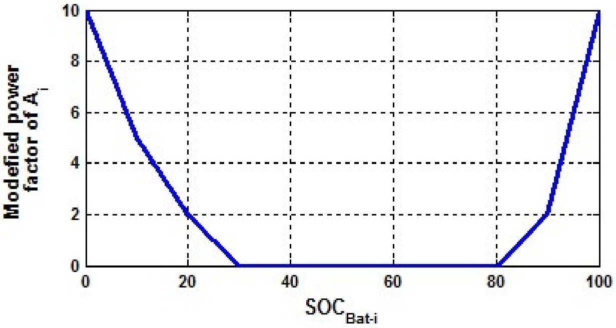

Figure 4.15: Modified power factor (A_i) vs SOC_{Bat-i}.

CHAPTER 5

SIMULATION RESULTS

Parameters [27, 60] used for the simulation are listed in Table 5.1 and Table 5.2. For simulation purpose, the average model of DAB and MMC converters are used. Figure 5.1 shows the 5kV reduced MVDC system of IEEE 1709 standard for simulation purposes, which has one Main AC Turbine Generator (MTG) and one Auxiliary AC Turbine Generator (ATG) as the source of power. The total load of the MVDC system is divided into propulsion load, ship service load and radar load and pulsed load.

Table 5.1: The Simple Notional MVDC System Parameters

Type	Name	Quantity	P (MW)	P_{tot} (MW)
Source	MTG	1	36	48
	ATG	1	4	
	Battery	1	4	
	SC	1	4	
Load	Normal Loads (Propulsion load, service loads and radar load)		40	44
	Pulsed Load	1	4	

Table 5.2: Battery and Supercapacitor Parameters

Battery		Supercapacitor	
Parameters	Values	Parameters	Values
Rated capacity	800Ah	Rated capacitance	500.25F
Nominal voltage	800V	Rated voltage	550V
Fully charged voltage	931.18V	Initial voltage	465V
Initial SOC	75%	Initial SOC	82.65%

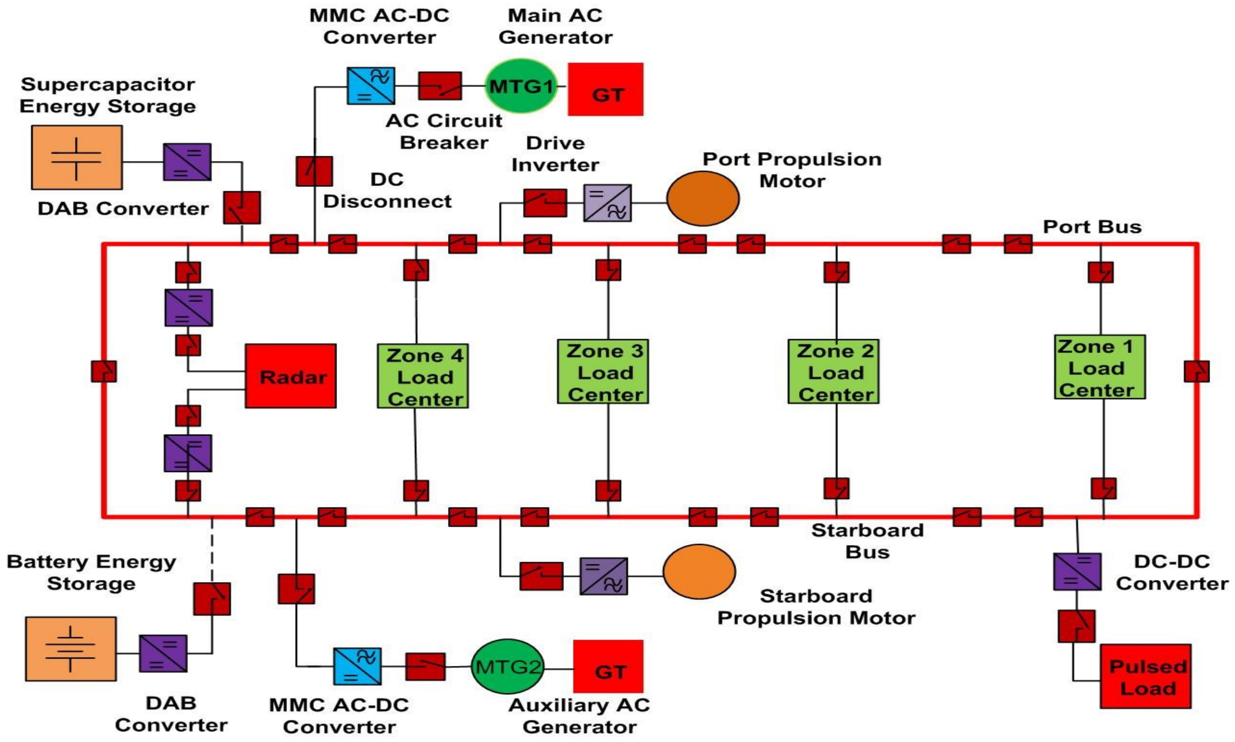

Figure 5.1: 5kV MVDC system (40MW).

5.1 Simulation Results with FL Based Two Level Strategy

Parameters used for the simulation are kept same as listed in Table 5.1 and Table 5.2. To show the performances of the of the FL based two level ESM system, when the SOC of HESS within the upper (90%) and lower limit (30%), the SOC of the battery (75%) and supercapacitor (82.65%) are kept same as listed in the Table 5.2.

At t=0.3s, 34MW load is connected to the system. The addition of the load decreases the bus voltage momentarily and increases the total load current as shown in Figure 5.2 and Figure 5.3. As the bus voltage goes down, the FL1 controller provides negative total storage reference power ($P_{stor-ref}$) (shown in Figure 5.4). The FL2 controller separates the $P_{stor-ref}$ into two parts: the battery reference power ($P_{Bat-ref}$) and the supercapacitor reference power (P_{SC-ref}) (Figure 5.4). The $P_{Bat-ref}$ and P_{SC-ref} are sent to the controllers of the DAB converters. Figure 5.5 shows the actual power responses of the battery and supercapacitor for the two level FL controller based ESM system. Figure 5.6, Figure 5.7, and Figure 5.8 show the voltage, current and SOC of the battery and supercapacitor, respectively, for the FL based two level ESM system. So, the simulation results show that FL based two level ESM system is capable of supporting the MVDC system in a transient situation.

At t=0.6s, another 6MW load is connected to the MVDC system. The total load of the system is now 40MW. With the addition of the load, Figure 5.4 shows that the FL1 controller generates negative $P_{stor-ref}$ for discharging. The FL2 controller separates $P_{stor-ref}$ into two parts: $P_{Bat-ref}$ and P_{SC-ref}. Figure 5.5 shows the actual power responses of the battery and supercapacitor for the two level FL controller based ESM system.

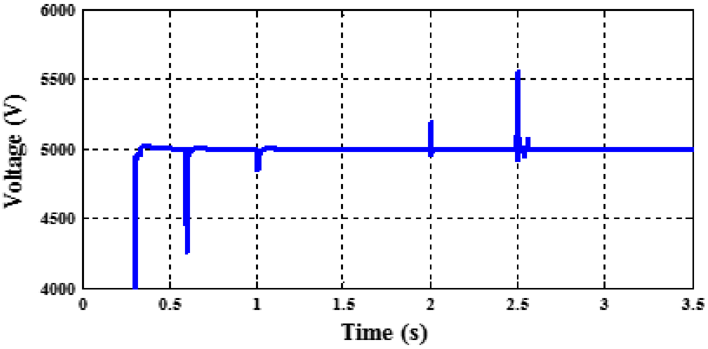

Figure 5.2: MVDC bus voltage.

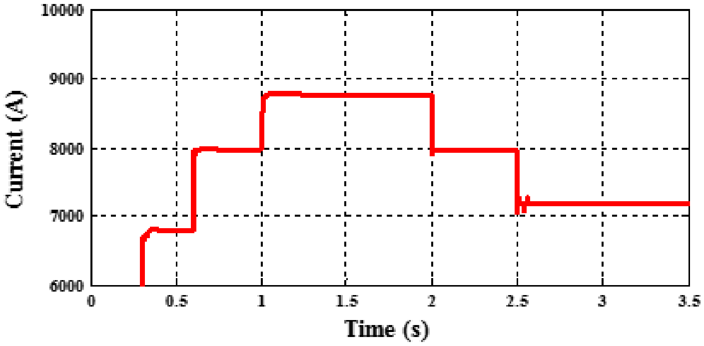

Figure 5.3: Total load current.

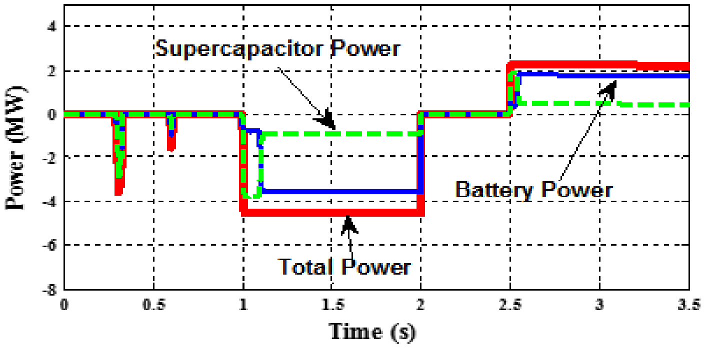

Figure 5.4: The reference power produced by FL based two level ESM system.

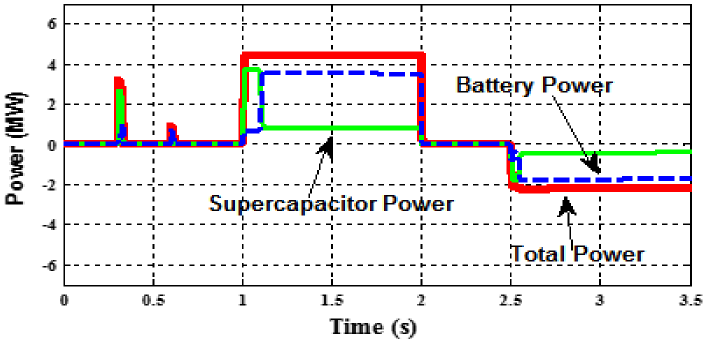

Figure 5.5: The actual power responses of the HESS.

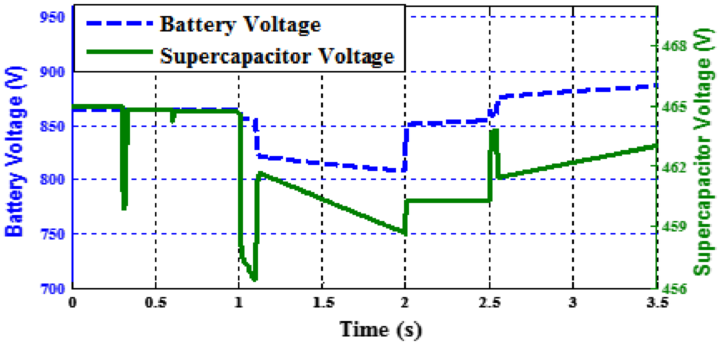

Figure 5.6: Battery and supercapacitor voltage responses.

At t=1s, 4MW pulsed load is connected to the MVDC system and it continues until t=2s. Now, the total load of the system is 44MW. But the total generation capacity of the MVDC

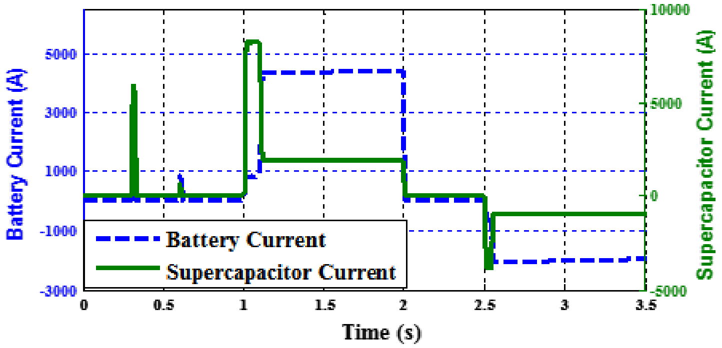

Figure 5.7: Battery and supercapacitor current responses.

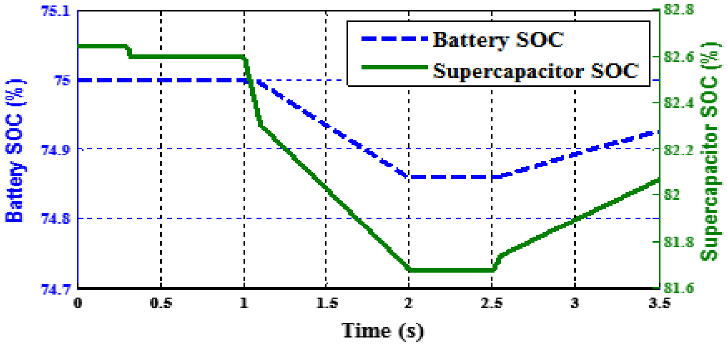

Figure 5.8: Battery and supercapacitor SOC.

system is 40MW. So, the addition of the pulsed load exceeds the total generation capacity of the MVDC system. These effects are shown in Figure 5.2 and Figure 5.3, where it is shown that the bus voltage goes down momentarily and the total load current increases. As the total power requirement (44MW) is higher than the total generation capacity (40MW), FL1 controller generates negative $P_{stor-ref}$ for discharging. It is shown in Figure 5.4 that FL2 controller separates $P_{stor-ref}$ into two parts: $P_{Bat-ref}$ and P_{SC-ref}. Figure 5.5 shows the actual power response of the battery and supercapacitor for the two level FL controller based ESM system for supporting the pulsed load. Figure 5.6, Figure 5.7, and Figure 5.8 show the voltage, current and SOC of the battery and supercapacitor, respectively, for the two level FL controller based ESM system for the discharging period, t=1s to t=2s. These figures show that during t=1s to t=2s, the voltages of the battery and supercapacitor go down, output currents increase and the SOC decrease for discharging power to the MVDC system.

From t=2s to t=2.5s, the total load remains at 40MW. At t=2.5s, a 4MW load is rejected from the MVDC system. This causes the bus voltage to increase and a decrease in total current as shown in Figure 5.2 and Figure 5.3. Figure 5.4 shows, the FL1 controller provides positive $P_{stor-ref}$ for charging, during t=2.5s to t=3.5s. The FL2 controller separates $P_{stor-ref}$ into $P_{Bat-ref}$ and P_{SC-ref}. Figure 5.5 shows the actual power consumed by the battery and supercapacitor from the MVDC system for the two level FL controller based ESM system. In this case, from Figure 5.5, powers are negative because the battery and supercapacitor work in the charging mode, during t=2.5s to t=3.5s. Figure 5.6, Figure 5.7, and Figure 5.8 show the voltage, current and SOC of the battery and supercapacitor, respectively, for the two level FL controller based ESM system. These figures show that during t=2.5s to t=3.5s, voltages of the battery and supercapacitor go up, the SOC increase and the currents go to negative because that time, the battery and supercapacitor work in the charging mode.

5.2 Simulation Results with FL Controller and LPF Based Strategy

From Figure 5.4, the FL2 controller separates the total storage reference power ($P_{stor-ref}$) into battery reference power ($P_{Bat-ref}$) and supercapacitor reference power (P_{SC-ref}). At Figure 5.4, reference power of battery ($P_{Bat-ref}$) shows very sharp response and it goes from zero to nearly -4.5MW momentarily. But, battery has low power density and it cannot respond to sharp power changes. So, low pass filter (LPF) is used instead of FL2 controller for separation of total storage reference power ($P_{stor-ref}$) into battery reference power ($P_{Bat-ref}$) and supercapacitor reference power (P_{SC-ref}). Simulation results are shown based on the different conditions of SOC of the battery and supercapacitor. For simulation purpose, same parameters of Table 5.1 and Table 5.2 are used.

Case 1: Performances of the FL Controller and LPF Based ESM System when the SOC of HESS within the Limit: Parameters used for the simulation are kept same as listed in Table 5.1 and Table 5.2. To show the performances of the FL controller and LPF based ESM system, when the SOC of HESS within the upper (90%) and lower limit (30%), the SOC of the battery (75%) and supercapacitor (82.65%) are kept same as listed in the Table 5.2.

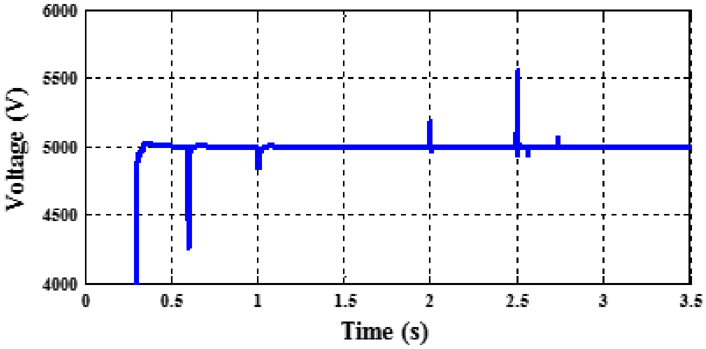

Figure 5.9: MVDC bus voltage (case 1).

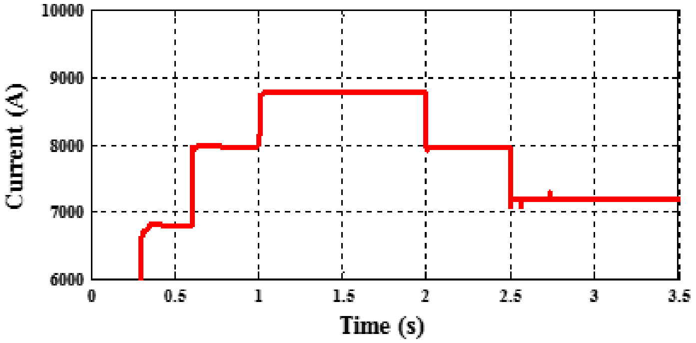

Figure 5.10: Total load current (case 1).

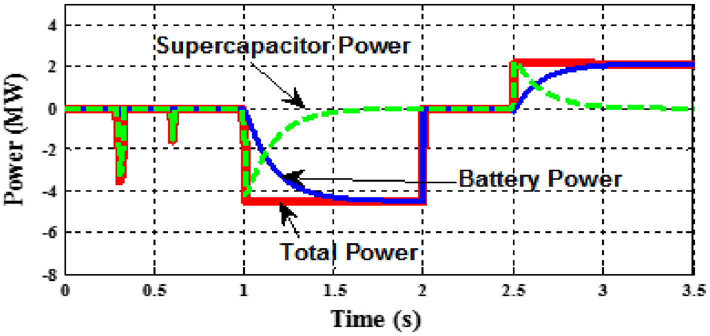

Figure 5.11: The reference power produced by FL controller and LPF based ESM system (case 1).

In order to show the performances of the FL controller and LPF based ESM system, same operations of FL based two level ESM system are done. At t=0.3s and t=0.6s, 34MW and 6MW load are connected to the MVDC system, respectively. Those are transient operations, simulation results for the FL controller and LPF based ESM system are given in Figure 5.9 to Figure 5.15. Again at t=1s, 4MW pulsed load is added to the MVDC system and it is continued until t=2s. With the addition of pulsed load, the total load (44MW) goes higher than the total generation capacity (40MW). Considering those operations, the FL controller and LPF based ESM system provides negative total storage reference power ($P_{stor-ref}$) for discharging (Figure 5.11). The LPF splits, $P_{stor-ref}$ between battery reference power ($P_{Bat-ref}$) and supercapacitor reference power (P_{SC-ref}). Comparing the generated reference power of the battery ($P_{Bat-ref}$) and supercapacitor (P_{SC-ref}) by the FL based two level ESM system and FL controller and LPF based ESM system (Figure 5.4 and Figure 5.11), it shows that the generated battery reference power ($P_{Bat-ref}$) for discharging by the FL controller and LPF based ESM system increases slowly and does not show sharp raising (Figure 5.11). But, for the FL controller based two level ESM system, the $P_{Bat-ref}$ shows sharp response (Figure 5.4). At t=2.5s, a 4MW load is rejected from the MVDC system.

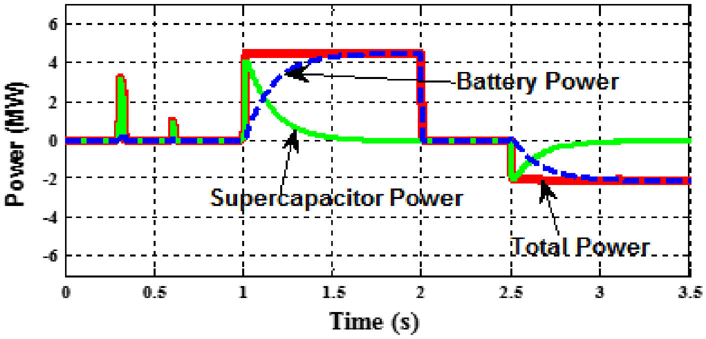

Figure 5.12: The actual power response of the HESS (case 1).

With the rejection of 4MW load, the FL controller and LPF based ESM system provides positive total storage reference power ($P_{stor-ref}$) for charging (Figure 5.11). The LPF splits, $P_{stor-ref}$ between battery reference power ($P_{Bat-ref}$) and supercapacitor reference power (P_{SC-ref}). Again, the generation of $P_{Bat-ref}$ for charging by the FL based two level ESM system and FL controller and LPF based ESM system are different (Figure 5.4 and Figure 5.11). It shows that the $P_{Bat-ref}$ for charging by the FL controller and LPF based ESM system increases slowly, and does not show sharp raising (Figure 5.11). But, for the FL controller based two level strategy, the $P_{Bat-ref}$ shows sharp response (Figure 5.4).

So, the simulation results show that FL controller and LPF filter based ESM system shows superior performances than the two level FL controller based ESM system in the case of battery power management. As, the FL controller and LPF filter based ESM deals efficiently the low power density characteristics of the battery than the two level FL controller based ESM system.

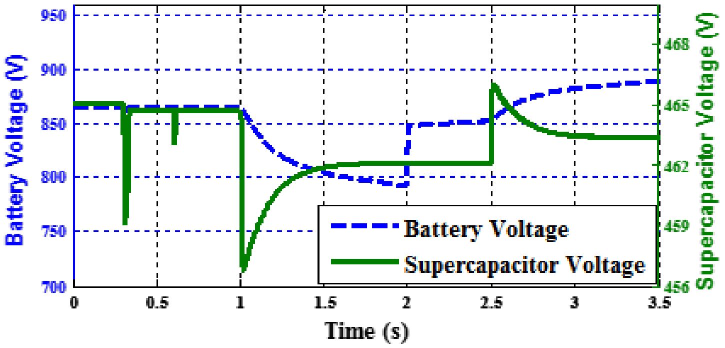

Figure 5.13: Battery and supercapacitor voltage response (case 1).

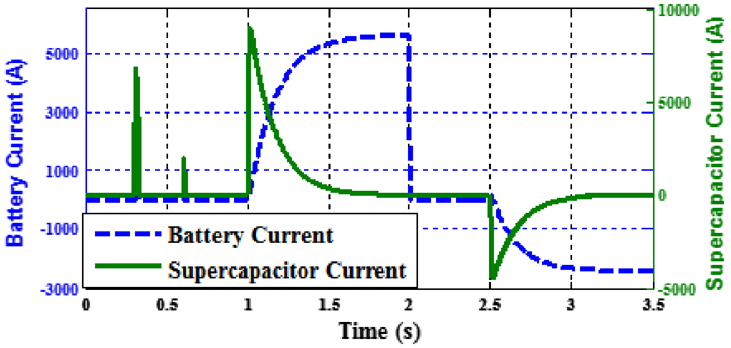

Figure 5.14: Battery and supercapacitor current response (case 1).

Case 2: Performances of the FL Controller and LPF Based ESM System at Low SOC of HESS: To show the performances of the FL controller and LPF based ESM system with the situation of low SOC, the SOC of the battery is set 20% as the initial SOC and the supercapacitors initial voltage is kept 170V with SOC of 25.5% in the Table 5.2.

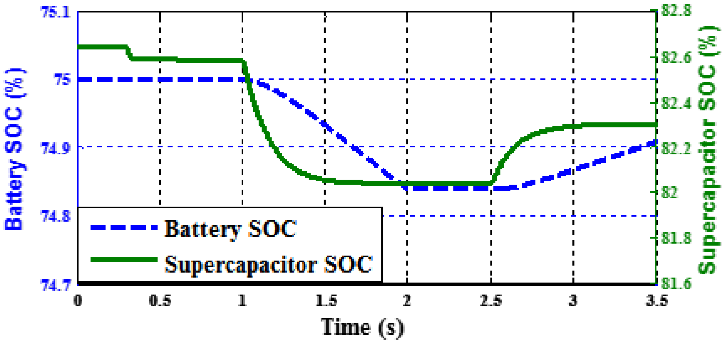

Figure 5.15: Battery and supercapacitor SOC (case 1).

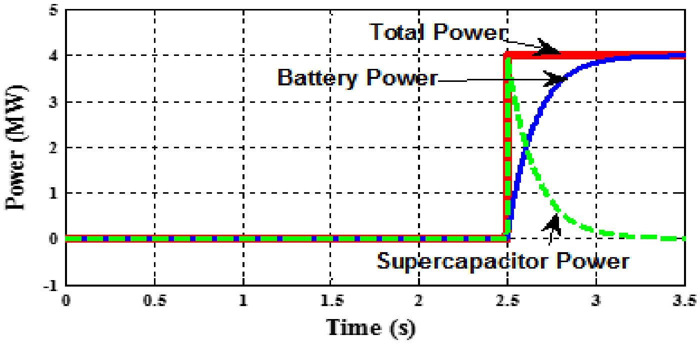

Figure 5.16: The reference power produced by FL controller and LPF based ESM system (case 2).

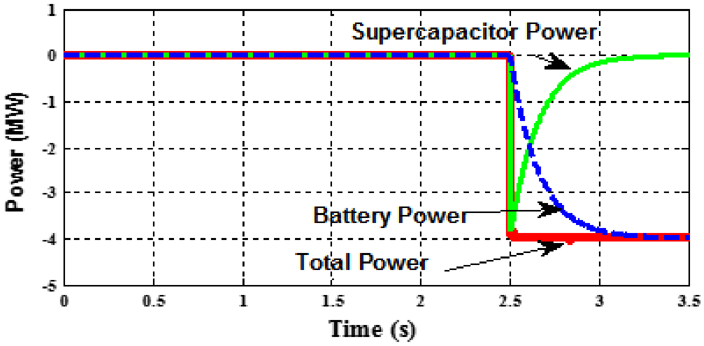

Figure 5.17: The actual power response of the HESS (case 2).

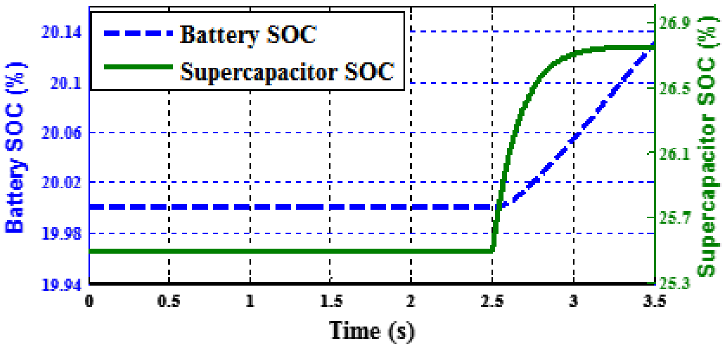

Figure 5.18: Battery and supercapacitor SOC (case 2).

At t=0.3s and t=0.6s, 34MW and 6MW load are connected to the MVDC system, respectively. Again at t=1s, 4MW pulsed load is added to the MVDC system and it is continued until t=2s. With the addition of pulsed load, the total load (44MW) goes higher than the total generation capacity (40MW). The FL controller and LPF based ESM system is expected to provide the negative ($P_{stor-ref}$) for discharging. For the FL controller, the reference power generation depends also on the SOC of the battery and supercapacitor. Figure 5.16 shows that due to low SOC (20% and 25.5%, Figure 5.18), the FL controller provides zero reference power. Simulation results after t=2s for the FL controller and LPF bases ESM system are same as shown earlier in the case 1, where at t=2.5s, the battery and supercapacitor start charging and continue until t=3.5s. Figure 5.17 shows actual power consumed by the battery and supercapacitor from the MVDC system.

Case 3: Performances of the FL Controller and LPF based ESM System at High SOC of HESS: To show the performances of the FL controller and LPF based ESM system with the situation of high SOC, the SOC of the battery is set 94% as the initial SOC and the supercapacitors initial voltage is kept 535V with SOC of 97.02% in the Table 5.2.

From Figure 5.19, the simulation results up to t=2.5s for the FL controller and LPF based ESM system are same as shown earlier in the case 1, where at t=0.3s, t=0.6s and t=1s to t=2s, the battery and supercapacitor supply power to the MVDC system (Figure 5.19). Figure 5.20 shows actual power supplied to the MVDC system by the battery and supercapacitor. At t=2.5s, 4MW load is rejected, and the FL controller and LPF based ESM system is expected to provide the positive $P_{stor-ref}$ for charging. For the FL controller, the reference power generation depends also on the SOC of the battery and supercapacitor. Due to the high SOC of the battery and

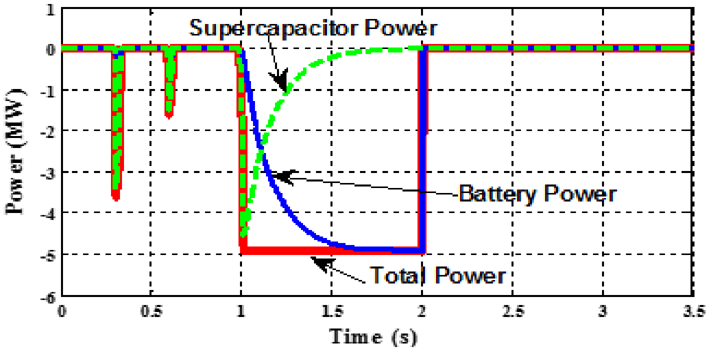

Figure 5.19: The reference power produced by FL controller and LPF based ESM system (case 3).

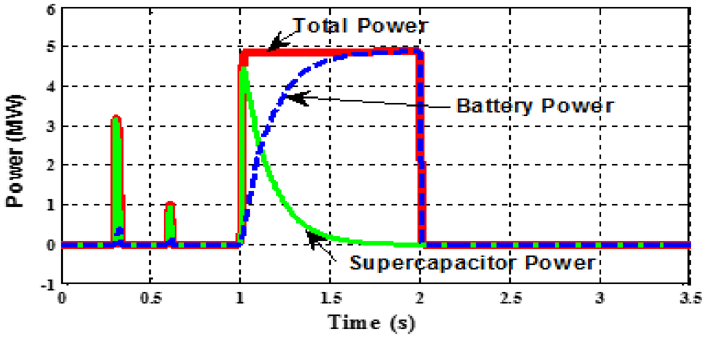

Figure 5.20: The actual power response of the HESS (case 3).

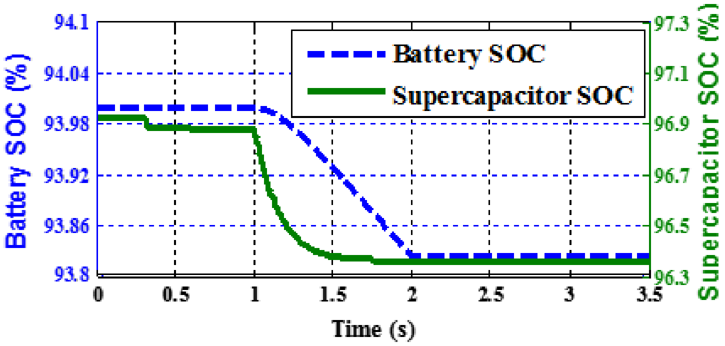

Figure 5.21: Battery and supercapacitor SOC (case 3).

supercapacitor (nearly 94% and 97.02%, Figure 5.21), Figure 5.19 shows that the FL controller provides zero reference power for charging.

5.3 Simulation Results with PI Controller and LPF Based Strategy

Simulation results are shown to verify the performances of the PI controller and LPF based ESM system for maintaining the bus voltage within the limit and supporting the generators when the total load requirement is higher than the total generation capacity. Simulation results are shown based on the different conditions of SOC of the battery and supercapacitor.

Case 1: Performances of the PI Controller and LPF Based ESM System when the SOC of HESS within the Limit: Parameters used for the simulation are kept same as listed in Table 5.1 and Table 5.2. To show the performances of the of the PI controller and LPF based ESM system, when the SOC of HESS within the upper (90%) and lower limit (30%), the SOC of the battery (75%) and supercapacitor (82.65%) are kept same as listed in the Table 5.2.

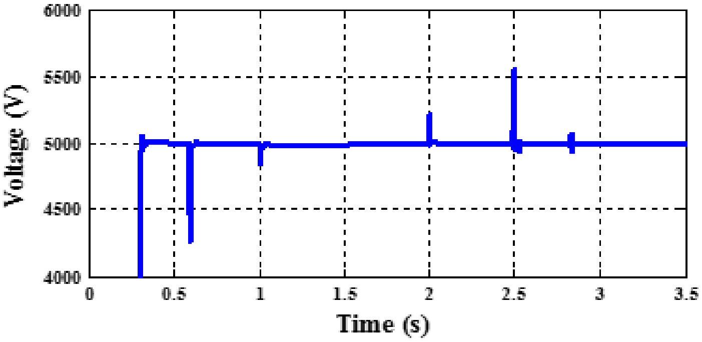

Figure 5.22: MVDC bus voltage (case 1).

To show the performances of the PI controller and LPF based ESM system, same operations of FL controller and LPF based ESM system are done. From Figure 5.22 and Figure 5.23, at *t*=0.3s, 34MW load is connected to the system. As the addition of the load is transient effect, the PI controller based ESM system provides negative total storage reference power ($P_{stor-ref}$) for the battery and supercapacitor for discharging (shown in Figure 5.24) to support the generators. The negative reference power ($P_{stor-ref}$) represents that the HESS needs to supply this amount of power to the MVDC system. The low pass filter separates the total storage reference power ($P_{stor-ref}$) into two parts, the low-frequency component as the battery reference power ($P_{Bat-ref}$)

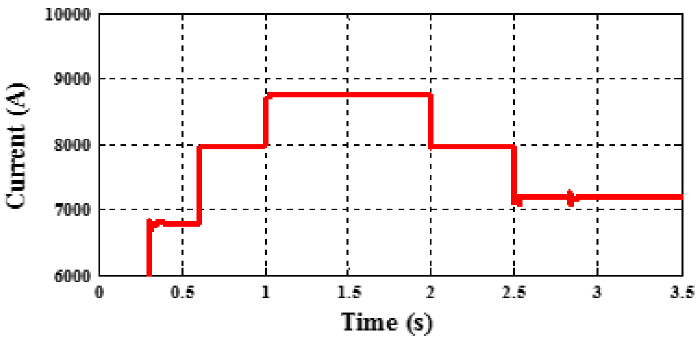

Figure 5.23: Total load current (case 1).

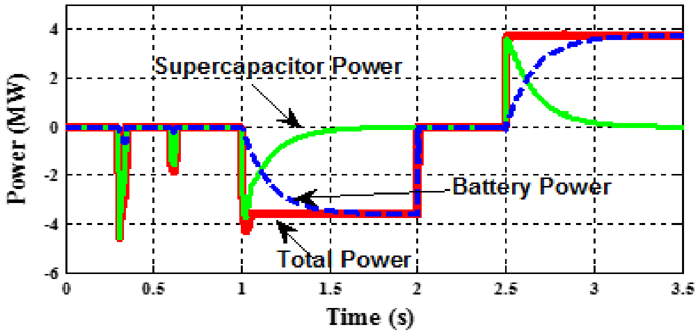

Figure 5.24: The reference power produced by PI controller and LPF based ESM system (case 1).

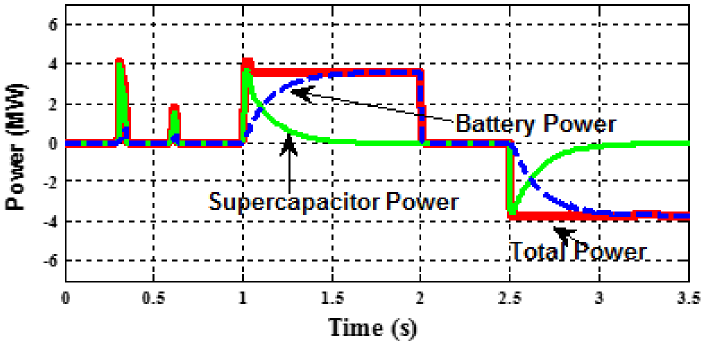

Figure 5.25: The actual power response of the HESS (case 1).

and the high-frequency component as the reference power (P_{SC-ref}) for the supercapacitor. These battery reference power ($P_{Bat-ref}$) and supercapacitor reference power (P_{SC-ref}) are sent to the controllers of the DAB converters. Figure 5.25 shows the actual power responses of the battery and supercapacitor for the PI controller based ESM system. Figure 5.26, Figure 5.27, and Figure 5.28 show the voltage, current and SOC, respectively, of the battery and supercapacitor for the PI controller based ESM system. So, the simulation results show that the ESM strategy based on PI controller is capable of supporting the MVDC system in a transient situation.

At t=0.6s, another 6MW load is connected to the MVDC system. The total load of the system is now 40MW. Figure 5.22 and Figure 5.23 show that this causes the bus voltage to go down and increases the total load current. As the bus voltage goes down, Figure 5.24 shows that the PI controller based ESM system generates negative total storage reference power ($P_{stor-ref}$) for discharging. The LPF separates the ($P_{stor-ref}$) into two parts, $P_{Bat-ref}$ and P_{SC-ref}. Figure 5.25 shows the actual power response of the battery and supercapacitor.

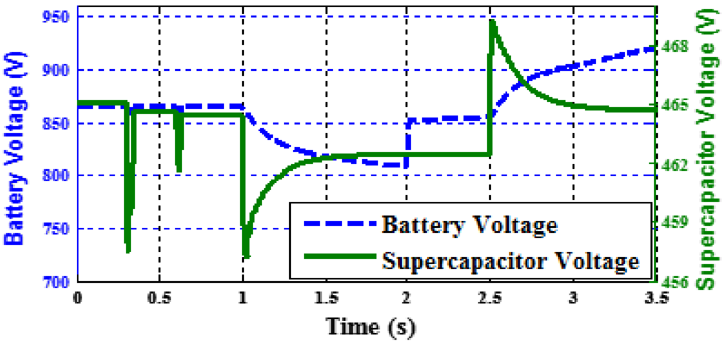

Figure 5.26: Battery and supercapacitor voltage response (case 1).

At t=1s, 4MW pulsed load is connected to the MVDC system and it continues until t=2s. Now, the total load of the system is 44MW. But the total generation capacity of the MVDC system is 40MW. So, the addition of the pulsed load exceeds the total generation capacity of the MVDC system. These effects are shown in Figure 5.22 and Figure 5.23, where it is shown that the bus voltage goes down momentarily and the total load current increases. As the total power requirement (44MW) is higher than the total generation capacity (40MW), the PI controller based ESM system generates negative total storage reference power ($P_{stor-ref}$) for discharging. It is shown in Figure 5.24 that the LPF separates the $P_{stor-ref}$ into two parts, $P_{Bat-ref}$ and P_{SC-ref}. Figure 5.25 shows

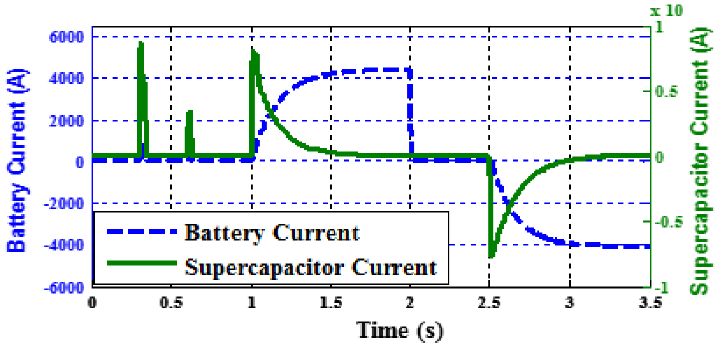

Figure 5.27: Battery and supercapacitor current response (case 1).

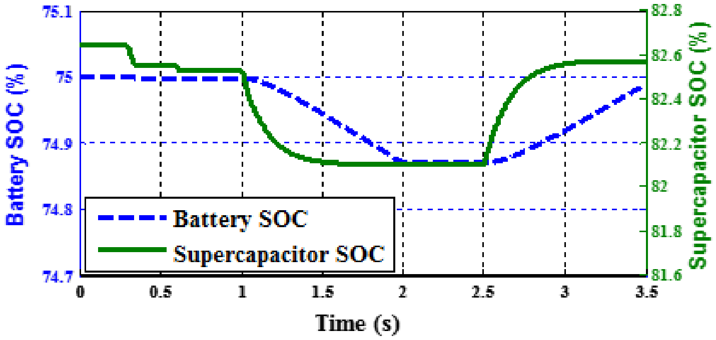

Figure 5.28: Battery and supercapacitor SOC (case 1).

the actual power responses of the battery and supercapacitor for the PI controller based ESM system for supporting the pulsed load. Figure 5.26, Figure 5.27, Figure 5.28 show the voltage, current and SOC, respectively, of the battery and supercapacitor for the discharging period, t=1s to t=2s. These figures show that during t=1s to t=2s, the voltages of the battery and supercapacitor go down, output currents increase and the SOC decrease for discharging power to the MVDC system.

From t=2s to t=2.5s, the total load remains at 40MW. At t=2.5s, a 4M load is rejected from the MVDC system. This causes the bus voltage to increase and a decrease in total current as shown in Figure 5.22 and Figure 5.23. Figure 5.24 shows, the PI controller based ESM system provides positive total storage reference power ($P_{stor-ref}$) for charging, during t=2.5s to t=3.5s. The LPF separates $P_{stor-ref}$ into $P_{Bat-ref}$ and P_{SC-ref}. Figure 5.25 shows the actual power consumed by the battery and supercapacitor from the MVDC system, during t=2.5s to t=3.5s. In this case, from

Figure 5.25, the actual power responses are negative because the battery and supercapacitor work in the charging mode, during t=2.5s to t=3.5s. Figure 5.25, Figure 5.27, and Figure 5.28 show the voltage, current and SOC, respectively, of the battery and supercapacitor for the charging period, t=2.5s to t=3.5s. These figures show that during t=2.5s to t=3.5s, voltages of the battery and supercapacitor go up, the SOC increase and the currents go to negative because during t=2.5s to t=3.5s, the battery and supercapacitor work in the charging mode.

Case 2: Performances of the PI Controller and LPF Based ESM System at Low SOC of HESS: To show the performances of the PI controller and LPF based ESM system with the situation of low SOC, the SOC of the battery is set 20% as the initial SOC and the supercapacitors initial voltage is kept 170V with SOC of 25.5% in the Table 5.2.

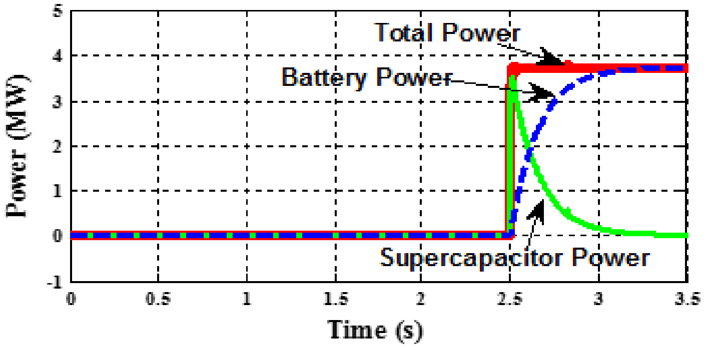

Figure 5.29: The reference power produced by PI controller and LPF based ESM system (case 2).

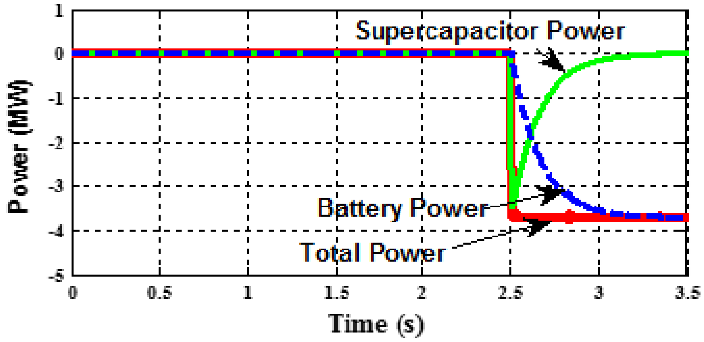

Figure 5.30: The actual power response of the HESS (case 2).

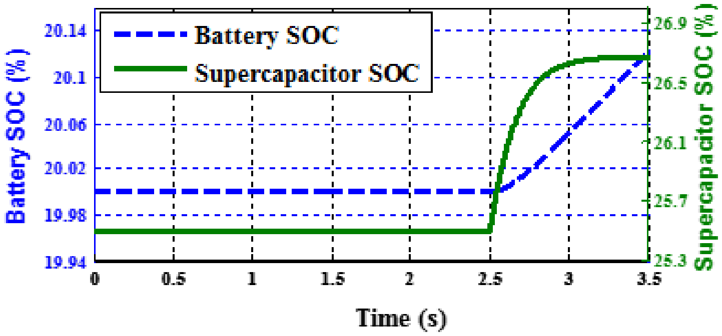

Figure 5.31: Battery and supercapacitor SOC (case 2).

At t=0.3s and t=0.6s, 34MW and 6MW load are connected to the MVDC system, respectively. The addition of the load creates momentary voltage dip and increases the total load current. At t=1s, 4MW pulsed load is added to the MVDC system and it is continued until t=2s. With the addition of pulsed load, the total load (44MW) goes higher than the total generation capacity (40MW). Considering these situations, it is expected that the PI controller and LPF based ESM system will provide the negative total storage reference power ($P_{stor-ref}$) for discharging of the battery and supercapacitor. As the overcharging and deep discharging protection controller is connected to the PI controller based ESM system, Figure 5.29 shows that the total storage reference power ($P_{stor-ref}$) for discharging is zero. Because of low SOC of the battery and supercapacitor (20% and 25.2%), the charge controller blocks the PI controller's negative total storage reference power ($P_{stor-ref}$) signal. Figure 5.31 shows the SOC of the battery and supercapacitor for the PI controller based ESM system. In this case, the battery and supercapacitor are not allowed to discharge for the PI controller based ESM system. Figure 5.31 shows that the SOC of the battery and supercapacitor are 20% and 25.2% at the beginning, and they do not change as they are not allowed to discharge up to t=2.5s. Simulation results at t=2.5s shows the battery and supercapacitor charge up to t=3.5s when load is shed. Figure 5.30 shows actual power consumed by the battery and supercapacitor from the MVDC system.

Case 3: Performances of the PI Controller and LPF based ESM System at High SOC of HESS: To show the performances of the PI controller and LPF based ESM system with the situation of high SOC, the SOC of the battery is set 94% as the initial SOC and the supercapacitors initial voltage is kept 535V with SOC of 97.02% in the Table 5.2.

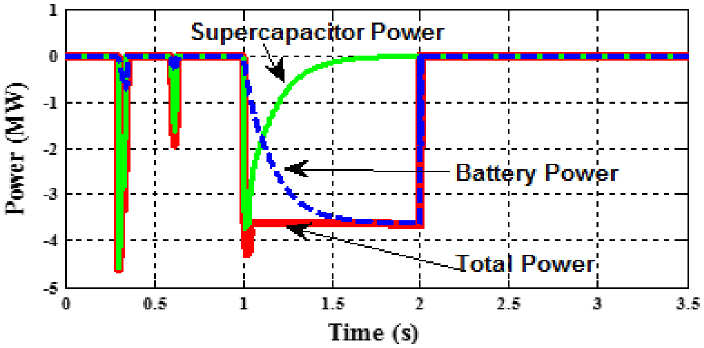

Figure 5.32: The reference power produced by PI controller and LPF based ESM system (case 3).

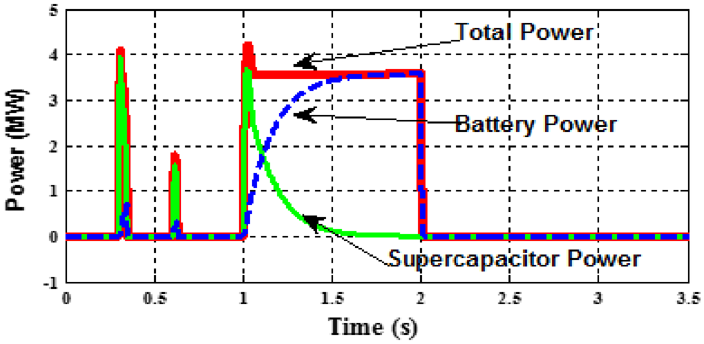

Figure 5.33: The actual power response of the HESS (case 3).

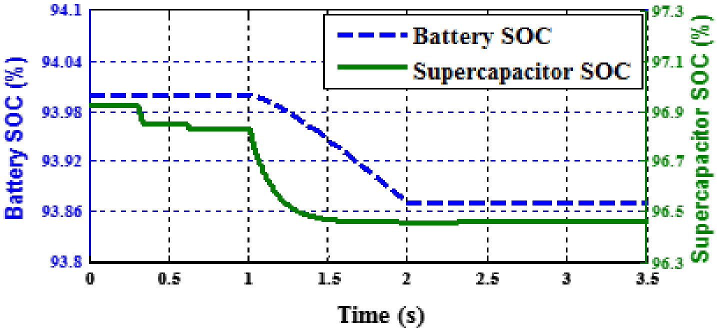

Figure 5.34: Battery and supercapacitor SOC (case 3).

In this case, the simulation results up to t=2.5s for the PI controller and LPF based ESM system are the same as shown in the case 1, where at t=0.3s, t=0.6s, and t=1s to t=2s, the battery and supercapacitor supply power to the MVDC system (Figure 5.32). Figure 5.33 shows actual power supplied to the MVDC system by the battery and supercapacitor. At t=2.5s, 4MW load is rejected and it is expected that the PI controller and LPF based ESM system will provide the positive total storage reference power ($P_{stor-ref}$) for charging of the battery and supercapacitor. As the overcharging protection controller is connected to the PI controller based ESM system, Figure 5.32 shows that the total storage reference power ($P_{stor-ref}$) for charging is zero. Because of high SOC of the battery and supercapacitor (94% and 97.02%), the charge controller blocks the PI controller's positive total storage reference power ($P_{stor-ref}$) signal. Figure 5.34 shows the SOC of the battery and supercapacitor for the PI controller based ESM system. In this case, the battery and supercapacitor are not allowed to charge from t=2.5s to t=3.5s and the SOC of them do not change after t=2.5s.

5.4 Comparison of Performances of the FL and PI Controller Based ESM Systems

Parameters [27, 60] used for the simulation are listed in Table 5.1 and Table 5.2.

Case 1: Comparison of performances of the FL and PI controller based ESM systems when the SOC of HESS within the limit: For this case, the SOC of the battery and supercapacitor are set at 75% and 82.65%.

At t=0.3s, 34MW load is connected to the system which decreased the bus voltage momentarily and increased the total load current as shown in Figure 5.35. As the bus voltage goes down, the FL and PI controllers provide negative total storage reference power ($P_{stor-ref}$) (shown in Figure 5.36a). The low pass filter separates $P_{stor-ref}$ into two parts: the battery reference power ($P_{Bat-ref}$) and supercapacitor reference power (P_{SC-ref}) (Figure 5.36b and Figure 5.36c). The $P_{Bat-ref}$ and P_{SC-ref} are sent to the controllers of the DAB converters. Figure 5.37 shows the actual power responses of the battery and supercapacitor for the FL and PI controller based ESM systems. Figure 5.38 and Figure 5.39 show the voltage, current and SOC of the battery and supercapacitor, respectively, for both FL and PI controller based ESM systems. Simulation results show that the ESM systems based on FL and PI controllers are capable of supporting the MVDC system in a transient situation.

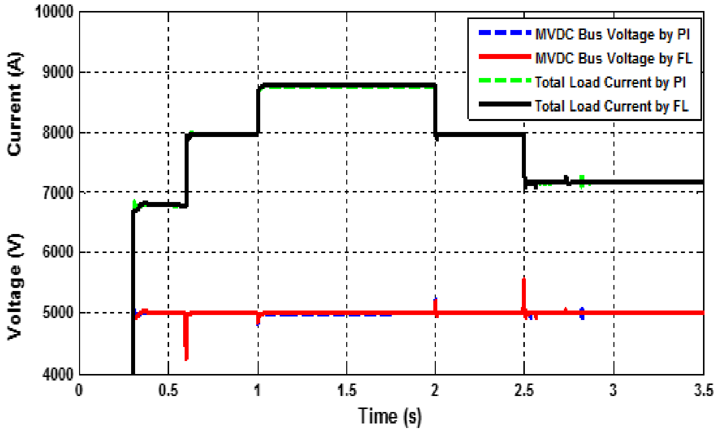

Figure 5.35: The MVDC bus voltage and total load current with the FL and PI controller based ESM systems (case 1).

At t=0.6s, another 6MW load is connected to the MVDC system. The total load of the system is now 40MW. With the addition of the load, Figure 5.36 shows that the FL and PI controller generate negative $P_{stor-ref}$ for discharging. The LPF separates $P_{stor-ref}$ into two parts: $P_{Bat-ref}$ and P_{SC-ref}. Figure 5.37 shows the actual power responses of the battery and supercapacitor for the FL and PI controller based ESM systems.

At t=1s, 4MW pulsed load is connected to the MVDC system and it continues until t=2s. Now, the total load of the system is 44MW, which exceeds the total generation capacity of the MVDC system. These effects are shown in Figure 5.35, where it is shown that the bus voltage goes down slightly and the total load current increases. As the total power requirement (44MW) is higher than the total generation capacity (40MW), the FL and PI controller based ESM systems generate negative $P_{stor-ref}$ for discharging. Figure 5.37 shows the actual power responses of the battery and supercapacitor for the FL and PI controller based ESM systems for supporting the pulsed load. Figure 5.38 and Figure 5.39 show the voltage, current and SOC of the battery and supercapacitor, respectively, for the FL and PI controller based ESM systems for the discharging period, t=1s to t=2s. These figures show that during t=1s to t=2s, the voltages of the battery and supercapacitor go down, output currents increase and the SOC decrease for discharging power to the MVDC system.

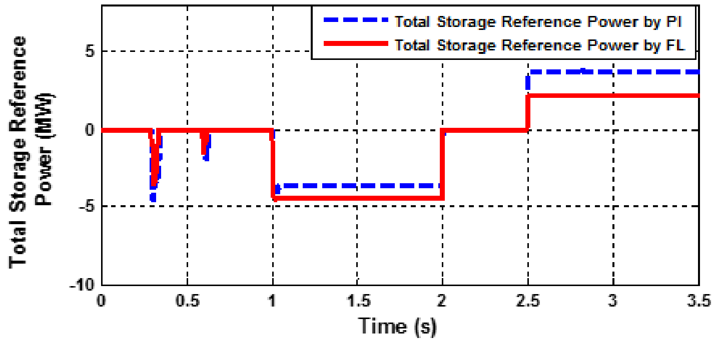

(a) Total storage reference power.

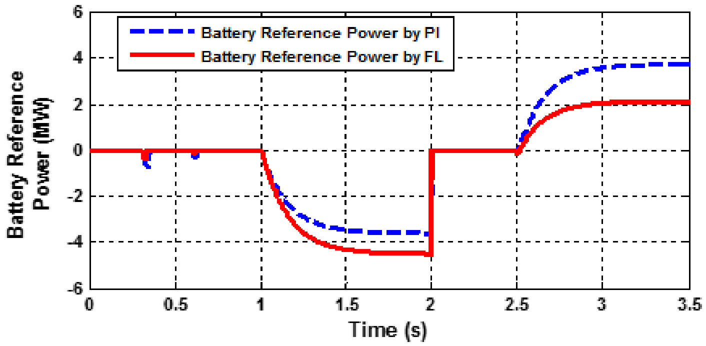

(b) Battery reference power.

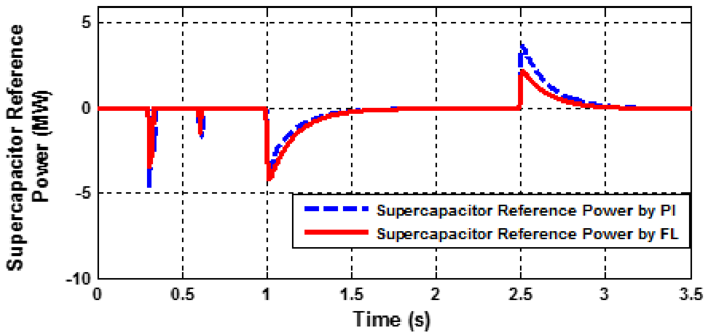

(c) Supercapacitor reference power

Figure 5.36: Reference power produced by the FL and PI controller based ESM systems (case 1).

For the 4MW power mismatch at t=1s, the PI controller provides nearly 4MW negative $P_{stor-ref}$ for discharging (Figure 5.36). But the FL controller provides nearly 4.5MW negative $P_{stor-ref}$ for

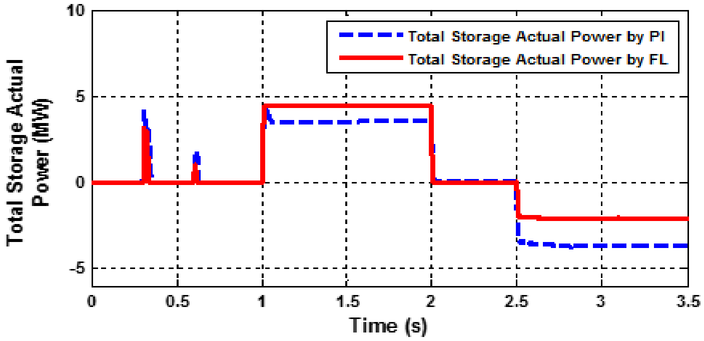

(a) Total storage actual power.

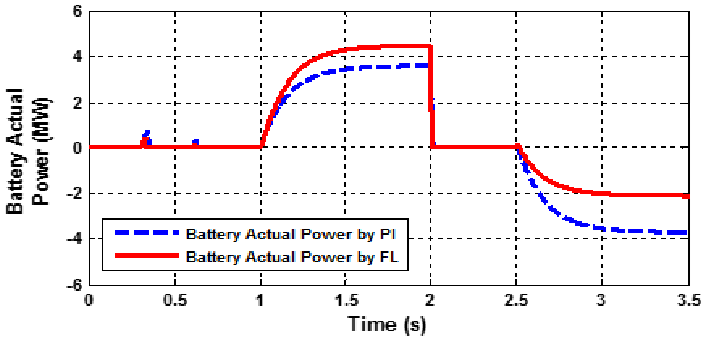

(b) Battery actual power.

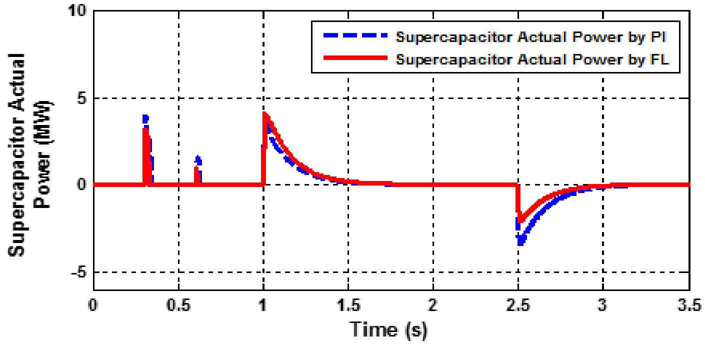

(c) Supercapacitor actual power

Figure 5.37: Actual power response of the battery and supercapacitor with the FL and PI controller based ESM systems (case 1).

discharging (Figure 5.36). The PI controller determines the $P_{stor-ref}$ depending on the conditions of the total generated power (P_{gen}), total load power demand (P_{load}), measured bus voltage (V_{Bus})

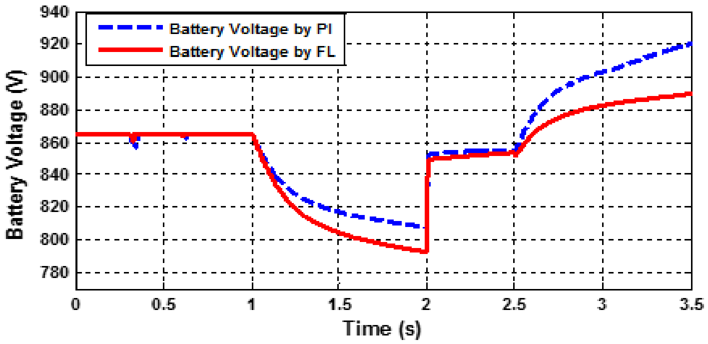

(a) Battery voltage response.

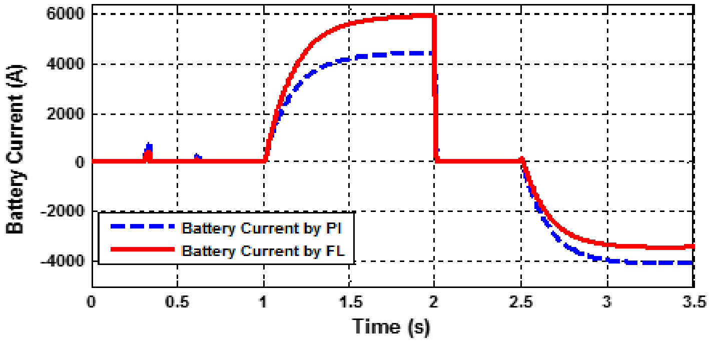

(b) Battery current response.

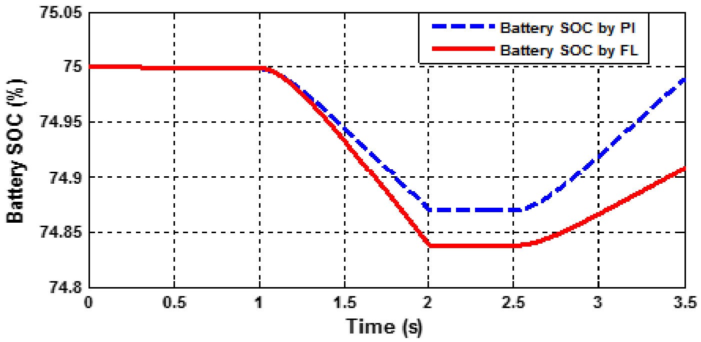

(c) Battery SOC.

Figure 5.38: The voltage, current and SOC of the battery with the FL and PI controller based ESM systems for (case 1).

and reference bus voltage (V_{DC-ref}). On the other hand, the FL controller considers additionally the SOC of the battery and supercapacitor (SOC_{Bat}, SOC_{SC}). In this case, the SOC of the battery and supercapacitor are nearly high (75%, 82.65%), which means that the battery and supercapacitor have good amount of energy stored to discharge. So, considering the SOC of the battery and supercapacitor with the total load and bus voltage, the FL controller provides nearly -4.5MW as $P_{stor-ref}$ for discharging instead of providing -4MW reference power for discharging. Now the total available power is 44.5MW, but total load is 44MW. At this situation, generators will reduce their power supply by 0.5MW automatically by controlling their gas turbine based governor systems. However, if desired, the FL controller can be adjusted in such a way that generation output can be left to its maximum value.

From t=2s to t=2.5s, the total load remains at 40MW. At t=2.5s, a 4MW load is rejected from the MVDC system. This causes the bus voltage to increase and a decrease in total current as shown in Figure 5.35. Figure 5.36 shows, the FL and PI controllers provide positive $P_{stor-ref}$ for charging, during that period. Figure 5.37 shows the actual power consumed by the battery and supercapacitor from the MVDC system for the FL and PI controller based ESM systems. In this case, powers are negative because the battery and supercapacitor work in the charging mode, during t=2.5s to t=3.5s. Figure 5.38 and Figure 5.39 show that during the period of t=2.5s to t=3.5s, voltages of the battery and supercapacitor go up, the SOC increases and the currents go to negative because the battery and supercapacitor work in the charging mode.

For the rejection of 4MW load from the MVDC system at t=2.5s, the PI controller provides nearly 4MW reference power for charging but the FL controller generates nearly 2MW reference power. This is because the FL controller generates reference power by considering the SOC of the battery and supercapacitor (SOC_{Bat}, SOC_{SC}) with the other two input variables, ΔI and V_{Bus}. As the SOC of the battery and supercapacitor are high, they do not need to be charged quickly. On the other hand, the PI controller's reference power generation does not depend on the SOC of the battery and supercapacitor.

Case 2: Comparison of performances of the FL and PI controller based ESM systems at low SOC: In this case, the SOC of the battery is set at 20% as the initial SOC and the supercapacitor's initial voltage is kept 170V with SOC of 25.2%.

At t=0.3s and t=0.6s, 34MW and 6MW load are connected to the MVDC system, respectively. Again at t=1s, 4MW pulsed load is added to the MVDC system and it is continued until t=2s. With the addition of pulsed load, the total load (44MW) goes higher than the total generation

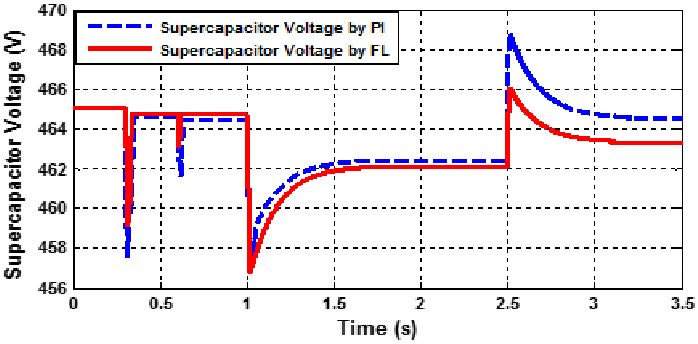

(a) Supercapacitor voltage response.

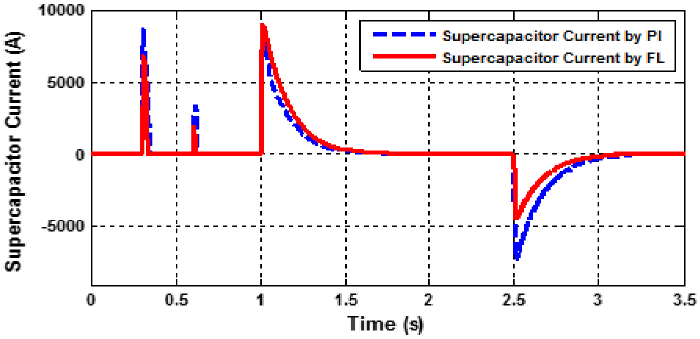

(b) Supercapacitor current response.

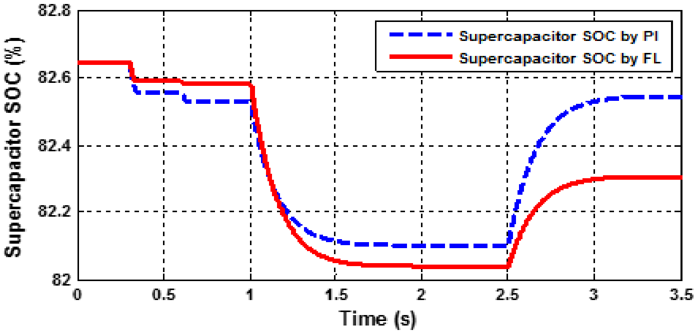

(c) Supercapacitor SOC.

Figure 5.39: The voltage, current and SOC of the supercapacitor with the FL and PI controller based ESM systems (case 1).

capacity (40MW). Both the FL controller and PI controller based ESM systems are expected to provide the negative $P_{stor-ref}$ for discharging. As the overcharging and deep discharging protection

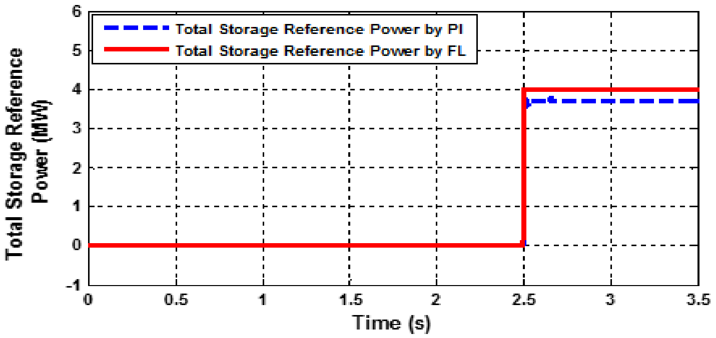

Figure 5.40: Total storage reference power produced by the FL and PI controller based ESM systems (case 2).

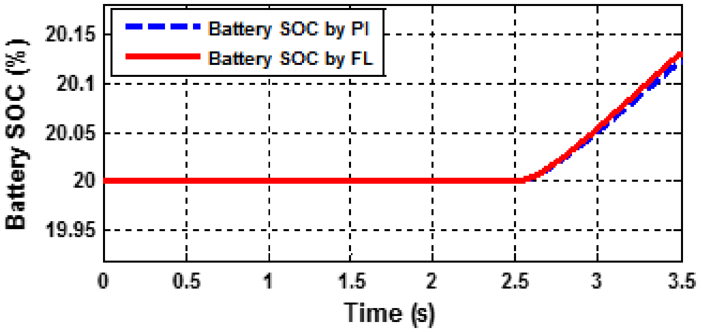

(a) Battery SOC.

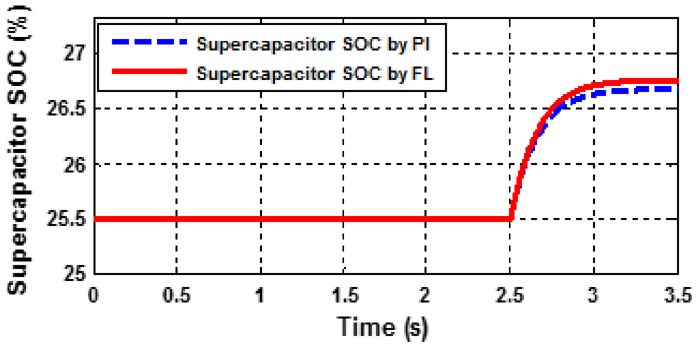

(b) Supercapacitor SOC.

Figure 5.41: SOC of the battery and supercapacitor with the FL and PI controller based ESM systems (case 2).

controller is connected to the PI controller based ESM system, Figure 5.40 shows that the $P_{stor-ref}$ for discharging is zero. Because of low SOC (20% and 25.2%) of the battery and supercapacitor (Figure 5.41), the charge controller blocks the PI controller's negative $P_{stor-ref}$ signal. For the FL controller based ESM systems, the reference power generation depends also on the SOC of the battery and supercapacitor (SOC_{Bat}, SOC_{SC}) with the other two input variables, ΔI and V_{Bus}. Figure 5.41 shows that due to low SOC (20% and 25.2%) , the FL controller also provides zero reference power (Figure 5.40). Simulation results after t=2s for the FL and PI controller based ESM systems are the same as shown earlier subsection 5.4.2, where at t=2.5s, the battery and supercapacitor start charging and continue until t=3.5s.

In this case, for the rejection of 4MW load from the MVDC system at t=2.5s, the PI controller based ESM system provides nearly 4MW reference power for charging (Figure 5.40). For the same condition, the FL controller based ESM system generates 5MW reference power for charging but the available power limit is applied which changed to 4MW. As the SOC of the battery and supercapacitor are very low (20%, 25.2%), they need to be charged quickly. Considering these issues, the FL controller based ESM system generates 5MW reference power for charging instead of 4MW reference power generation. But due to generator power limit, the generation limit checking controller adjusted the $P_{stor-ref}$ to 4MW.

Case 3: Comparison of performances of the FL and PI controller based ESM systems at high SOC: In this case, the SOC of the battery is set at 94% as the initial SOC and the supercapacitor's initial voltage is kept 535V with SOC of 97.02%.

From Figure 5.42, the simulation results up to t=2s for the FL and PI controller based ESM systems are same as shown earlier in subsection 5.4.1, where as at t=0.3s, t=0.6s and t=1s to t=2s, the battery and supercapacitor supply power to the MVDC system. At t=2.5s, 4MW load is rejected, and both the FL and PI controller based ESM system are expected to provide the positive $P_{stor-ref}$ for charging. As the overcharging and deep discharging protection controller is connected to the PI controller based ESM system, Figure 5.42 shows that the $P_{stor-ref}$ for charging is zero. Because of high SOC (nearly 94% and 97.02%) of the battery and supercapacitor (Figure 5.43), the charge controller blocks the PI controller. For the FL controller based ESM system, the reference power generation depends also on the SOC of the battery and supercapacitor. Figure 5.43 shows that due to the high SOC (nearly 94% and 97.02%) of the battery and supercapacitor, Figure 5.42 shows that the FL controller also provides zero reference power.

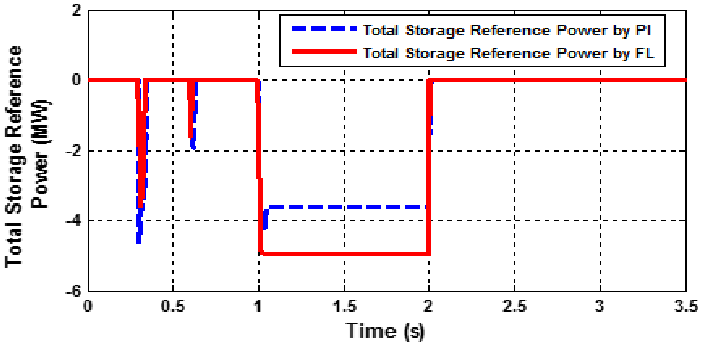

Figure 5.42: Reference power produced by the FL and PI controller based ESM systems (case 3).

In this case, for the 4MW power mismatch at t=1s, the PI controller based ESM system provides nearly 4MW negative $P_{stor-ref}$ for discharging (Figure 5.42). But the FL controller provides nearly 5MW negative $P_{stor-ref}$ for discharging (Figure 5.42). In this case, the SOC of the battery and supercapacitor are very high (94%, 97.02%) which means that the battery and supercapacitor have good amount of energy to discharge. So, considering the SOC of the battery and supercapacitor with the other two input variables, ΔI and V_{Bus}, the FL controller based ESM system provides nearly -5MW as $P_{stor-ref}$ for discharging instead of providing -4MW for discharging. At this situation, generators will reduce their power supply by 1MW automatically by controlling their gas turbine based governor systems. But the PI controller based ESM system provides nearly -4MW reference power for charging as it does not consider SOC_{Bat} and SOC_{SC} for the generation of $P_{stor-ref}$.

5.5 FL vs PI Controller Based ESM Systems

As evident from the previous discussion, FL controller based ESM strategy has some advantages over the PI controller based ESM strategy. The main advantage is that the FL controller based ESM system does not need additional deep discharging and overcharging protection controller. As shown in Figure 4.7, the total storage reference power ($P_{stor-ref}$) generated by the FL controller depends

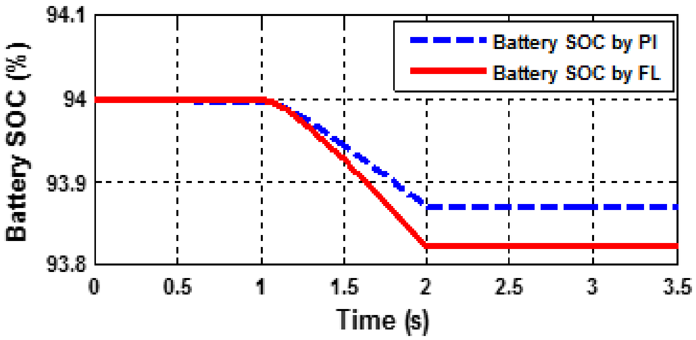

(a) Battery SOC.

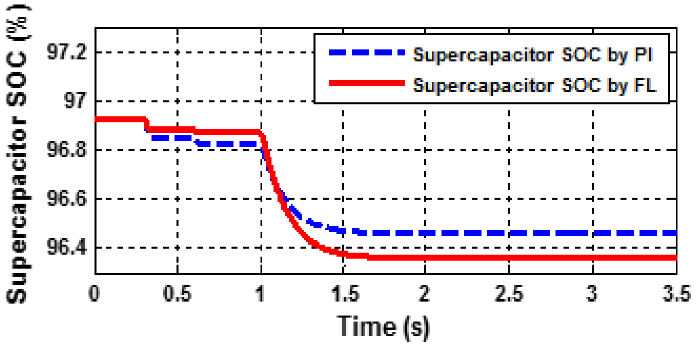

(b) Supercapacitor SOC.

Figure 5.43: SOC of the battery and supercapacitor with the FL and PI controller based ESM systems (case 3).

on the difference between the total supplied current and the total load current (ΔI), bus voltage (V_{Bus}), SOC of the battery (SOC_{Bat}), and supercapacitor (SOC_{SC}). The fuzzy rules are shown in Table 4.1. From the Table 4.1, it is shown that if the SOC of the battery and supercapacitor are low than the total storage reference power ($P_{stor-ref}$) for discharging should be zero, and if the SOC of the battery and supercapacitor are high than the total storage reference power ($P_{stor-ref}$) for charging should be also zero. So, there is no need for extra overcharging and deep discharging protection controller.

On the other hand, as shown in Figure 4.8, the total storage reference power ($P_{stor-ref}$) generation by the PI controller based ESM system depends on the difference of the total load (P_{load}) and the total generated power (P_{gen}), and the difference of the reference bus voltage (V_{DC-ref}) and the

Table 5.3: Comparison of FL and PI Controller Based ESM Systems

FL controller based ESM System	**PI controller based ESM System**
FL based ESM system does not need additional deep discharging and overcharging protection controller.	PI based ESM system needs additional deep discharging and overcharging protection controller.
In FL based ESM system, total storage reference power ($P_{stor-ref}$) is dependent on SOC_{Bat} and SOC_{SC} with other two input variables (V_{Bus}, ΔI).	In PI based ESM system, total storage reference power ($P_{stor-ref}$) is not dependent on SOC_{Bat} and SOC_{SC}. It depends on only the two input variables (power and voltage).
FL based ESM system can change $P_{stor-ref}$ with the change of SOC_{Bat} and SOC_{SC}.	PI based ESM system cannot change $P_{stor-ref}$ with the change of SOC_{Bat} and SOC_{SC}.
FL based ESM system helps for fast charging and discharging.	PI based ESM system does not help for fast charging and discharging.

measured bus voltage (V_{Bus}). The total storage reference power ($P_{stor-ref}$) generation by the PI controller based ESM system does not consider the SOC of the battery and supercapacitor. If the PI controller based ESM system generates $P_{stor-ref}$ depending on the power mismatch and the bus voltage change, and if the SOC of the battery and supercapacitor are low or high then there are possibilities of deep discharging or overcharging. Overcharging and deep discharging reduce the life time of the energy storage and decrease efficiency. So, the PI controller based ESM strategy needs extra overcharging and deep discharging protection controller as shown in Figure 4.9.

The overcharging and deep discharging controller of the PI controller based ESM system blocks the total storage reference power ($P_{stor-ref}$) when the SOC of the battery and supercapacitor cross the upper (90%) and lower (30%) limit. It has no impact on determining the $P_{stor-ref}$. But the reference power generation by the FL controller based ESM system depends on all the four input variables (ΔI, V_{Bus}, SOC_{Bat}, SOC_{SC}). The SOC of the battery and supercapacitor (SOC_{Bat}, SOC_{SC}) have direct impact on determining the total storage reference power ($P_{stor-ref}$). If the battery and supercapacitor are nearly at fully charged, the FL controller based ESM system generates high reference power for discharging and low reference power for charging. It does opposite when the SOC of the battery and supercapacitor are low. If the SOC of the battery and supercapacitor are nearly low, the FL controller based ESM system will generate low reference power for discharging and high reference power for charging. The comparison of FL and PI controller based ESM system are summarized in Table 5.3.

5.6 Power Sharing by FL and SOC Based Strategies

To show the power sharing between two batteries and two supercapacitors, the SOC of the batteries are set randomly as 86% and 54% as the initial SOC and the supercapacitors initial voltage are kept 430V and 495V with SOC of 75.55% and 88.75%, respectively. The system is subjected to the same test situations as described in the previous case 5.4.1.

5.6.1 FL Based Power Sharing

At t=0.3s, t=0.6s and t=1s to t=2s, the FL controller provides the negative $P_{stor-ref}$ for discharging (Figure 5.44). The LPF separates the $P_{stor-ref}$ into $P_{Bat-ref}$ and P_{SC-ref}. The FL based power sharing controller separates the $P_{Bat-ref}$ into $P_{Bat-1-ref}$, $P_{Bat-2-ref}$ and P_{SC-ref} into $P_{SC-1-ref}$, $P_{SC-2-ref}$ (Figure 5.45). As the SOC of the battery-1 is higher than the SOC of the battery-2, the FL based power sharing controller allocates the big part of $P_{Bat-ref}$ as $P_{Bat-1-ref}$ and small part as $P_{Bat-2-ref}$ for discharging (Figure 5.45a). For supercapacitors, the SOC of the supercapacitor-1 is lower than the SOC of the supercapacitor-2. The SOC based power sharing controller allocates the small part of P_{SC-ref} as $P_{SC-1-ref}$ and big part as $P_{SC-2-ref}$ for discharging (Figure 5.45b). At t=2.5s, 4MW load is rejected and the FL controller provides positive $P_{stor-ref}$ for charging of the batteries and supercapacitors (Figure 5.44). From Figure 5.44, the LPF separates the $P_{stor-ref}$ into $P_{Bat-ref}$ and P_{SC-ref}. As the SOC of the battery-1 is higher than the SOC of the battery-2, the FL based power sharing controller allocates the small part of $P_{Bat-ref}$ as $P_{Bat-1-ref}$ and a big part as $P_{Bat-2-ref}$ for charging of the batteries (Figure 5.45a). For supercapacitors, the SOC of the supercapacitor-1 is lower than the SOC of the supercapacitor-2. The FL based power sharing controller allocates the major part of P_{SC-ref} as $P_{SC-1-ref}$ and small part as $P_{SC-2-ref}$ (Figure 5.45b) for charging of the supercapacitors.

5.6.2 SOC Based Power Sharing

At t=0.3s, t=0.6s and t=1s to t=2s, the PI controller provides the negative $P_{stor-ref}$ for discharging (Figure 5.46). From Figure 5.46, the LPF separates the $P_{stor-ref}$ into $P_{Bat-ref}$ and P_{SC-ref}. The SOC based power sharing controller separates the $P_{Bat-ref}$ into $P_{Bat-1-ref}$, $P_{Bat-2-ref}$ and P_{SC-ref} into $P_{SC-1-ref}$, $P_{SC-2-ref}$ (Figure 5.47a and Figure 5.47b). As the SOC of the battery-1 is higher than the SOC of the battery-2, the SOC based power sharing controller allocates the big part of $P_{Bat-ref}$ as $P_{Bat-1-ref}$ and small part as $P_{Bat-2-ref}$ for discharging

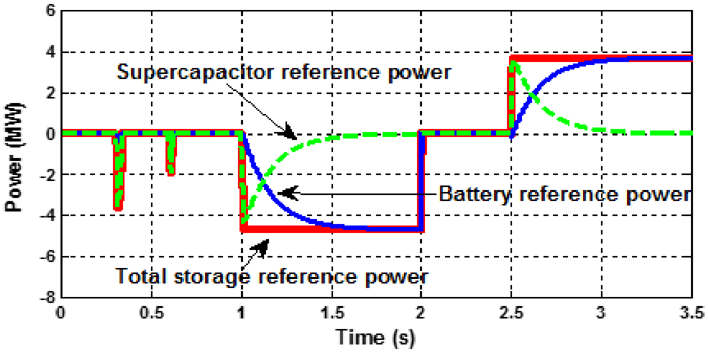

Figure 5.44: Reference power produced by the FL controller based ESM system.

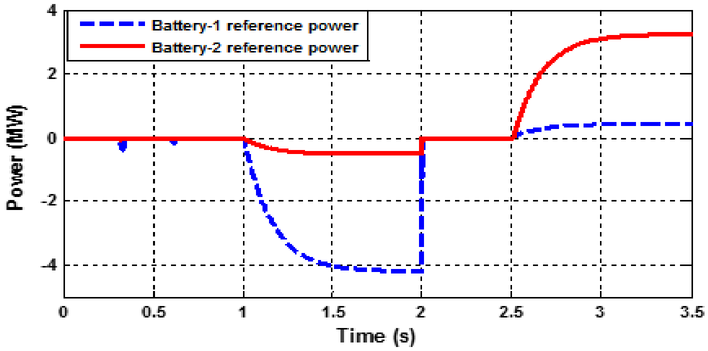

(a) Reference power of the batteries.

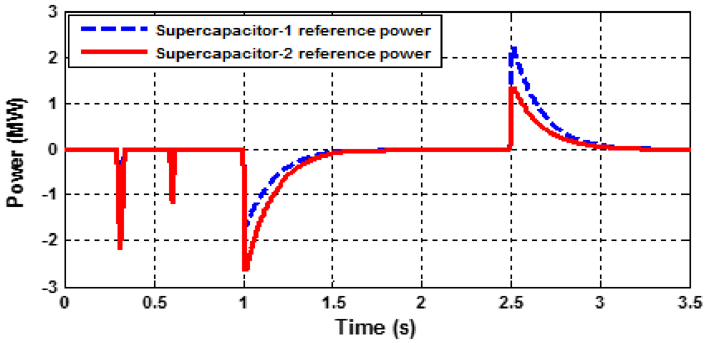

(b) Reference power of the supercapacitors.

Figure 5.45: Reference power of the batteries and supercapacitors produced by the FL based power sharing controller.

(Figure 5.47a). For supercapacitors, the SOC of the supercapacitor-1 is lower than the SOC of the supercapacitor-2. The SOC based power sharing controller allocates the small part of P_{SC-ref} as $P_{SC-1-ref}$ and a big part as $P_{SC-2-ref}$ for discharging (Figure 5.47b). At t=2.5s, 4MW load is rejected and the PI controller provides the positive $P_{stor-ref}$ for charging of the batteries and supercapacitors (Figure 5.46). The LPF separates the $P_{stor-ref}$ into $P_{Bat-ref}$ and P_{SC-ref} (Figure 5.46). As the SOC of the battery-1 is higher than the SOC of the battery-2, the SOC based power sharing controller allocates the small part of $P_{Bat-ref}$ as $P_{Bat-1-ref}$ and big part as $P_{Bat-2-ref}$ for charging of the batteries (Figure 5.47a). For supercapacitors, the SOC of the supercapacitor-1 is lower than the SOC of the supercapacitor-2. The SOC based power sharing controller allocates the big part of P_{SC-ref} as $P_{SC-1-ref}$ and small part as $P_{SC-2-ref}$ for charging of the supercapacitors (Figure 5.47b).

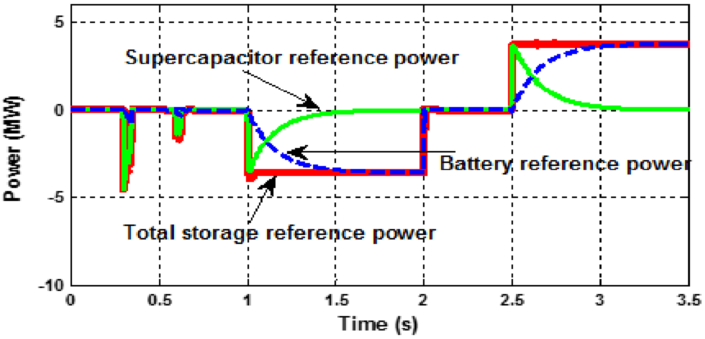

Figure 5.46: Reference power produced by the PI controller based ESM system.

5.7 Controller Hardware-in-the-Loop (CHIL) Based Experimental Results

5.7.1 Introduction of CHIL Environment

RT-LAB Real-Time Simulator: For real-time simulation of MVDC power system, RT-LAB real-time simulator is used. MATLAB/Simulink platform is used for drawing, editing block diagram of the model of the system [89]. The block-diagram is used to generate C code which is downloaded onto Target computer (real-time simulator) for real-time simulation. To connect the real-time simulator with external hardware devices, controllers, physical plants, inputs, and

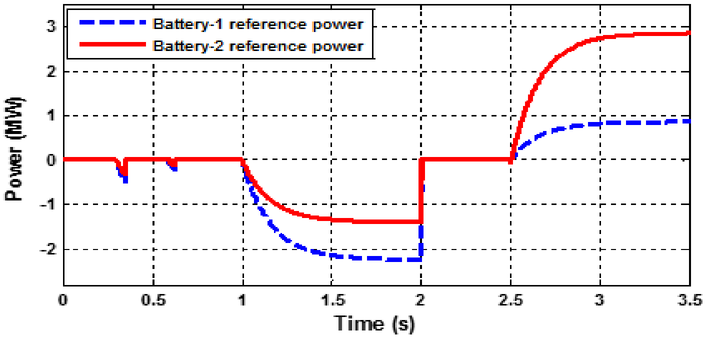

(a) Reference power of the batteries.

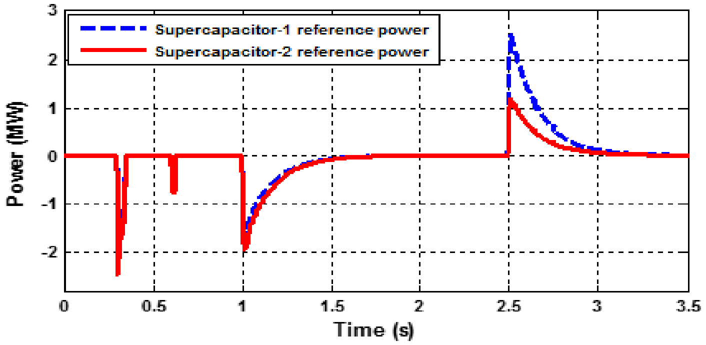

(b) Reference power of the supercapacitors.

Figure 5.47: Reference power of the batteries and supercapacitors produced by the SOC based power sharing controller.

outputs (I/O) interfacings are required. Signals can be passed easily as inputs and outputs by using I/O blocks from the library of RT-LAB. RT-LAB automatically generates model code and I/O drivers. The Target computer (real-time simulator) uses TCP/IP network for communication between Target computer and Host computer. The Target computer can be connected to more than one Host computer but only a single Host computer has the full control of the simulator. The Target real-time simulator computer uses REDHAT real-time operating system. The Simulink SimPowerSystems use fixed-time-step solver based on the Tustin method but it is not suitable for real-time simulation for some limitations. It has limitations with iterative calculations to solve algebraic loops, dynamic computation of circuit matrices, un-damped switching oscillation, and the slowdown of simulation speed with the very small time step size. To overcome the limitations of SimPowerSystems solver, RT-LAB uses advanced fixed time-step solvers and computational techniques designed for the real-time simulation which is known as ARTHEMIS [89].

OP7020: The OP7020 is a Virtex-7 FPGA process and expansion unit which is designed to be used with Opal-RT real-time multi-core computer to simulate complex power electronics circuits and to develop control systems. It incorporates the FPGA technology in RT-LAB simulation. It operates at 100MHz. It can support 16 high-speed fiber optic links using Small Form-factor Pluggable (SFP) transceivers for high-speed communication with other OPAL-RT simulators, such as the OP7000, OP5607 and users external controllers. Where the maximum signaling rate is 5Gbps with Aurora, Gigabit Ethernet or customer requirements based protocols. It also supports high speed (30Gbps) PCI Express X4 links to interface with an OPAL-RT real-time multi-core simulator which helps for simulation of large AC-DC grids [90].

OP5607: The OP5607 is a Xilinx Virtex-7 FPGA which can be interfaced with an OPAL-RT real-time multi-core simulator. It helps to incorporate FPGA technology to RT-LAB simulation with high-speed, high-density analog/digital I/O. It has additional I/O (input/output) expansion unit which actually acts as additional inputs and outputs ports for Opal-RT simulator. It has 8 signal conditioning and analog/digital converter modules with 16 analog and 32 digital channels. Which eventually supports 128 fast analog and 256 digital signals. It can accommodate 16 SFP multi-mode fiber optic modules for high sped communications (speed from 1 to 5Gbps) with other FPGA devices (OP7020, OP4500, OP7020) and external controllers. It maintains the Aurora, Gigabit Ethernet or customer requirements based protocols. It has additional mini-BNC terminals for monitoring signals through oscilloscope. It can accommodate high speed PCI Express Gen2*4 for connection to real-time multi-time computer [91]. It enables update rates of 100MHz which is capable to generate digital events for high-precision switching.

5.7.2 CHIL Simulation Setup

The block diagram for CHIL simulation setup is shown in Figure 5.48. The Host computer is Intel core i7, 3.2GHz processor. The Host computer is used to prepare the model for real-time simulation in Target computer. It can show the real-time simulation results from Target computer. It is connected to the Target-real time simulator via Ethernet cable. All the loads, sources, battery and supercapacitor are modeled in four different subsystems and run on 4 cores of the simulator

CPU. The FL based ESM system controller is implemented in FPGA-OP7020. The FPGA board-OP5706 is used to produce analog output signals. FPGA-7020 and FPGA-5607 are connected to the Target computer via PCIe cable.

The Xilinx System Generator (XSG) library provided by RT-LAB is used to model the controller in FPGA-OP7020. RT-XSG library is also used to model analog outputs in FPGA-OP5607. The RT-XSG is capable of compiling the model and generates VHDL (VHSIC Hardware Description Language) code and FPGA bit streams. The FPGA bit stream files are loaded in OP5607, OP7020.

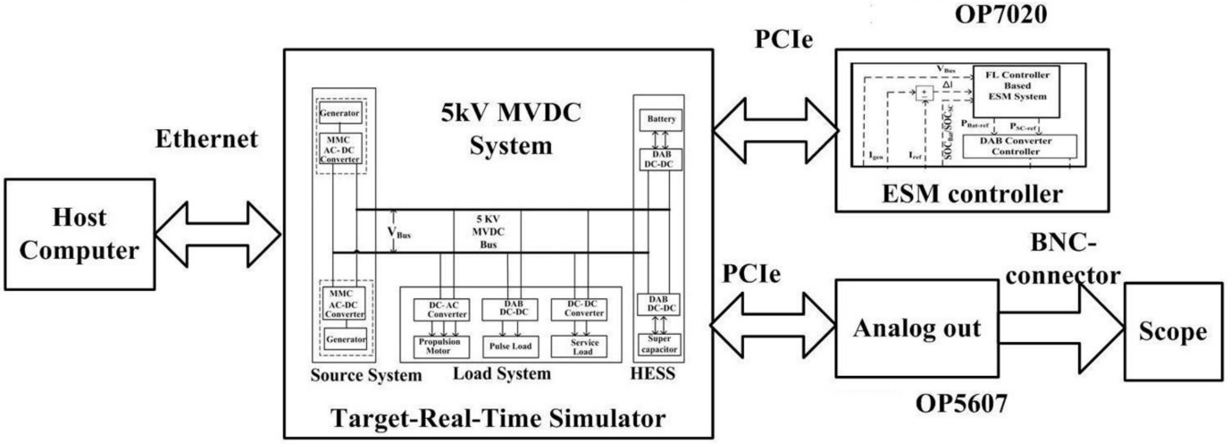

Figure 5.48: Block diagram of hardware setup for CHIL simulation of FL based ESM system.

Figure 5.49 shows the experimental setup. In the front panel (Figure 5.49a), the top FPGA board is OP7020 where the ESM controller is implemented. The bottom FPGA board is OP5607 and it is used to show the analog output results in the scope. The black audio cable is for synchronization between two FPGAs (OP5607 and OP7020). The top FPGA board (OP7020) works as master and bottom FPGA board works as slave. The white cable is RJ45 connector which connects analog/digital ports to quick monitoring ports. BNC connectors are used to connect quick monitoring ports to the oscilloscope. In the back panel (5.49b), the orange cables are PCI express (PCIe) cables which connect both FPGAs (OP5607, OP7020) to the Target computer system. FPGA boards (OP5607, OP71020) transfer signals to the modeled electrical subsystems in real-time simulator through the PCIe cables.

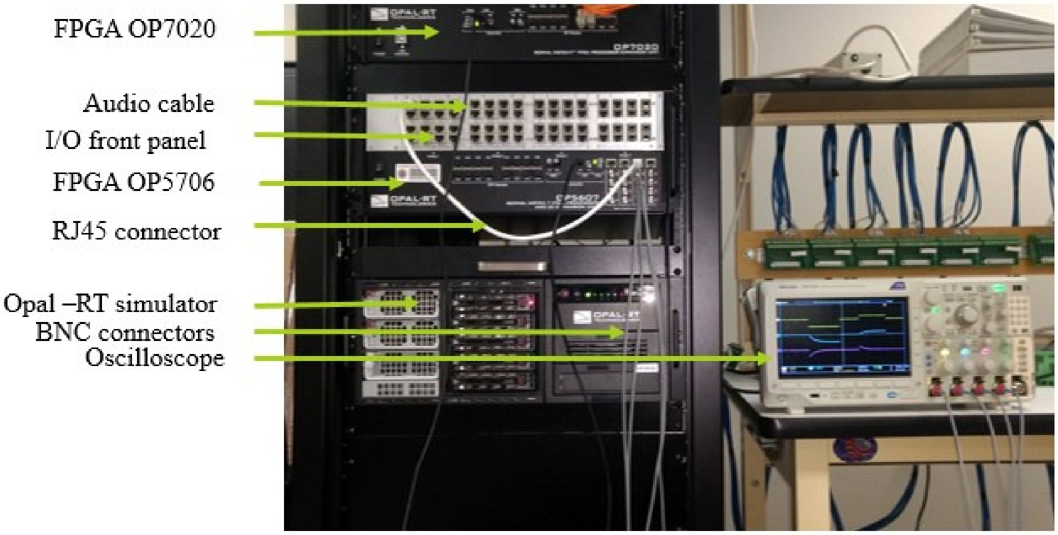

(a) Front panel.

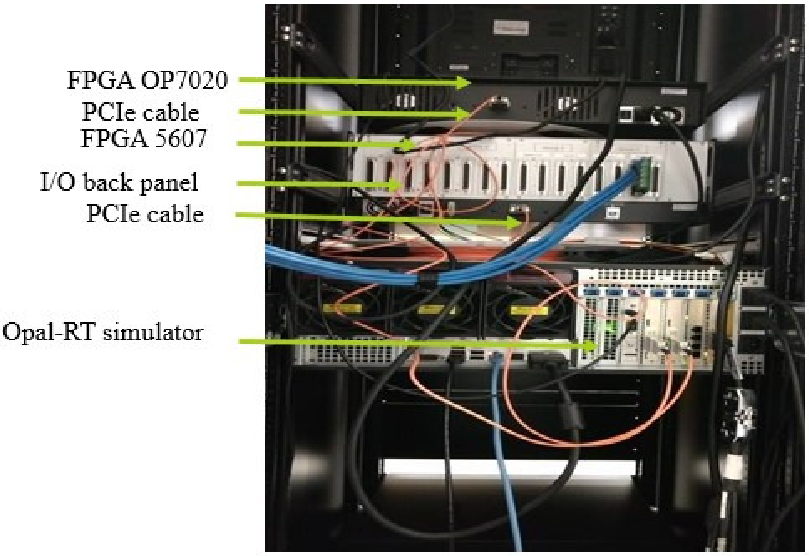

(b) Back panel.

Figure 5.49: Experimental setup for CHIL operation of FL based ESM system.

5.7.3 CHIL vs Off-line Results

To show the experimental results of the FL controller and LPF based ESM systems, the three cases of section 5.2 are performed. Here, Off-line and CHIL results are shown together for comparison purpose.

Case 1: Performances of the FL Controller and LPF Based ESM System when the SOC of HESS within the Limit: For this case, the SOC of the battery and supercapacitor are set at 75% and 82.65%. The simulation steps are the same as described in case 1 of section 5.2 of chapter 5. At t=0.3s and t=0.6s, 34MW and 6MW load are connected to the MVDC system, respectively. Figure 5.50 shows the MVDC bus voltage and total load current (Off-line and CHIL). The addition of loads are transient operations and FL controller based ESM system provides negative $P_{stor-ref}$ for discharging (Figure 5.51). Figure 5.51 shows also LPF separates $P_{stor-ref}$ between $P_{Bat-ref}$ and P_{SC-ref}. Again, at t=1s, 4MW pulsed load is added to the MVDC system and it is continued for t=1s. With this operation, total power demand exceeds the total generation capacity and the FL controller based ESM system provides nearly -4.5MW as $P_{stor-ref}$ for discharging (Figure 5.51). Figure 5.52 shows the actual power response of the battery and supercapacitor. At t=2.5s, 4MW load is rejected and the FL controller based ESM system provides positive $P_{stor-ref}$ for charging (Figure 5.51). Figure 5.52 shows the actual power consumed by the HESS. From the figures (Figure 5.50, Figure 5.51, and Figure 5.52) it is clear that the Off-line and CHIL results are same.

Case 2: Performances of the FL Controller and LPF based ESM System at Low SOC of HESS: To show the performances of the FL controller and LPF based ESM system with the situation of low SOC, the SOC of the battery is set 20% as the initial SOC and the supercapacitor's initial voltage is kept 170V with SOC of 25.5%. In this case, the simulation steps are the same as described in case 2 of section 5.2 of chapter 5.

At t=0.3s and t=0.6s, 34MW and 6MW load are connected to the MVDC system, respectively. Pulsed load is added at t=1s until t=2s. Considering those operations, the FL controller based ESM system is expected to provide negative $P_{stor-ref}$ for discharging. But due to low SOC of battery and supercapaictor (20% and 25.5%), Figure 5.53 shows that the FL controller based ESM system provides zero $P_{stor-ref}$ for discharging. Similar to case 1, at t=2.5s, 4MW load rejected and Figure 5.53 shows that the ESM system provides positive $P_{stor-ref}$ for charging. From the Figure 5.53, the Off-line and CHIL results are same.

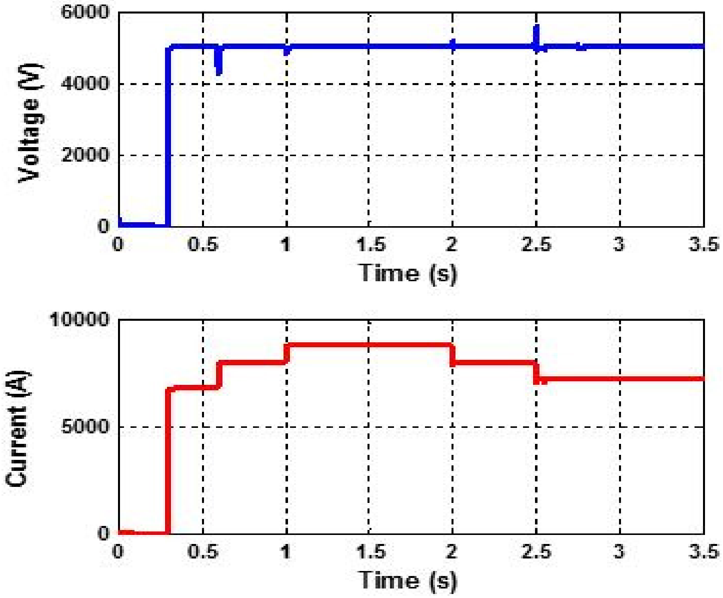

(a) Off-line simulation results.

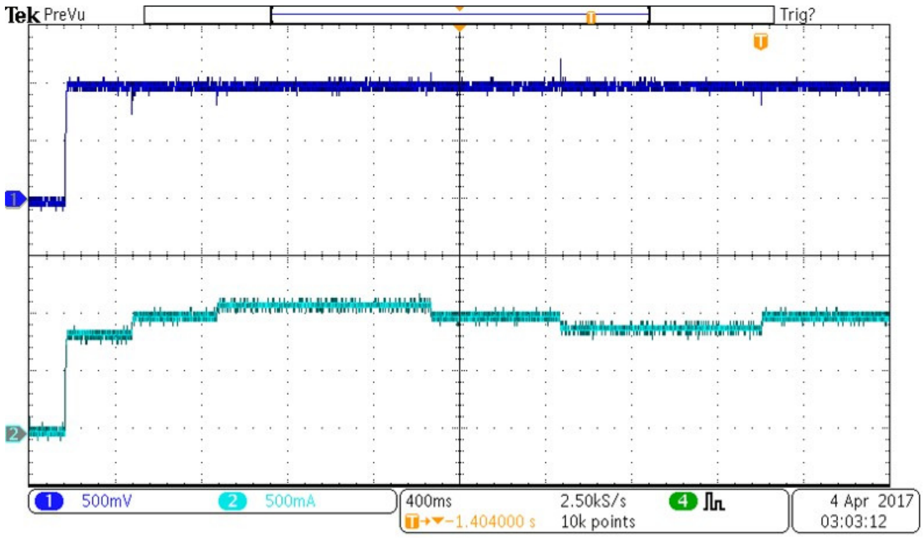

(b) CHIL results-oscilloscope plots: Ch1: MVDC bus voltage and Ch2: total load current (Ch1: 2.5kV/div, Ch2: 4000A/div).

Figure 5.50: MVDC bus voltage and total load current (case 1).

Case 3: Performances of the FL Controller and LPF based ESM System at High SOC of HESS: To show the performances of the FL controller and LPF based ESM system with the situation of high SOC, the SOC of the battery is set 94% as the initial SOC and the supercapacitor's initial voltage is kept 535V with SOC of 97.02%. In this case, the simulation steps are the same as described in case 3 of section 5.2 of chapter 5.

In this case, at t=0.3s, t=0.6s, t=1s to t=2s, 34MW, 6MW and 4MW pulsed load are connected to MVDC system. Considering those operations, the FL controller based ESM system provides negative $P_{stor-ref}$ for discharging (Figure 5.54). At t=2.5s, 4MW load is rejected and for charging the FL controller based ESM system should provide positive $P_{stor-ref}$. But the SOC of the battery and supercapacitor are high (94%, 97.02%). To avoid overcharging, Figure 5.54 shows that the FL controller based ESM system provide zero $P_{stor-ref}$ instead of positive $P_{stor-ref}$. From the Figure 5.54, the Off-line and CHIL results are same.

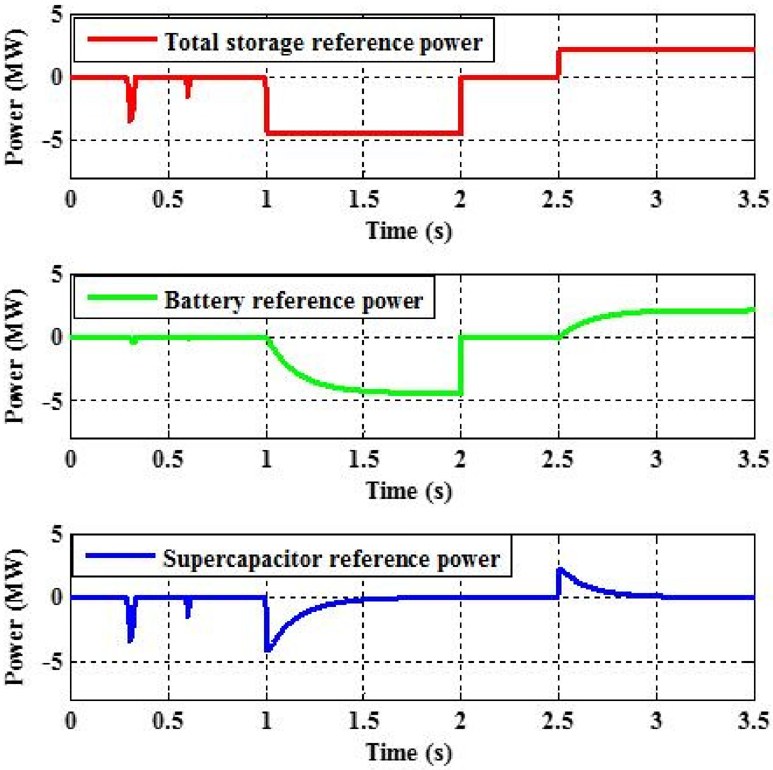

(a) Off-line simulation results.

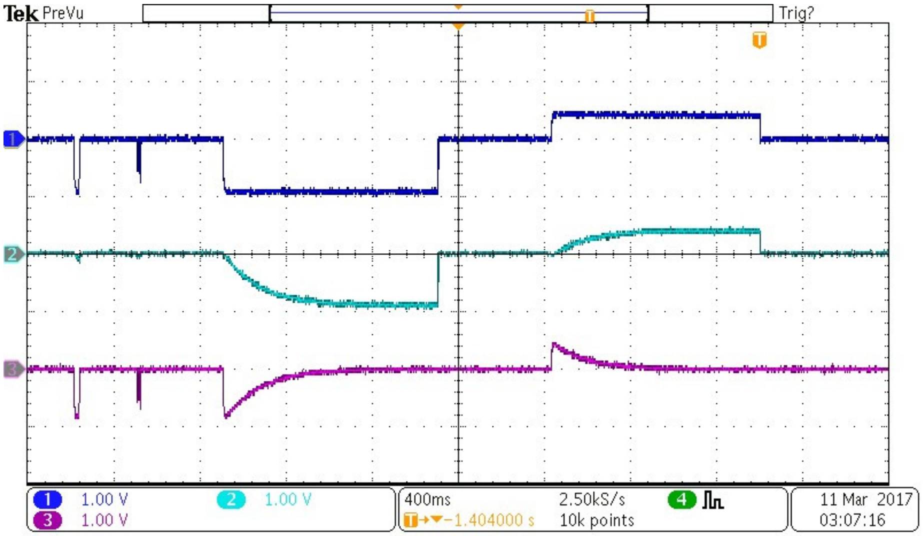

(b) CHIL results-oscilloscope plots: Ch1: total storage reference power, Ch2: battery reference power, Ch3: supercapacitor reference power (Ch1, Ch2, Ch3 = 5MW/div).

Figure 5.51: Reference power produced by FL controller and LPF based ESM system (case 1).

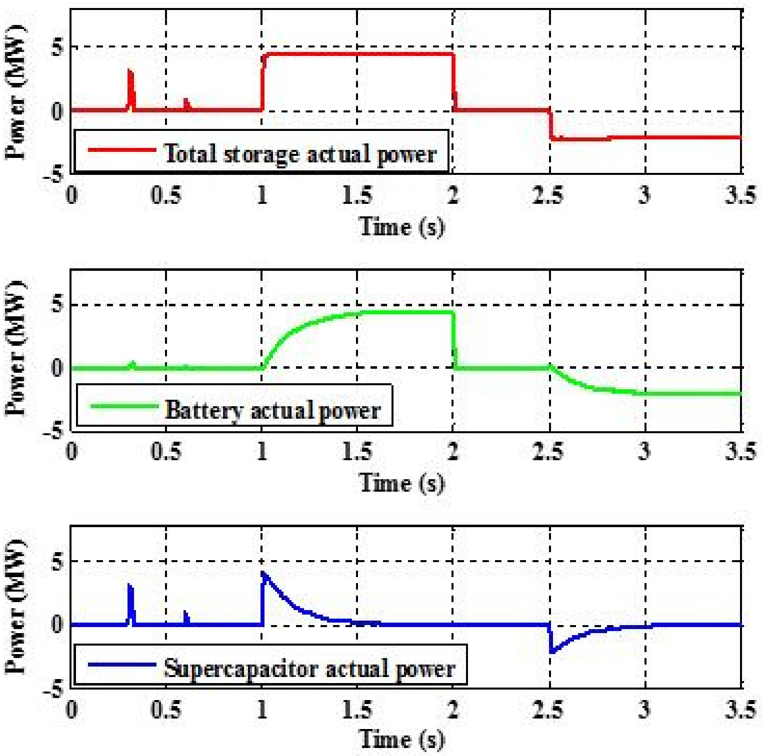

(a) Off-line simulation results.

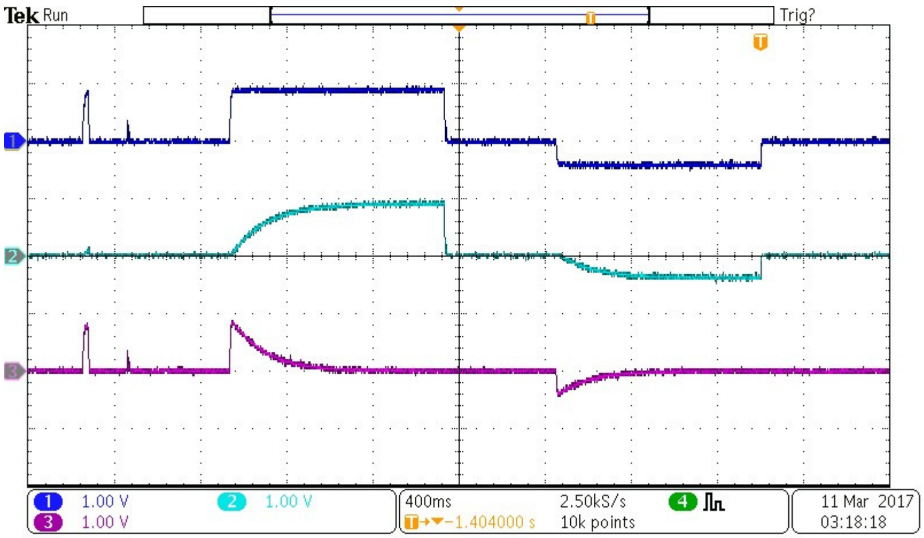

(b) CHIL results-oscilloscope plots: Ch1: total storage actual power, Ch2: battery actual power, Ch3: supercapacitor actual power (Ch1, Ch2, Ch3 = 5MW/div).

Figure 5.52: Actual power response of the HESS (case 1).

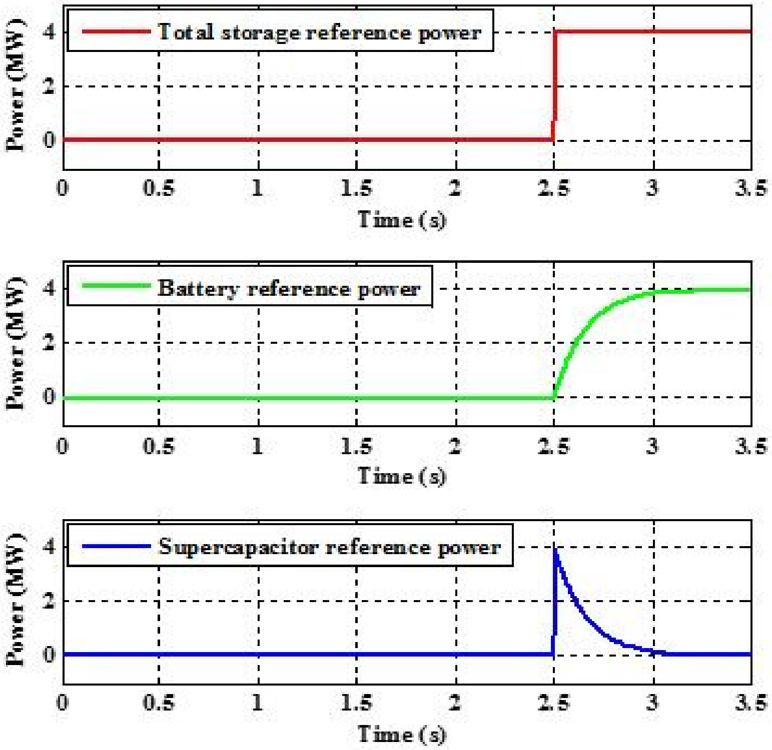

(a) Off-line simulation results.

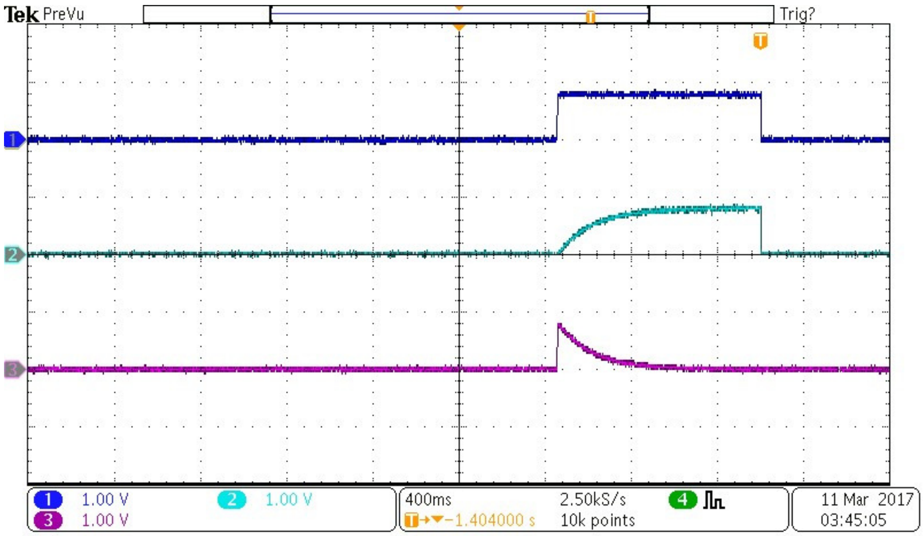

(b) CHIL results-oscilloscope plots: Ch1: total storage reference power, Ch2: battery reference power, Ch3: supercapacitor reference power (Ch1, Ch2, Ch3 = 5MW/div).

Figure 5.53: Reference power produced by FL controller and LPF based ESM system (case 2).

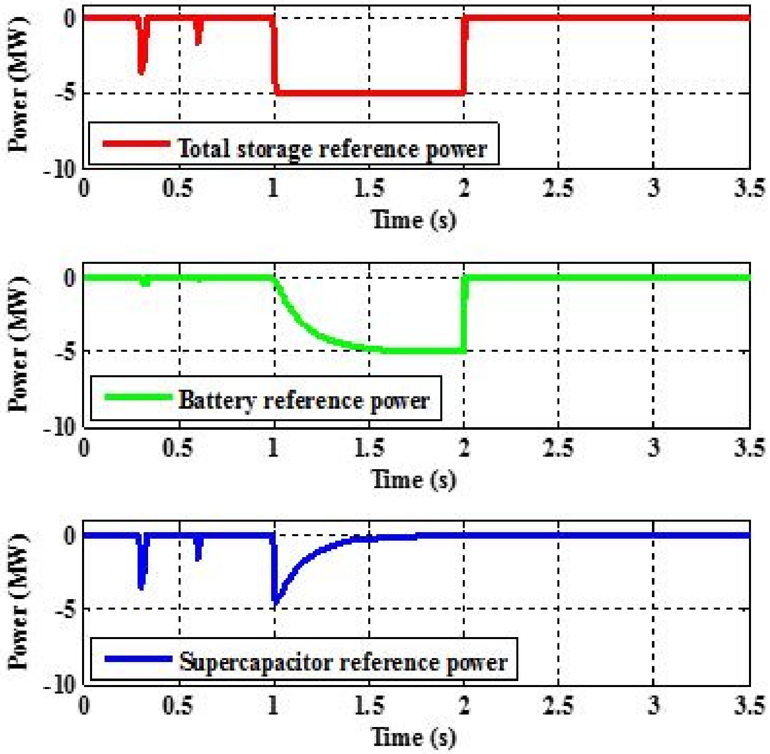

(a) Off-line simulation results.

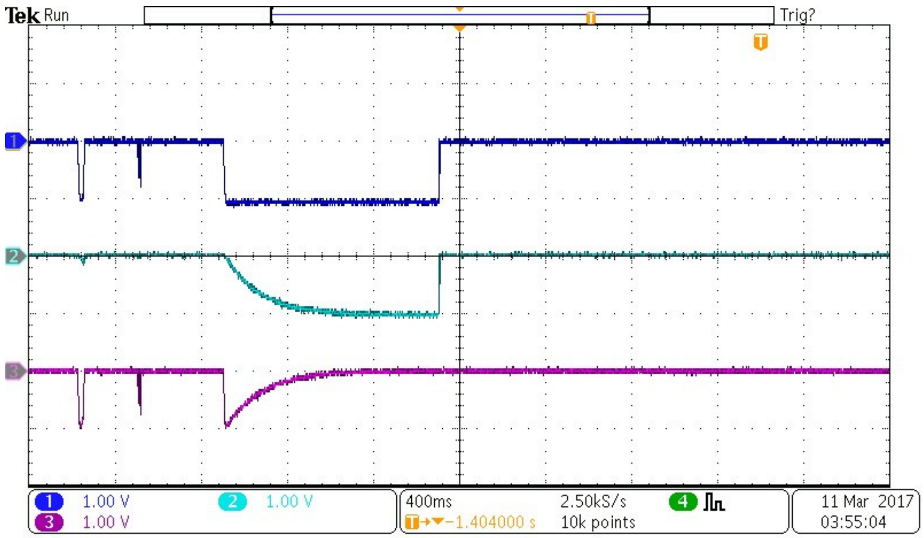

(b) CHIL results-oscilloscope plots: Ch1: total storage reference power, Ch2: battery reference power, Ch3: supercapacitor reference power (Ch1, Ch2, Ch3 = 5MW/div).

Figure 5.54: Reference power produced by FL controller and LPF based ESM system (case 3).

CHAPTER 6

CONCLUSION AND FUTURE WORK

6.1 Conclusion

The research work focused on the energy storage management system of the MVDC power system of the electric ship. With the incorporation of high power pulsed load (EMALS, and EMRG), the energy storages have become indispensable part of the shipboard power system. The main challenges of this research work is to find out the proper type of energy storages for the shipboard power system considering the size, weight, energy density, power density, and efficiency of the energy storages. As the space is limited in the shipboard, it is required to find out the appropriate energy storages to provide best service without consuming much space in the shipboard. Considering those issues, battery and supercapacitor are selected as the suitable energy storages for the shipboard power system. To show the real scenario of steady state and transient operations of the shipboard power system, it is challenging to model the shipboard power system with the all the components (generators, propulsion motors, MMC converters, DAB converters, battery model, supercapacitor mode, pulsed load, ship service load). It is required to model generators with excitation system, governor system and synchronous machine to show the real transient effects of the generator on the shipboard power system. If a three-phase infinite source is used instead of generator model, it can deliver any amount of power at any time without any change in output voltage. But a generator has limited capacity and it needs time to responds with the change of the load. If more power is drawn than its capacity, its voltage degrade. Considering those issues, it is impossible to show the operations of the energy storages of a MVDC power system without generators. For power transfer among the MVDC system and generators, MMC converters are used. MMC converter shows better controllability of DC output voltage than the three-phase rectifier. MMC converter also helps to limit fault current. The modeling of MMC converter is a difficult task with different operation principle than the three-phase rectifier. Here, ship propulsion system is also modeled with drive inverter, propeller and hydrodynamics to show the load variation of the shipboard power system with the variation of the ship's speed in knots. As the main load of the shipboard power system is the propulsion load and it changes with the variation of the ship's speed, it is required to model the shipboard propulsion system accurately to show the performances of the energy storages with the variation of the ship's speed. In this research work, pulsed power load is represented as constant power load instead of using resistive load to show the real effect of the pulsed load on the ship power system. For power transfer among the MVDC system and energy storages (battery and supercapacitor), DAB converters with galvanic isolation are used instead of conventional Buck-Boost DC-DC converters. The final goal is to design an ESM system for the shipboard power system to control the power transfer among the MVDC system and energy storages (battery and supercapacitor). To control the charging and discharging of the battery and supercapacitor with the changes of load demand, it is required to design an intelligent ESM system which is capable to provide reference power signal for charging and discharging of the energy storages. Here, at the beginning, two level FL based ESM system is designed. Simulation results showed that the two level FL based ESM system is capable to control the charging and discharging of the energy storages. But it creates some problem with the battery charging and discharging. Later, a LPF is designed to replace FL2 controller for power allocation of the battery and supercapacitor. A PI controller based ESM system is also designed to compare the performances with the FL based EMS system. Finally, the comparisons of the FL controller based ESM system and PI controller based ESM system are shown. Simulation results verify that the FL based ESM system shows superior performances than the PI controller based ESM system. Key contributions of the research work are summarized here,

- A MVDC system with IPS structure is designed to show transient and steady state behavior of the shipboard power system.
- The MVDC system is modeled with all the components (gas turbine based generators, propulsion hydrodynamics, MMC converter, battery model, supercapacitor model, DAB converter, pulsed load, ship service load, radar load).
- Two ESM systems (FL controller based and PI controller based) are designed to control power transfer among the energy storages and the MVDC system.
- Both the ESM systems are capable to control power transfer of the battery and supercapacitor to meet the transient and steady power demand of the MVDC system.
- Eventually, the comparisons of the FL controller and PI controller based ESM system are shown.

- Finally CHIL based experimental results are added to demonstrate the effectiveness of the controller.

6.2 Future Work

- In this research work, two ESM systems are designed for supervisory control of the energy storages. Battery and supercapacitor are connected to the MVDC system directly via DAB converters. The energy storages are not incorporated for individual loads. They are connected directly to the MVDC bus. Another technique for ESM system could be zonal energy storage management. In this technology, individual ESM system would be responsible to control power transfer among the individual zonal load and specified energy storages for this zone.
- Here energy storage are connected to the MVDC system. Another future aspect of this research would be to connect energy storages only for the pulsed load. In this potential location, energy storages would be responsible for power supply only to the pulsed load not for any other load and they will take charging power from the MVDC system. By connecting energy storages in this potential location, need to observe the bus voltage load power demand, and power quality.
- In this research work, battery and supercapacitor are used as the potential energy storages. Another prospective future work would be using other energy storages (for example: SMES, and FES) and compare the results with the results of the battery and supercapacitor.
- As the size of the shipboard power system is very large (40MW), it is difficult to implement the system experimentally. But a good solution would be to test the short version of the MVDC system.

APPENDIX A

OFFLINE SIMULATION MODEL

Charge controller MATLAB code

```
function [P_Sig_ref, Discharge_Bat, Charge_Bat, Discharge_SC, Charge_SC] =
fcn(Pref, Pgen,P_Sig, SOC_Bat, SOC_SC, Dis_Bat, Char_Bat, Dis_SC, Char_SC)

if (40<=SOC_Bat)&& (SOC_Bat<=90)
  if Pref>(Pgen)
      Dis_Bat=1;
  else
      Dis_Bat=0;
  end
   if Pgen>(Pref)
       Char_Bat=0;
   else
       Char_Bat=0;
   end

 end
 if (SOC_Bat<=40)% for overdischarging protection and charge if total generation
     %is higher than total load.
     if Pgen>(Pref0)
       Char_Bat=1;
       Dis_Bat=0;
   else
       Char_Bat=0;
       Dis_Bat=0;
     end
 end
 if (SOC_Bat>=90) %for overcharging protection and discharge if total generation
     %is higher than total load.
     if Pref>(Pgen)
       Char_Bat=0;
       Dis_Bat=1;
   else
       Char_Bat=0;
       Dis_Bat=0;
     end
 end

 % for supercapacitor
 if (40<=SOC_SC)&& (SOC_SC<=90)
   if Pref>(Pgen)
       Dis_SC=1;
   else
       Dis_SC=0;
```

```
  end
  if Pgen>(Pref)
      Char_SC=1;
  else
      Char_SC=0;
  end

end
if (SOC_SC<=40)% for overdischarging protection and charge if total generation
    %is higher than total load.
    if Pgen>(Pref)
      Char_SC=1;
      Dis_SC=0;
  else
      Char_SC=0;
      Dis_SC=0;
    end
end
if (SOC_SC>=90) %for overcharging protection and discharge if total generation
    %is higher than total load.
    if Pref>(Pgen)
      Char_SC=0;
      Dis_SC=1;
  else
      Char_SC=0;
      Dis_SC=0;
    end
end


if (1<=Dis_Bat)&& (1<=Dis_SC)
    P_Sig2=P_Sig;
else P_Sig2=0;
end
if (1<=Char_Bat)&& (1<=Char_SC)
    P_Sig3=P_Sig;
else P_Sig3=0;
end
if (P_Sig<=0)
    P_Sig4=P_Sig2;
else P_Sig4=P_Sig3;
end
Discharge_Bat=Dis_Bat;
Charge_Bat=Char_Bat;
Discharge_SC=Dis_SC;
Charge_SC=Char_SC;

P_Sig_ref=P_Sig4;
end
```

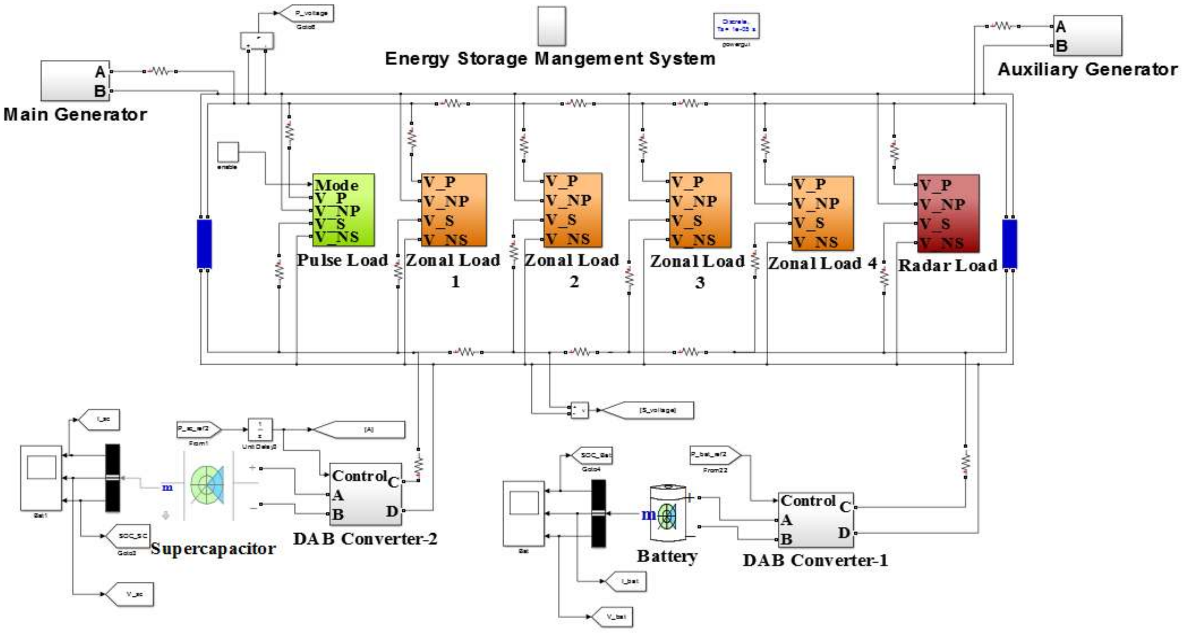

Figure A.1: MATLAB-Simulink diagram of 40MW MVDC power system with ESM system.

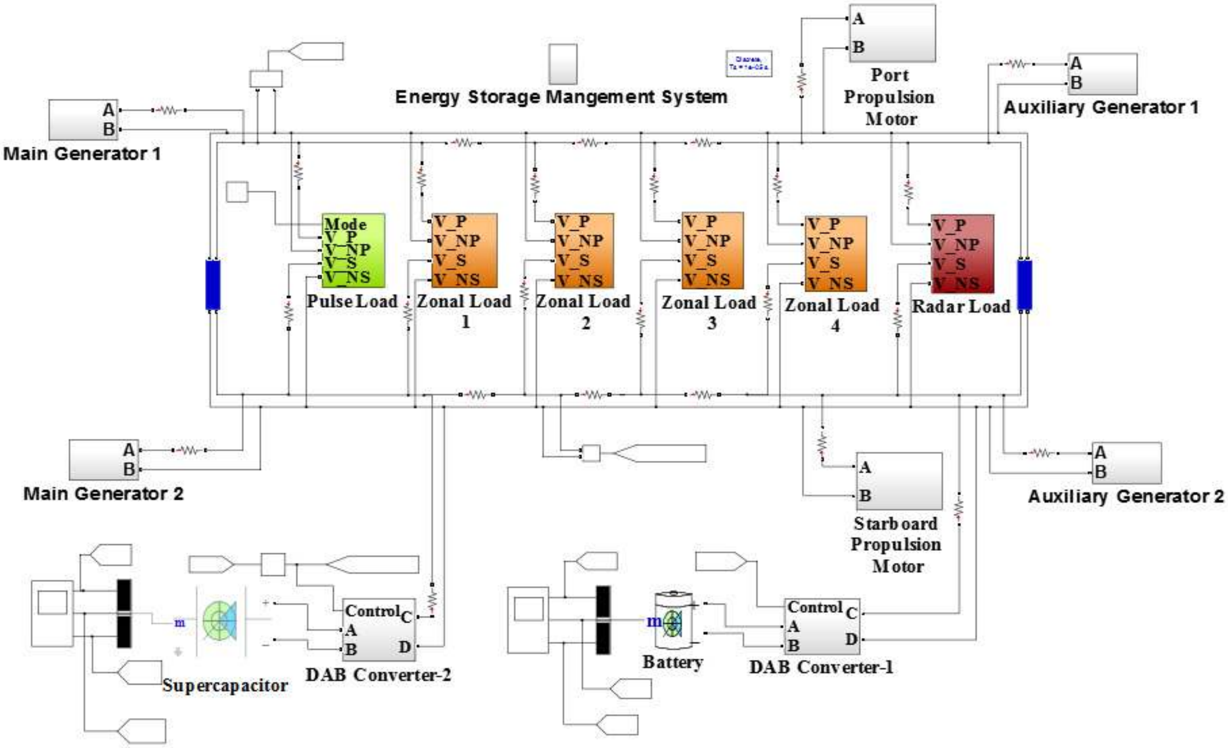

Figure A.2: MATLAB-Simulink diagram of 80MW MVDC power system with ESM system.

APPENDIX B

REAL-TIME MODEL

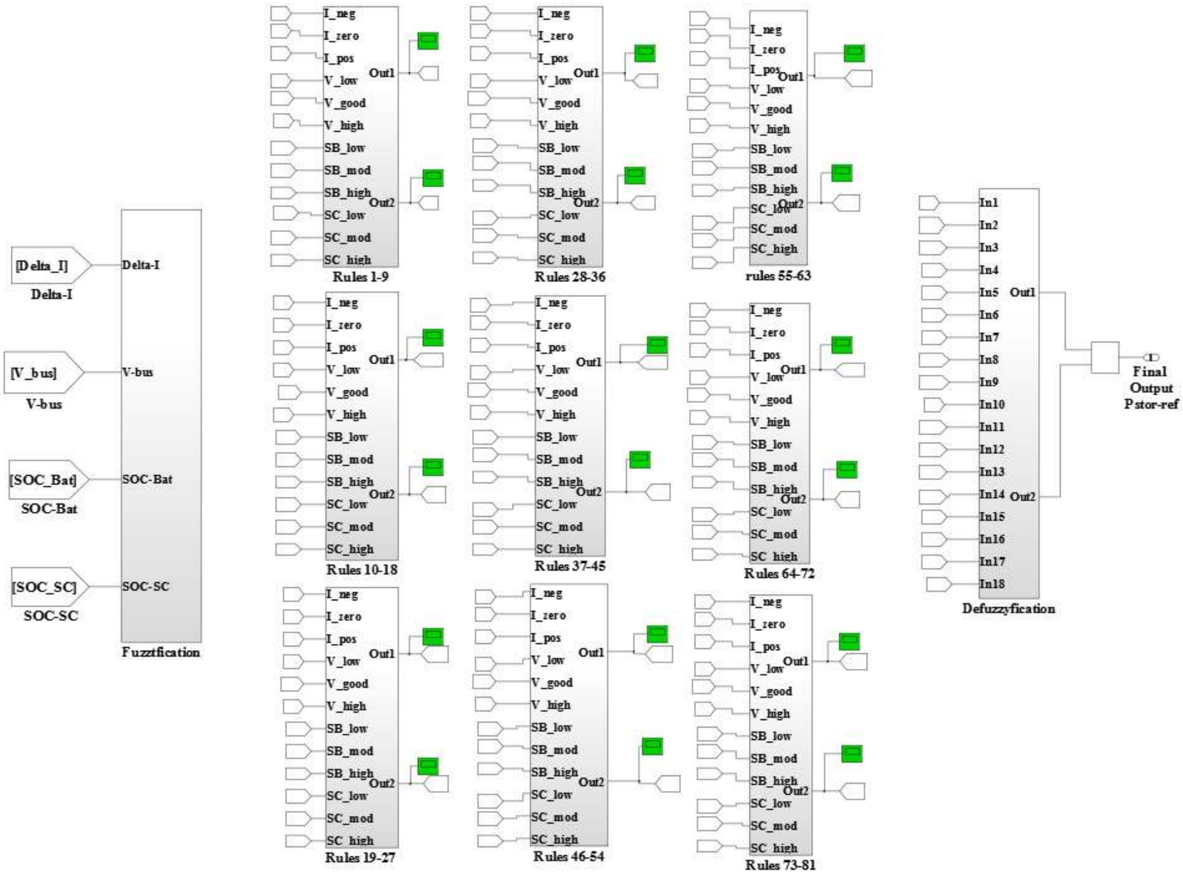

Figure B.1: Mathematical implementation of FL based ESM system.

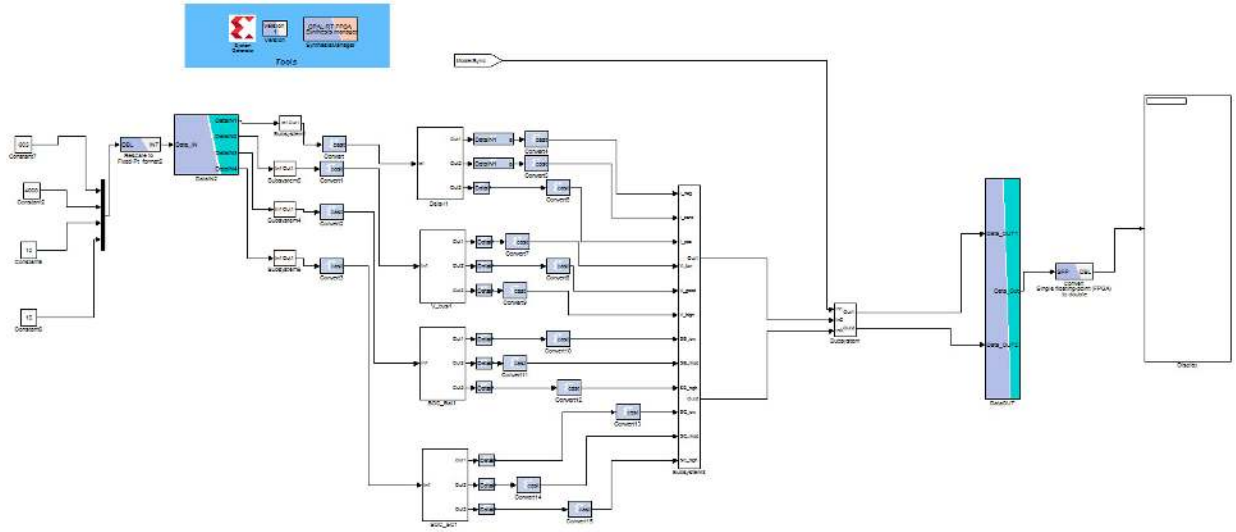

Figure B.2: RT-XSG model of FL based ESM system for FPGA implementation.

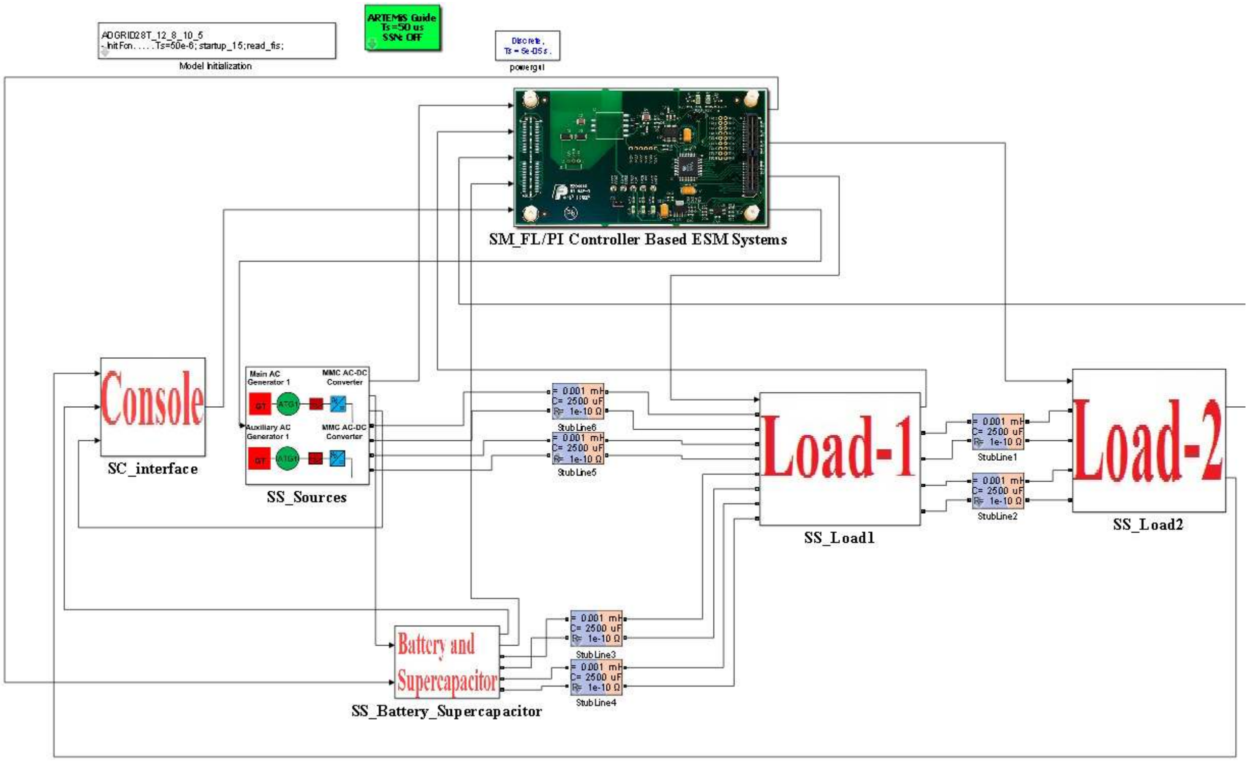

Figure B.3: Real-time simulation model of 40MW MVDC power system with ESM system in FPGA.

REFERENCES

[1] J. Amy, "Considerations in the design of naval electric power systems," in *Power Engineering Society Summer Meeting, 2002 IEEE*, vol. 1. IEEE, 2002, pp. 331–335.

[2] Q. Shen, *A distributed control approach for power and energy management in a notional shipboard power system*, 2012.

[3] N. Doerry, "Next generation integrated power systems (ngips) for the future fleet," in *IEEE Electric Ship Technologies Symposium*, 2009.

[4] R. J. Pifer, "Modeling of the electric ship," Ph.D. dissertation, Citeseer, 2010.

[5] A. Monti, S. D'Arco, L. Gao, and R. Dougal, "Energy storage management as key issue in control of power systems in future all electric ships," in *2008 International Symposium on Power Electronics, Electrical Drives, Automation and Motion*, 2008.

[6] C. Holsonback, T. Webb, T. Kiehne, and C. Seepersad, "System-level modeling and optimal design of an all-electric ship energy storage module," in *Electric Machines Technology Symposium*, 2006.

[7] J. Hou, J. Sun, and H. Hofmann, "Integrated control of power generation, electric motor and hybrid energy storage for all-electric ships," in *American Control Conference (ACC), 2016.* IEEE, 2016, pp. 6797–6802.

[8] ——, "Interaction analysis and integrated control of hybrid energy storage and generator control system for electric ship propulsion," in *American Control Conference (ACC), 2015.* IEEE, 2015, pp. 4988–4993.

[9] M. R. Miyazaki, A. J. Sørensen, and B. J. Vartdal, "Reduction of fuel consumption on hybrid marine power plants by strategic loading with energy storage devices," *IEEE Power and Energy Technology Systems Journal*, vol. 3, no. 4, pp. 207–217, 2016.

[10] A. Haseltalab, R. R. Negenborn, and G. Lodewijks, "Multi-level predictive control for energy management of hybrid ships in the presence of uncertainty and environmental disturbances," *IFAC-PapersOnLine*, vol. 49, no. 3, pp. 90–95, 2016.

[11] T. I. Bø and T. A. Johansen, "Battery power smoothing control in a marine electric power plant using nonlinear model predictive control," *IEEE Transactions on Control Systems Technology*, 2016.

[12] M. Steurer, M. Andrus, J. Langston, L. Qi, S. Suryanarayanan, S. Woodruff, and P. Ribeiro, "Investigating the impact of pulsed power charging demands on shipboard power quality," in *Electric Ship Technologies Symposium, 2007. ESTS'07. IEEE.* IEEE, 2007, pp. 315–321.

[13] H. A. Toliyat, S. Talebi, P. McMullen, C. Huynh, and A. Filatov, "Advanced high-speed flywheel energy storage systems for pulsed power applications," in *Electric Ship Technologies Symposium, 2005 IEEE.* IEEE, 2005, pp. 379–386.

[14] S. Kulkarni and S. Santoso, "Impact of pulse loads on electric ship power system: With and without flywheel energy storage systems," in *Electric Ship Technologies Symposium, 2009. ESTS 2009. IEEE.* IEEE, 2009, pp. 568–573.

[15] F. Scuiller, "Simulation of an energy storage system to compensate pulsed loads on shipboard electric power system," in *Electric Ship Technologies Symposium (ESTS), 2011 IEEE.* IEEE, 2011, pp. 396–401.

[16] B. Vural and C. Edrington, "Ultra-capacitor based pulse power management in electrical ships," in *Transportation Electrification Conference and Expo (ITEC), 2012 IEEE.* IEEE, 2012, pp. 1–5.

[17] R. E. Hebner, K. Davey, J. Herbst, D. Hall, J. Hahne, D. D. Surls, and A. Ouroua, "Dynamic load and storage integration," *Proceedings of the IEEE*, vol. 103, no. 12, pp. 2344–2354, 2015.

[18] D. Li, "Real-time simulation of shipboard power system and energy storage device management," Ph.D. dissertation, Kansas State University, 2014.

[19] I. J. Cohen, D. A. Wetz, S. Veiga, Q. Dong, and J. Heinzel, "Fuzzy logic control of a hybrid energy storage module for naval pulsed power applications," *arXiv preprint arXiv:1602.02045*, 2016.

[20] C. Yan, G. K. Venayagamoorthy, and K. A. Corzine, "Optimal location and sizing of energy storage modules for a smart electric ship power system," in *Computational Intelligence Applications In Smart Grid (CIASG), 2011 IEEE Symposium on.* IEEE, 2011, pp. 1–8.

[21] H. Zhang, F. Mollet, C. Saudemont, and B. Robyns, "Experimental validation of energy storage system management strategies for a local dc distribution system of more electric aircraft," *IEEE Transactions on Industrial Electronics*, vol. 57, no. 12, pp. 3905–3916, 2010.

[22] H. Zhou, T. Bhattacharya, D. Tran, T. S. T. Siew, and A. M. Khambadkone, "Composite energy storage system involving battery and ultracapacitor with dynamic energy management in microgrid applications," *IEEE transactions on power electronics*, vol. 26, no. 3, pp. 923–930, 2011.

[23] S. Castellan, R. Menis, A. Tessarolo, and G. Sulligoi, "Power electronics for all-electric ships with mvdc power distribution system: An overview," in *Ecological Vehicles and Renewable Energies (EVER), 2014 Ninth International Conference on.* IEEE, 2014, pp. 1–7.

[24] Y. Guo, M. Khan, M. Faruque, and K. Sun, "Fuzzy logic based energy storage supervision and control strategy for mvdc power system of all electric ship," in *Power and Energy Society General Meeting (PESGM), 2016.* IEEE, 2016, pp. 1–5.

[25] M. M. S. Khan and M. Faruque, "Management of hybrid energy storage systems for mvdc power system of all electric ship," in *North American Power Symposium (NAPS), 2016.* IEEE, 2016, pp. 1–6.

[26] M. M. S. Khan, M. O. Faruque, and A. Newaz, "Fuzzy logic based energy storage management system for mvdc power system of all electric ship," *IEEE Transactions on Energy Conversion*, 2017.

[27] "Ieee recommended practice for 1 kv to 35 kv medium-voltage dc power systems on ships," *IEEE Std 1709*, pp. 1–54, 2010.

[28] A. A. Ferreira, J. A. Pomilio, G. Spiazzi, and L. de Araujo Silva, "Energy management fuzzy logic supervisory for electric vehicle power supplies system," *IEEE Transactions on Power Electronics*, vol. 23, no. 1, pp. 107–115, 2008.

[29] J. Moreno, M. E. Ortúzar, and J. W. Dixon, "Energy-management system for a hybrid electric vehicle, using ultracapacitors and neural networks," *IEEE transactions on Industrial Electronics*, vol. 53, no. 2, pp. 614–623, 2006.

[30] M. Zandi, A. Payman, J.-P. Martin, S. Pierfederici, B. Davat, and F. Meibody-Tabar, "Energy management of a fuel cell/supercapacitor/battery power source for electric vehicular applications," *IEEE transactions on vehicular technology*, vol. 60, no. 2, pp. 433–443, 2011.

[31] R. Zamora and A. K. Srivastava, "Energy management and control algorithms for integration of energy storage within microgrid," in *2014 IEEE 23rd International Symposium on Industrial Electronics (ISIE).* IEEE, 2014, pp. 1805–1810.

[32] X. Li, D. Hui, and X. Lai, "Battery energy storage station (bess)-based smoothing control of photovoltaic (pv) and wind power generation fluctuations," *IEEE Transactions on Sustainable Energy*, vol. 4, no. 2, pp. 464–473, 2013.

[33] L. Zhu, J. Han, D. Peng, T. Wang, T. Tang, and J.-F. Charpentier, "Fuzzy logic based energy management strategy for a fuel cell/battery/ultra-capacitor hybrid ship," in *2014 First International Conference on Green Energy ICGE 2014.* IEEE, 2014, pp. 107–112.

[34] F. Jin, M. Wang, and C. Hu, "A fuzzy logic based power management strategy for hybrid energy storage system in hybrid electric vehicles considering battery degradation," in *Transportation Electrification Conference and Expo (ITEC), 2016 IEEE.* IEEE, 2016, pp. 1–7.

[35] M. Michalczuk, B. Ufnalski, and L. Grzesiak, "Fuzzy logic control of a hybrid battery-ultracapacitor energy storage for an urban electric vehicle," in *Ecological Vehicles and Renewable Energies (EVER), 2013 8th International Conference and Exhibition on.* IEEE, 2013, pp. 1–7.

[36] W. Yanzi, W. Wang *et al.*, "Energy management strategy based on fuzzy logic for a new hybrid battery-ultracapacitor energy storage system," in *Transportation Electrification Asia-Pacific (ITEC Asia-Pacific), 2014 IEEE Conference and Expo.* IEEE, 2014, pp. 1–5.

[37] C.-T. Pham, M. Daniel *et al.*, "Suitability analysis of fuzzy logic as an evaluation method for the selection of energy storage technologies in smart grid applications," in *Smart Electric Distribution Systems and Technologies (EDST), 2015 International Symposium on.* IEEE, 2015, pp. 452–457.

[38] A. Nourai, "Large-scale electricity storage technologies for energy management," in *Power Engineering Society Summer Meeting, 2002 IEEE*, vol. 1. IEEE, 2002, pp. 310–315.

[39] A. Donaldson and D. Williamson, "Advanced batteries: New capability for an electric ship," in *All Electric Ship: Developing Benefits for Maritime Applications*, 2005.

[40] S. Young, J. Newell, and G. Little, "Beyond electric ship," *Naval engineers journal*, vol. 113, no. 4, pp. 79–92, 2001.

[41] I. Hadjipaschalis, A. Poullikkas, and V. Efthimiou, "Overview of current and future energy storage technologies for electric power applications," *Renewable and sustainable energy reviews*, vol. 13, no. 6, pp. 1513–1522, 2009.

[42] H. Chen, T. N. Cong, W. Yang, C. Tan, Y. Li, and Y. Ding, "Progress in electrical energy storage system: A critical review," *Progress in Natural Science*, vol. 19, no. 3, pp. 291–312, 2009.

[43] S. Vazquez, S. M. Lukic, E. Galvan, L. G. Franquelo, and J. M. Carrasco, "Energy storage systems for transport and grid applications," *IEEE Transactions on Industrial Electronics*, vol. 57, no. 12, pp. 3881–3895, 2010.

[44] ——, "Lithium ion technical handbook," *Gold Peak Industries Ltd*, 2003.

[45] B. Dunn, H. Kamath, and J.-M. Tarascon, "Electrical energy storage for the grid: a battery of choices," *Science*, vol. 334, no. 6058, pp. 928–935, 2011.

[46] "Li-ion vs. lead acid," https://www.ultralifecorporation.com/, accessed: 2016-09-29.

[47] G. Albright, J. Edie, and S. Al-Hallaj, “A comparison of lead acid to lithium-ion in stationary storage applications,” *Alternative Energy eMagazine Industry [online serial](April 12)*, 2012.

[48] M. S. Whittingham, “History, evolution, and future status of energy storage,” *Proceedings of the IEEE*, vol. 100, no. Special Centennial Issue, pp. 1518–1534, 2012.

[49] P. Denholm, E. Ela, B. Kirby, and M. Milligan, “The role of energy storage with renewable electricity generation,” 2010.

[50] S. Teleke, “Energy storage overview: applications, technologies and economical evaluation,” *Quanta Technology Technical Papers, http://www. sandia. gov/ess/publications/SAND2010-0815. pdf*, 2011.

[51] M. S. Whittingham, “History, evolution, and future status of energy storage,” *Proceedings of the IEEE*, vol. 100, no. Special Centennial Issue, pp. 1518–1534, 2012.

[52] W. Yuan, *Second-generation high-temperature superconducting coils and their applications for energy storage.* Springer Science & Business Media, 2011.

[53] L. Chen, Y. Liu, A. Arsoy, P. Ribeiro, M. Steurer, and M. Iravani, “Detailed modeling of superconducting magnetic energy storage (smes) system,” *IEEE Transactions on Power Delivery*, vol. 21, no. 2, pp. 699–710, 2006.

[54] G. Fuchs, B. Lunz, M. Leuthold, and D. Sauer, “Technology overview on electricity storage,” *ISEA, Aachen, Juni*, 2012.

[55] Z. Long and Q. Zhiping, “Review of flywheel energy storage system,” in *Proceedings of ISES World Congress 2007 (Vol. I–Vol. V).* Springer, 2008, pp. 2815–2819.

[56] N. Doerry and J. V. Amy Jr, “The road to mvdc,” in *ASNE Intelligent Ships Symposium*, 2015.

[57] P. C. L. Petersen, “Naval sea systems command washington dc,” 2010.

[58] Q. Shen, B. Ramachandran, S. K. Srivastava, M. Andrus, and D. A. Cartes, “Power and energy management in integrated power system,” in *2011 IEEE Electric Ship Technologies Symposium.* IEEE, 2011, pp. 414–419.

[59] R. W. D. D. F. Mura, “Preparation of a medium-voltage dc grid demonstration project,” in *E.ON Energy Research Center Seriesn*, vol. 4, 2008.

[60] M. Andrus, M. Bosworth, J. Crider, H. Ouroua, E. Santi, and S. Sudhoff, “Notional system models,” 2015, Electric Ship Research and Development Consortium.

[61] E. N. Abildgaard and M. Molinas, “Modelling and control of the modular multilevel converter (mmc),” *Energy Procedia*, vol. 20, pp. 227–236, 2012.

[62] S. Debnath, J. Qin, B. Bahrani, M. Saeedifard, and P. Barbosa, “Operation, control, and applications of the modular multilevel converter: A review,” *IEEE transactions on power electronics*, vol. 30, no. 1, pp. 37–53, 2015.

[63] M. Andrus, M. Bosworth, J. Crider, H. Ouroua, E. Santi, and S. Sudhoff, “Notional system report,” 2014.

[64] K. Sun, D. Soto, M. Steurer, and M. Faruque, “Experimental verification of limiting fault currents in mvdc systems by using modular multilevel converters,” in *Electric Ship Technologies Symposium (ESTS), 2015 IEEE*. IEEE, 2015, pp. 27–33.

[65] E. Lecourt, “Using simulation to determine the maneuvering performance of the wagb-20,” *Naval engineers journal*, vol. 110, no. 1, pp. 171–188, 1998.

[66] “Dd(x) notional baseline modeling and simulation development report,” Syntek, Tech. Rep., August 2003.

[67] R. F. Roddy, D. E. Hess, and W. Faller, “Neural network predictions of the 4-quadrant wageningen propeller series,” DTIC Document, Tech. Rep., 2006.

[68] “shipdata2.xls,” Syntek, Tech. Rep., August 2003.

[69] M. Collins, “Dd (x) transformational technologies for the navys surface combatant,” *Proc. of FIATECH*, pp. 6–7, 2004.

[70] H. R. Karshenas, A. Bakhshai, A. Safaee, H. Daneshpajooh, and P. Jain, *Bidirectional dc-dc converters for energy storage systems*. INTECH Open Access Publisher, 2011.

[71] I.-Y. Chung, W. Liu, M. Andrus, K. Schoder, S. Leng, D. A. Cartes, and M. Steurer, “Integration of a bi-directional dc-dc converter model into a large-scale system simulation of a shipboard mvdc power system,” in *2009 IEEE Electric Ship Technologies Symposium*. IEEE, 2009, pp. 318–325.

[72] H. Zhou, T. Bhattacharya, and A. M. Khambadkone, “Composite energy storage system using dynamic energy management in microgrid applications,” in *Power Electronics Conference (IPEC), 2010 International*. IEEE, 2010, pp. 1163–1168.

[73] Q. Bajracharya, “Dynamic modeling, monitoring and control of energy storage system,” *Karlstad University-2013*, 2013.

[74] M. Ceraolo, “New dynamical models of lead-acid batteries,” *IEEE transactions on Power Systems*, vol. 15, no. 4, pp. 1184–1190, 2000.

[75] J. P. Cun, J. N. Fiorina, M. Fraisse, and H. Mabboux, “The experience of a ups company in advanced battery monitoring,” in *Telecommunications Energy Conference, 1996. INTELEC’96., 18th International*. IEEE, 1996, pp. 646–653.

[76] M. Valvo, F. E. Wicks, D. Robertson, and S. Rudin, “Development and application of an improved equivalent circuit model of a lead acid battery,” in *Energy Conversion Engineering Conference, 1996. IECEC 96., Proceedings of the 31st Intersociety*, vol. 2. IEEE, 1996, pp. 1159–1163.

[77] F. M. González-Longatt, “Circuit based battery models: a review,” in *Proceedings of 2nd Congreso IberoAmericano De Estudiantes de Ingenieria Electrica, Puerto la Cruz, Venezuela*, 2006.

[78] “Mathworks battery,” http://www.mathworks.com/help/physmod/sps/powersys/ref/battery.html?requestedDomain=www.mathworks.com, accessed: 2016-09-30.

[79] C. M. Shepherd, “Design of primary and secondary cells ii. an equation describing battery discharge,” *Journal of the Electrochemical Society*, vol. 112, no. 7, pp. 657–664, 1965.

[80] O. Tremblay and L.-A. Dessaint, “Experimental validation of a battery dynamic model for ev applications,” *World Electric Vehicle Journal*, vol. 3, no. 1, pp. 1–10, 2009.

[81] “Wikipediasupercapacitor,” https://en.wikipedia.org/wiki/Supercapacitor, accessed: 2016-09-30.

[82] Z.-l. Cheng, W.-r. Chen, Q. Li, Z.-l. Jiang, and Z.-h. Yang, “Modeling and dynamic simulation of an efficient energy storage component-supercapacitor,” in *2010 Asia-Pacific Power and Energy Engineering Conference*. IEEE, 2010, pp. 1–4.

[83] S. Kim and S. S. Williamson, “Modeling, design, and control of a fuel cell/battery/ultra-capacitor electric vehicle energy storage system,” in *2010 IEEE Vehicle Power and Propulsion Conference*. IEEE, 2010, pp. 1–5.

[84] “Mathworks supercapacitor,” http://www.mathworks.com/help/physmod/sps/powersys/ref/supercapacitor.html, accessed: 2016-09-30.

[85] H. Zhang, H. Fakham, C. Saudemont, and B. Robyns, “Power management strategies in a local dc power distribution system of more electric aircraft with the help of hybrid storage and dissipation systems,” in *Advanced Electromechanical Motion Systems & Electric Drives Joint Symposium, 2009. ELECTROMOTION 2009. 8th International Symposium on*. IEEE, 2009, pp. 1–7.

[86] D. Tran, H. Zhou, and A. M. Khambadkone, “Energy management and dynamic control in composite energy storage system for micro-grid applications,” in *IECON 2010-36th Annual Conference on IEEE Industrial Electronics Society*. IEEE, 2010, pp. 1818–1824.

[87] R. Teodorescu, M. Liserre *et al.*, *Grid converters for photovoltaic and wind power systems.* John Wiley & Sons, 2011, vol. 29.

[88] W. Bin, L. Yongqiang, Z. Navid, and K. Samir, "Power conversion and control of wind energy systems," 2011.

[89] S. Mikkili, A. K. Panda, and J. Prattipati, "Review of real-time simulator and the steps involved for implementation of a model from matlab/simulink to real-time," *Journal of The Institution of Engineers (India): Series B*, vol. 96, no. 2, pp. 179–196, 2015.

[90] "OP7020 simulator," http://www.opal-rt.com/hardware-io-expansion-box/-op7020/, accessed: 2017-03-13.

[91] "OP6507 simulator," http://www.opal-rt.com/hardware-io-expansion-box-op5707/, accessed: 2017-03-13.

BIOGRAPHICAL SKETCH

Mohammed Masum Siraj Khan was born in Chittagong, Bangladesh. He received his B.Sc degree in Electrical and Electronic Engineering from Bangladesh University of Engineering and Technology (BUET) in 2013. Currently he is pursuing his M.S. degree in Electrical and Computer Engineering in Florida State University (FSU). From September, 2014 he has been working as a research assistant at Center for Advanced Power Systems (CAPS). His research interests are in controller-hardware-in-loop (CHIL) based simulations, real-time simulations, Power Electronics converter design and renewable energy systems.